The Dissertation Committee for Shaolie Samira Hossain Certifies that this is the approved version of the following dissertation:

MATHEMATICAL MODELING OF COUPLED DRUG AND DRUG-ENCAPSULATED NANOPARTICLE TRANSPORT IN PATIENT-SPECIFIC CORONARY ARTERY WALLS

Committee:

Thomas J. R. Hughes, Supervisor

Robert D. Moser, Co-Supervisor

Ronald E. Barr

Richard H. Crawford

Syed F. A. Hossainy

MATHEMATICAL MODELING OF COUPLED DRUG AND DRUG-ENCAPSULATED NANOPARTICLE TRANSPORT IN PATIENT-SPECIFIC CORONARY ARTERY WALLS

by

Shaolie Samira Hossain, B.S.; M.S.

Dissertation

Presented to the Faculty of the Graduate School of
The University of Texas at Austin
in Partial Fulfillment
of the Requirements
for the Degree of

Doctor of Philosophy

The University of Texas at Austin
December, 2009

Dedication

To my parents

Acknowledgements

I would like to express my sincere gratitude to my advisor, Professor Thomas J. R. Hughes for his inspiration, guidance and faith in me. I would also like to acknowledge Dr. Syed F. A. Hossainy for his vision and encouragement, and Abbott Vascular for its support. I am grateful to my distinguished committee members for their valuable input and suggestions.

A shout out to all my coworkers for their cooperation, especially Yuri Bazilevs for showing me the light at the end of the tunnel. Hook 'em Horns!

I am deeply indebted to my parents, Shahana Hossain and Dr. M. Anwar Hossain, for their unconditional love and unwavering support, and my sister (also my life coach), Natalie Hossain, for always being there for me.

Finally, I would like to take this opportunity to remember late Professor William C. Reynolds for believing in me and exposing me to the exciting world of computational sciences when I first came to Stanford.

MATHEMATICAL MODELING OF COUPLED DRUG AND DRUG-ENCAPSULATED NANOPARTICLE TRANSPORT IN PATIENT-SPECIFIC CORONARY ARTERY WALLS

Publication No._____________

Shaolie Samira Hossain, Ph.D.
The University of Texas at Austin, 2009

Supervisor: Thomas J. R. Hughes

A vast majority of heart attacks occur due to rapid progression of plaque buildup in the coronary arteries that supply blood to the heart muscles. The diseased arteries can be treated with drugs delivered locally to vulnerable plaques—ones that may rupture and release emboli, resulting in the formation of thrombus, or blood clot that can cause blockage of the arterial lumen.

In designing these local drug delivery devices, important issues regarding drug distribution and targeting need to be addressed to ensure device design optimization as physiological forces can cause the local concentration to be very different from mean drug tissue concentration estimated from *in vitro* experiments and animal studies. Therefore, the main objective of this work was to develop a computational tool-set to support the design of a catheter-based local drug delivery system that uses nanoparticles as drug carriers by simulating drug transport and quantifying local drug distribution in coronary artery walls. Toward this end, a three dimensional mathematical model of coupled transport of drug and drug-encapsulated nanoparticles was developed and solved numerically by applying finite element based isogeometric analysis that uses NURBS-based techniques to describe the artery wall geometry.

To gain insight into the parametric sensitivity of drug distribution, a study of the effect of Damkohler number and Peclet number was carried out. The tool was then applied to a three-dimensional idealized multilayered model of the coronary artery wall under healthy and diseased condition. Preliminary results indicated that use of realistic geometry is essential in creating physiological flow features and transport forces necessary for developing catheter-based drug delivery design procedures. Hence, simulations were run on a patient-specific coronary artery wall segment with a typical atherosclerotic plaque characterized by a lipid pool encased by a thin fibrous cap. Results show that plaque heterogeneity and artery wall inhomogeneity have a considerable effect on drug distribution.

The computational tool-set developed was able to successfully capture trends observed in local drug delivery by incorporating a multitude of relevant physiological phenomena, and thus demonstrated its potential utility in optimizing drug design parameters including delivery location, nanoparticle surface properties and drug release rate.

Table of Contents

CHAPTER 3 32

CHAPTER 4 41

CHAPTER 5 60

List of Tables

List of Figures

CHAPTER 1

Background and Significance

This section provides a brief background on the concept of vulnerable plaque, its role in causing acute cardiac events and current status of medical therapy. For this, the structure adopted by Lau et al. in [1] and Spratt et al. in [2] will be followed closely while relying heavily on a few relevant articles [3-5] (along with the two previously mentioned articles) for content. After building the case for local drug delivery systems as a viable option for treating vulnerable plaques, the motivation for the proposed work will be presented by outlining potential application and significance of the computational tool developed.

1.1 ACUTE CORONARY SYNDROME

Cardiovascular disease is the number one killer in the United States. Each year about 1.1 million Americans suffer a myocardial infarction (MI), i.e., heart attack, and almost half of them die from it, accounting for 1 in 5 deaths in the United States [6, 7]. The majority of these cardiac events occur suddenly in patients with no known history of coronary artery disease. But a large number take place in patients already diagnosed and treated for cardiovascular diseases. Even with today's best standard of care, one out of every six men diagnosed with a myocardial infarction will have another one within six years, while women are twice as likely to have a repeat MI [7]. Additionally, health care expenditure associated with cardiovascular diseases is increasing rapidly; in 2008 the projected cost was $448.5 billion [8]. There is, therefore, an overwhelming need to develop methods for early diagnosis and acute treatment of atherosclerosis—the root cause of cardiovascular diseases, and prevent its progression to heart attack.

Heart attacks are caused by blockages in the coronary arteries that supply oxygen-rich blood to the heart's muscular wall (the myocardium). The obstruction in the arterial lumen retards the blood flow; as a result, the heart muscles starve for oxygen causing acute coronary syndrome. This condition manifests as either unstable angina (chest pain), or acute myocardial infarction (tissue death) that leads to permanent loss of muscular contraction, causing heart attack (see Figure 1.1).

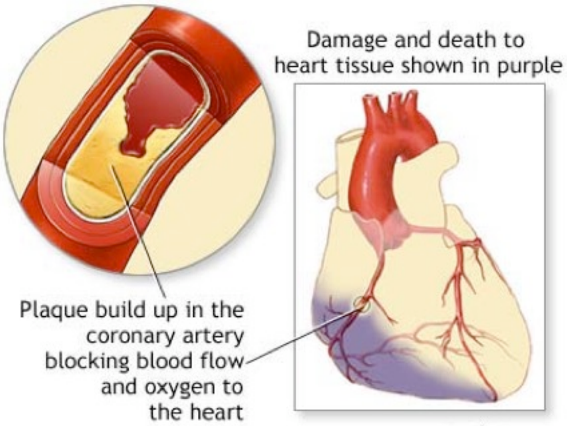

Figure 1.1: Coronary artery disease leading to acute coronary syndrome, causing heart attacks. [9]

These blockages occur due to atherosclerosis—the build up of plaque in the arterial wall that develops from low-density lipoprotein cholesterol (LDL). As

LDL enters the intima through the endothelium of the diseased artery wall, it reacts with oxygen producing oxidized-LDL. This triggers an immunoresponse where white blood cells, namely monocyte-derived macrophages are dispatched to consume the toxic oxidized-LDL forming foam cells—the main component of the atherosclerotic plaque. These lipid laden foam cells in turn capture monocytes that transform into macrophages, and the process repeats itself resulting in increased plaque size and gradual narrowing of the artery lumen (see Figure 1.2).

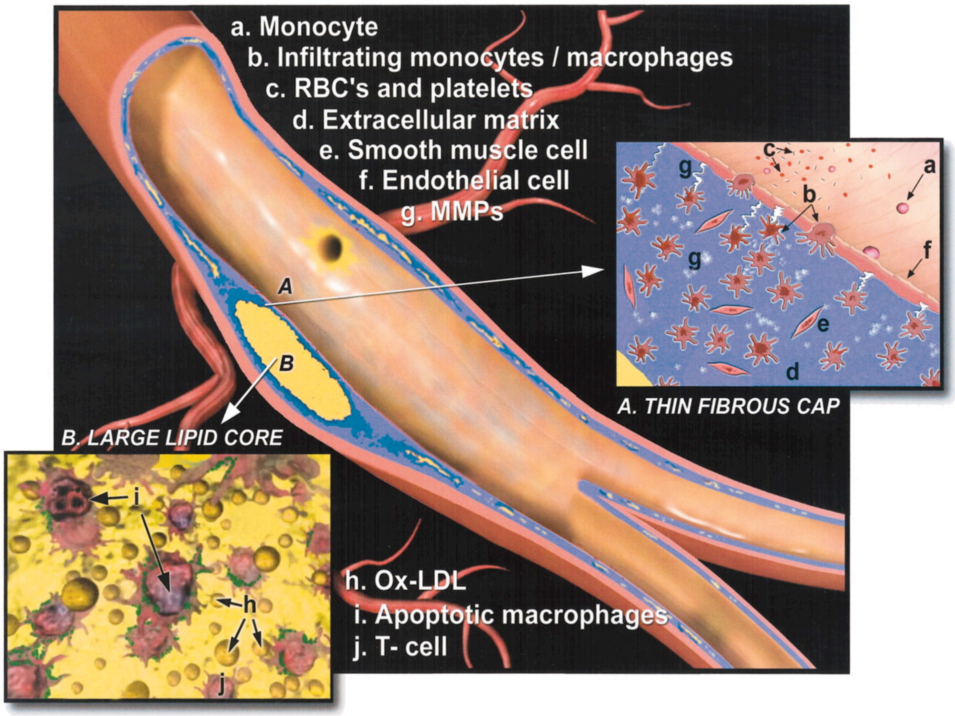

Figure 1.2: Schematic figure illustrating the most common type of vulnerable plaque characterized by thin fibrous cap, extensive macrophage infiltration, paucity of smooth muscle cells, and large lipid core, without significant luminal narrowing. [5]

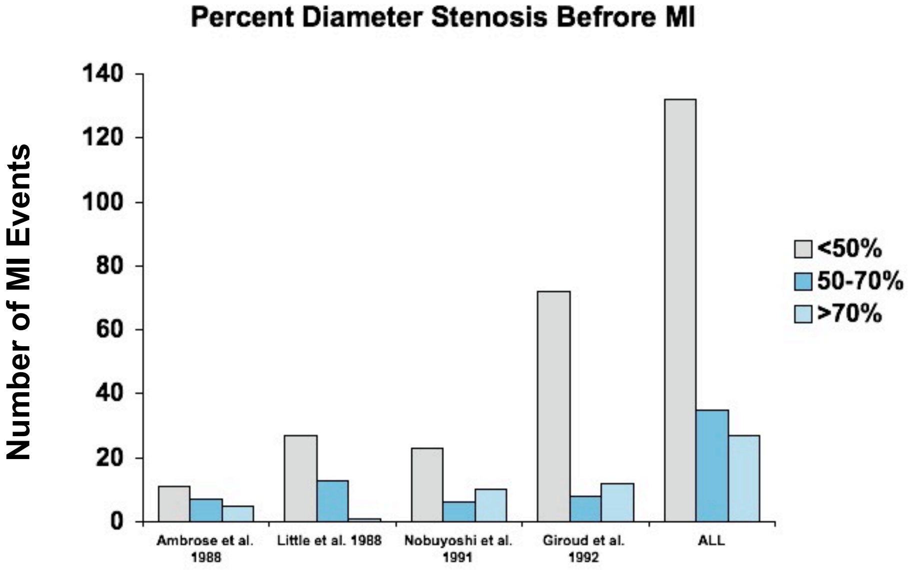

Figure 1.3: Angiography is a poor predictor of vulnerable plaque. Here findings of four different papers are presented that reported the number of MI events and corresponding percent diameter stenosis. Majority of the MI's occur in patients with less than 50% blockage. [10]

1.2 VULNERABLE PLAQUE AND ITS IDENTIFICATION

Patients with blockage of more than 60–70 percent are generally considered to be at a higher risk for acute myocardial infarctions (AMI). But recent studies using angiographic images show that a vast majority of these AMI's occur in patients with less than 50 percent blockage (see Figure 1.3), indicating that factors other than degree of stenosis are responsible for these sudden cardiac events. Most acute coronary syndromes can be attributed to coronary thrombosis resulting from plaque rupture. Plaque disruption exposes its lipid content to the lumen creating blood clots. This leads to thrombus formation and blockage of the arterial lumen causing acute coronary syndrome. These plaques that are at high risk for rupture or erosion, are referred to as vulnerable plaques.

Researchers have identified specific structural characteristics that distinguish vulnerable plaques from stable plaques, including, i) a large lipid-rich core (> 40% of plaque area), ii) a thin fibrous cap (< 165 μm), and iii) inflammation (see Figure 1.2). Figure 1.4 illustrates different types of vulnerable plaques based on their composition [5], providing a more comprehensive guideline for their identification.

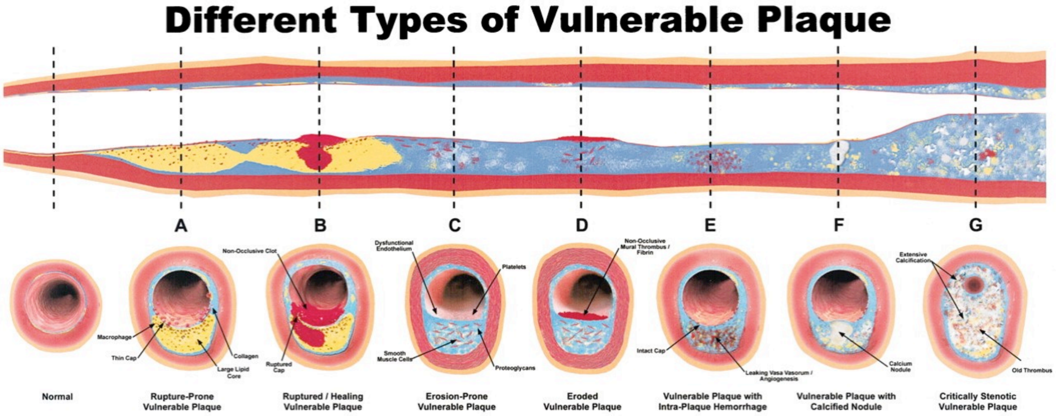

Figure 1.4: Different types of vulnerable plaque as underlying cause of acute coronary events and sudden cardiac death (SCD). A, Rupture-prone plaque with large lipid core and thin fibrous cap infiltrated by macrophages. B, Ruptured plaque with subocclusive thrombus and early organization. C, Erosion-prone plaque with proteoglycan matrix in a smooth muscle cell-rich plaque. D, Eroded plaque with subocclusive thrombus. E, Intraplaque hemorrhage secondary to leaking vasa vasorum. F, Calcific nodule protruding into the vessel lumen. G, Chronically stenotic plaque with severe calcification, old thrombus, and eccentric lumen. [5]

Additionally, systemic inflammation in vessel walls is known to be a reliable indicator of plaque instability. Therefore, detection of established biomarkers of plaque vulnerability, such as C-reactive protein (CRP) [11], may also lead to the diagnosis of patients with high-risk atherosclerotic lesions.

Despite the great progress made in diagnostic technology, timely identification of vulnerable plaques remains a challenge. Multiple imaging modalities, both invasive and non-invasive, have been proposed; among which intravascular ultrasound (IVUS) is the most promising. Clinical studies with IVUS have successfully identified characteristic features of vulnerable plaques, such as a lipid-laden necrotic core and a thin fibrous cap. Consequently, physicians have now started using IVUS routinely in cath-labs during intervention, making early diagnosis of vulnerable plaques a real possibility.

1.3 TREATMENT OF VULNERABLE PLAQUE

Proposed clinical strategies for diffusing vulnerable plaques mainly involve i) reducing the propensity to rupture by changing plaque composition or by improving endothelial function, and ii) reducing blood thrombogenicity. The former is referred to as plaque stabilization, and the latter as plaque passivation. Plaque stabilization can be achieved by decreasing LDL content, and reducing inflammation in atherosclerotic plaque through local or systemic administration of drugs, or by controlling diet. These conclusions, supported by animal studies [12-14], provide the rationale for treatment of vulnerable plaques.

1.3.1 Current practices and proposed treatment options

It is well recognized that vulnerable plaque is only the focal manifestation of a disease that is systemic at its root. Systemic drugs such as Statins (lipid-lowering agent) and Aspirins (antithrombotic agent) are preventing a substantial portion of events in patients. According to well-regarded clinical studies, patients treated with Statins have consistently lower rates of cardiac events than control subjects (see Figure 1.5). Aspirin, on the other hand, has been shown to be effective in reducing the risk of forming blood clots. Physicians have, therefore, widely adopted systemic drugs as a viable prospective way to prevent cardiac events. However, the majority of these events are still left to occur. Therefore the goal is to augment the benefits that Statins provide, to help treat patients acutely and thus more effectively, and achieve a 0% event rate through artery-specific therapies.

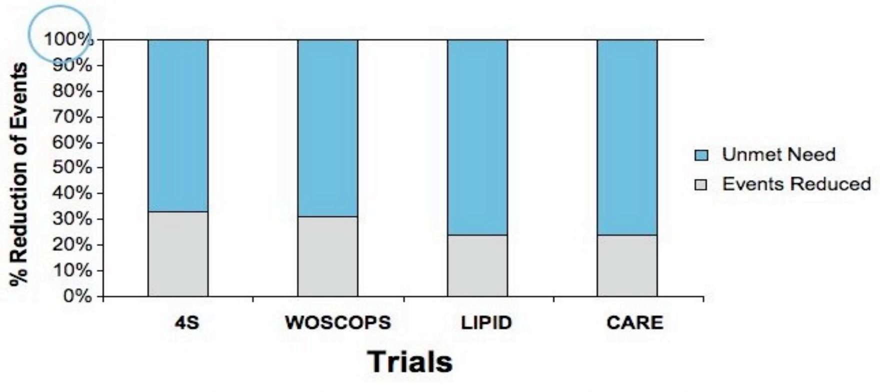

Lancet 1994;344:1383-1389
NEJM 1995;335:1001-1009
NEJM 1995;333:1301-1307
NEJM 1998;339:1349-1357

Figure 1.5: Sample of four key studies that appeared in top peer-reviewed publications that show significant reduction in number of events compared to control subjects. A huge unmet need still exists that can be targeted. [15-18]

There are important practical considerations that make the local drug delivery concept particularly attractive due to certain limitations of systemic therapy. Although many of the commonly used medications in cardiovascular medicine have positive effects on long-term plaque stabilization, the time course of these changes is unclear. In some cases, reduction in plaque lipid content or thrombogenicity can take as long as six months. Additionally, possible side effects like bleeding complications resulting from antithrombotic drugs pose a serious health concern. Local drug delivery takes care of these problems by providing concentrated targeted therapy acutely with a much smaller amount of drug. This ensures a high local drug tissue concentration and minimal systemic loss or side effect. Therefore, it is reasonable to conclude that a combined treatment approach incorporating both local and systemic administration of anti-thrombotic and lipid-lowering drugs may provide rapid treatment of vulnerable plaques as well as long-term prevention of acute coronary syndrome.

1.4 LOCAL DRUG DELIVERY SYSTEM

Recent advances in diagnostic technology and interventional cardiology have made targeted therapy, taking patient-specific artery wall geometry and plaque characteristic into account, a viable treatment option. In developing these local drug delivery systems, a multitude of clinical and design issues need to be considered. For example, a local drug delivery system should produce a high local drug concentration within the therapeutic window while reducing systemic leakage. Possible candidates for such drug delivery platforms include catheter-based delivery systems and drug eluting stents. These devices may deliver drug directly, or through local delivery vehicles, such as liposomes, shaped particles, polymeric nanoparticles, and so on (see Section 1.4.2). This work focuses on catheter-based delivery devices that use polymeric nanoparticles as drug carriers.

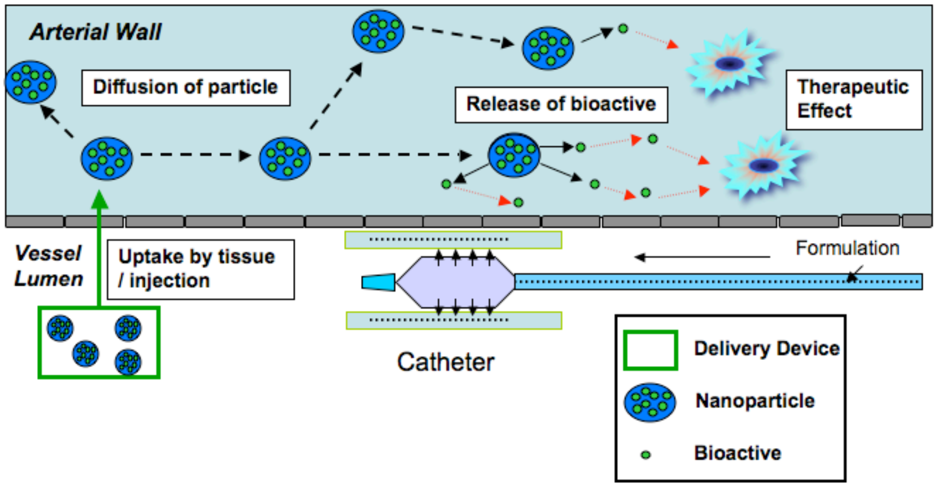

Figure 1.6: Schematic of the lumen-side drug delivery concept. [19]

1.4.1 Luminal drug delivery product concept

In a typical luminal drug delivery mechanism, a catheter is usually inserted in the groin. With the aid of live angiographic images, the physician guides the catheter through the artery into the heart until it reaches the target site of the diseased coronary artery. The catheter then releases a solution containing the drug-encapsulated delivery vehicle of choice (e.g., nanoparticles) radially into the arterial lumen. Following the tissue uptake of this solution, the delivery vehicles transport through the wall mainly via diffusion and advection while releasing the encapsulated drug. The released drug then travels through the wall and provides therapeutic effect to the targeted region (see Figure 1.6).

This concept provides regional treatment of the atherosclerotic plaque in a timely manner that results in sustained reduction in plaque progression. It is a relatively safe deliverable product concept that adds value over systemic therapy.

1.4.2 Nanoparticles as delivery vehicles

In recent years, polymeric nanoparticles (NPs) have generated a great deal of interest in the medical device community as effective drug delivery vehicles because they can provide controlled release of drug, achieve targeted delivery through surface modification, protect the drug from degradation, and reduce systemic toxic effect [20]. These are usually 20-500 nanometer (nm) polymeric spherical particles with the drug encapsulated within the polymer.

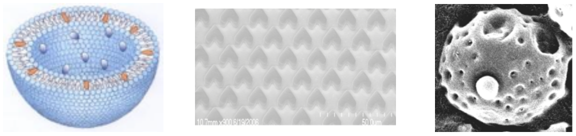
(a) (b) (c)

Figure 1.7: Examples of different drug delivery vehicles. (a) Liposome (b) shaped particles (c) polymeric nanoparticles [21]. Drug release rate is governed by drug diffusion and polymer degradation.

Since the nanoparticles can carry only a limited amount of drug, predictive models have been developed to describe mass transport of drug within a polymeric system to assist in the design of an optimized formulation. The tailored drug release rate profile obtained from these models serves as an essential ingredient in developing a coupled arterial mass transport model simulating the local drug delivery system (further discussed in Section 2.2.2).

1.5 MOTIVATION

The application of these medical devices in treating patients with high-risk lesions in a clinical setting can be challenging. This is mainly because of key design issues that need to be resolved on a case by case basis prior to treatment administration, including:

- delivery platform and location to use for maximum efficacy,
- type of vehicle to use to achieve targeted delivery,

which require performing specific tasks with some degree of reliability, for example,

- quantitative prediction of local drug distribution in the artery wall,
- evaluation of the effect of physiological forces on local drug distribution,
- tuning of the drug release rate profile to the temporal sequence of the target biological process in the affected region.

Experimental techniques are unable to address these critical design and targeting issues as they prove to be unsafe and often non-feasible to be performed *in vivo* on human patients. Numerical tools are particularly useful in this regard because they can provide crucial information that is otherwise unavailable.

Therefore, there is a pressing need for building technologies that will use mathematical models on patient-specific geometries to determine optimum drug design parameters, such as delivery location, delivery mechanism, drug release rate profile, vehicle size, vehicle surface properties, drug viscosity, etc., for a desired drug tissue concentration in the arterial wall. This work aims to address this need by developing a computational tool to support the design and analysis of a catheter-based local drug delivery system, and thus to make a useful contribution in the prevention of acute coronary syndrome.

The computational tool developed can help analysis by determining simple metrics like mean residence time (MRT) to measure the effectiveness of different drug delivery configurations. Additionally, dominant dimensionless numbers can be identified through a nondimensional analysis. Results can reveal the influence of parameters, such as drug diffusivity that may be tuned to better design novel drug release mechanisms from the nanoparticles. Moreover, when applied to a three dimensional (3D) patient-specific geometry, this tool will be able to capture essential 3D aspect of the physiological transport phenomenon more realistically, and thereby help tailor clinical strategies to individual patients. Using the temporal and spatial drug distribution data for the arterial tissue, physicians can assess treatment efficacy for a specific patient, saving potential cost of ineffective treatments.

1.6 MODELING OF COUPLED TRANSPORT OF DRUG AND DRUG-ENCAPSULATED NANOPARTICLES

In developing such a complex model that involves incorporating a multitude of physiological factors, a few practical issues from a modeling perspective need to be considered. For example, in the catheter-based lumen side delivery system, the radial release of nanoparticles in the bloodstream takes place over a few cardiac cycles, while the drug transport in the artery wall continues for days. Because of such a significant difference in time-scales, it is reasonable to confine the numerical simulations to the artery wall—decoupled from the lumen. This work, therefore, primarily focuses on the coupled transport of drug and drug-encapsulated nanoparticles in the coronary artery wall. The lumen-side contribution was incorporated in the model through appropriate boundary conditions.

It is well established that arterial wall mass transport is governed by diffusive and advective effects, and therefore can be described by linear scalar advection-diffusion equations [22-25]. However, metabolic consumption of drug by the wall tissue also plays an important role in drug transport through the artery wall. A first order reaction can be applied to incorporate this metabolic decay of drug [24, 26-28]. Furthermore, recently it has been shown [29] that realistic patient specific 3D geometry is an essential ingredient in creating physiological flow and transport features necessary for developing catheter-based drug delivery design procedures. Therefore, a comprehensive 3D advection-diffusion-reaction model to provide generality was warranted.

The various arterial wall mass transport models available in the literature deal with a variety of species, including LDL [27, 28, 30-32] as well as pure drug for local delivery by intravascular infusion through a porous membrane [33], stent-platform [23, 34, 35], and catheter [36]. To the author’s knowledge, there is no existing comprehensive 3D tool to numerically simulate coupled transport of drug and drug-encapsulated nanoparticles with application to a local drug delivery system. In previous studies, the artery wall has been modeled as either single layered [28, 30, 31, 37], or multilayered [24, 27, 32, 38-40] where it is divided into its constituent layers, namely intima, media and sometimes, adventitia. Most of these models consider the wall to be a rigid porous medium [26-28, 30-32, 34, 41] commonly using Darcy's law, or a poroelastic medium [36, 42]. For this work, at first a 3D model of a healthy idealized coronary artery—a straight cylindrical tube with a rigid homogenous wall, was considered. The model was then modified to incorporate a more sophisticated representation of wall structure that includes the intima, internal elastic lamina (IEL), the media, external elastic lamina (EEL), and the adventitia. Finally, computations were carried out on a patient-specific solid NURBS (Non-Uniform Rational B-Splines) coronary artery geometry under both healthy and diseased condition where the diseased condition was represented by the presence of a vulnerable plaque.

In the next few chapters, the coupled mathematical model will be described in detail, followed by the numerical procedures, and the artery wall geometries used to solve the mathematical problem. The results are presented in Chapters 5 and 6 while conclusions are drawn in Chapter 7.

CHAPTER 2

Mathematical Modeling

In this section, the coupled transport modeling theory for the two species will be described in detail. The conservation principle for chemical species can be represented by the following partial differential equations (PDEs)—the scalar transport equations in terms of concentrations.

2.1 THE COUPLED DRUG TRANSPORT MODEL IN CARTESIAN COORDINATES

Let Ω be an open, connected, bounded subset of $\mathbb{R}^d$, d = 2 or 3, with piecewise smooth boundary $\Gamma = \partial\Omega$, where $\partial\Omega\ (= \Gamma_D + \Gamma_N)$ is composed of the two non-overlapping parts, Γ_D and Γ_N, representing Dirichlet and Neumann boundaries, respectively. $\bar{\Omega} = \Omega + \partial\Omega$ denotes the fixed spatial domain of the problem and $\mathbf{n}$ denotes the unit normal to Γ. In the strong form, the boundary value problem can be stated as: find $C_I : \bar{\Omega} \times (0,T) \to \mathbb{R}$ and $C_{II} : \bar{\Omega} \times (0,T) \to \mathbb{R}$ such that

$$\frac{\partial C_I}{\partial t} + \nabla \cdot \left(\mathbf{u} C_I\right) - \nabla \cdot (\mathbf{K}_I \cdot \nabla C_I) + \sigma_I C_I = 0 \quad \text{in } \Omega \times (0,T), \tag{1}$$

$$\frac{\partial C_{II}}{\partial t} + \nabla \cdot \left(\mathbf{u} C_{II}\right) - \nabla \cdot (\mathbf{K}_{II} \cdot \nabla C_{II}) + \sigma_{II} C_{II} = C_I f \quad \text{in } \Omega \times (0,T), \tag{2}$$

$$C_I = g_I \quad \text{on } \Gamma_D \times (0,T), \tag{3}$$

$$C_{II} = g_{II} \quad \text{on } \Gamma_D \times (0,T), \tag{4}$$

$$\mathbf{n}\cdot(\mathbf{K}_I\cdot\nabla C_I)+\lambda_I(C_I-C_{I,\infty})=\psi_I \quad \text{on } \Gamma_\mathrm{N}\times(0,T), \tag{5}$$

$$\mathbf{n}\cdot(\mathbf{K}_{II}\cdot\nabla C_{II})+\lambda_{II}(C_{II}-C_{II,\infty})=\psi_{II} \quad \text{on } \Gamma_\mathrm{N}\times(0,T), \tag{6}$$

$$C_I(\boldsymbol{x},0)=0 \quad \text{in } \bar{\Omega}, \tag{7}$$

$$C_{II}(\boldsymbol{x},0)=0 \quad \text{in } \bar{\Omega}, \tag{8}$$

where,

C_I = Concentration of nanoparticles, number of particles/cm^3

C_{II} = Concentration of drug, gm-mole/cm^3

$\mathbf{u}$ = Velocity field in the artery wall, cm/s

$\mathbf{K}_I$ = Diffusivity tensor for the nanoparticles, cm^2/s

$\mathbf{K}_{II}$ = Diffusivity tensor for the drug, cm^2/s

σ_I = Metabolism rate constant for the nanoparticles, 1/s

σ_{II} = Metabolism rate constant for the drug, 1/s

$f=\dfrac{d\bar{M}}{dt}$ = Drug release rate by each nanoparticle, gm-mole/particle-sec

$\dfrac{\bar{M}}{\bar{M}_0}=1-\sum_n B_n\exp(-n^2\pi^2 t)$

= Fraction of drug released from each spherical nanoparticle at time t (see [43]).

Equations (1) and (2) are, respectively, the linear scalar advection-diffusion-reaction equation for drug-encapsulated nanoparticles (species *I*) and for the drug (species *II*)—both the encapsulated drug and any free drug that may be present in the formulation. Here the velocity field $\mathbf{u}(\mathbf{x},t)$ is given and assumed solenoidal, i.e., $\nabla \cdot \mathbf{u} = 0$. The term $\nabla \cdot \left(\mathbf{u}C\right)$ represents advection, that is, the velocity field that carries the scalar; the term $\partial C / \partial t$ represents accumulation, σC is the metabolic reaction term, and $\nabla \cdot (\mathbf{K} \cdot \nabla C)$ is the diffusion term. **K** can be a full, symmetric and positive-definite second order tensor representing anisotropic diffusion. There is a one-way coupling between the two transport equations through the source term $C_I f$ in Eq. (2) accounting for the rate at which drug is released from the nanoparticles.

Given an initial distribution of concentration as stated in Eqs. (7) – (8), the governing equations, Eqs. (1) – (2), can be solved subject to an appropriate set of boundary conditions. Eqs. (3) – (4) denote Dirichlet boundary conditions, and Eqs. (5) – (6) represent Robin type boundary conditions where g, C_∞, λ (mass transfer coefficient with the unit cm/s), and ψ (specified normal flux into Ω) are given functions (time-dependent in general) on the appropriate portion of the boundary with the subscripts *I* and *II* denoting the two species.

2.2 REDUCTION TO CYLINDRICAL COORDINATES

In the literature, typical physiological diffusivities are described in transmural (radial), and planar (circumferential and axial) directions (see Figure 2.1) due to the inherent cylindrical structure of the artery. In the medical device industry most in-house experiments for estimating physiological parameters and validating drug release rate models are carried out in a cylindrical coordinate setting. Furthermore, clinicians are more comfortable in interpreting results referred to a cylindrical domain, which is more intuitive. Therefore the mathematical model described in Eqs. (1) – (6) was transformed to cylindrical coordinates.

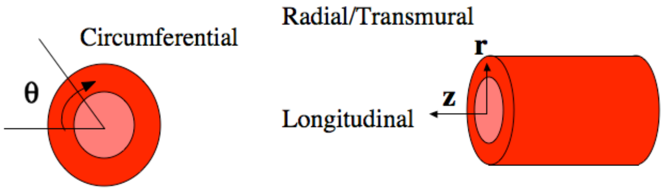

Figure 2.1: Cylindrical coordinate system.

This section will describe the coupled drug transport modeling theory in cylindrical coordinates with appropriate boundary conditions. The mathematical model can be described in four parts as follows.

2.2.1 Modeling of drug transport

The governing equations for the coupled drug transport model can be expressed in cylindrical coordinates as follows

$$\begin{aligned}\frac{\partial C_I}{\partial t} = {} & \frac{1}{r}\frac{\partial}{\partial r}\left(D_{r,I}\, r\frac{\partial C_I}{\partial r}\right) + \frac{1}{r^2}\frac{\partial}{\partial \theta}\left(D_{\theta,I}\frac{\partial C_I}{\partial \theta}\right) + \frac{\partial}{\partial z}\left(D_{z,I}\frac{\partial C_I}{\partial z}\right) \\ & -\left[\frac{1}{r}\frac{\partial (r V_r C_I)}{\partial r} + \frac{1}{r}\frac{\partial (V_\theta C_I)}{\partial \theta} + \frac{\partial (V_z C_I)}{\partial z}\right] - \sigma_I C_I\end{aligned} \tag{9}$$

$$\begin{aligned}\frac{\partial C_{II}}{\partial t} = {} & \frac{1}{r}\frac{\partial}{\partial r}\left(D_{r,II}\, r\frac{\partial C_{II}}{\partial r}\right) + \frac{1}{r^2}\frac{\partial}{\partial \theta}\left(D_{\theta,II}\frac{\partial C_{II}}{\partial \theta}\right) + \frac{\partial}{\partial z}\left(D_{z,II}\frac{\partial C_{II}}{\partial z}\right) \\ & -\left[\frac{1}{r}\frac{\partial (r V_r C_{II})}{\partial r} + \frac{1}{r}\frac{\partial (V_\theta C_{II})}{\partial \theta} + \frac{\partial (V_z C_{II})}{\partial z}\right] - \sigma_{II} C_{II} + C_I f\end{aligned} \tag{10}$$

Omitting subscripts I and II for simplicity, D_r, D_θ, and D_z are the diffusivities of the respective species in radial, circumferential, and axial directions, respectively, such that $D_{i,j} = D^0_{i,j}\varphi_i(\mathbf{r}, t)$, where $i = r,\theta,z$ and $j = I, II$. Similarly, V_r, V_θ, and V_z are the corresponding advective velocities in the artery wall such that, $V_i = V_{i,0}\varphi_i(\mathbf{r},t)$, where $i = r,\theta,z$. The thickness of the artery wall is denoted b. Here, D^0_i and $V_{i,0}$ are reference values of the diffusivity and the advective velocity, respectively, and $\varphi_i(\mathbf{r},t)$ is a space and time varying function accounting for the spatial and temporal variation of these quantities. A physical assumption has been made here that the diffusivity tensor has principle directions in the $r,\theta,$ and z coordinate directions (see Eq. (31)) in accordance with the experimental data available in the literature where it has been cited that diffusion in the circumferential and axial directions is faster than that in the radial direction for typical drugs of interest (see Chapter 4).

The governing equations (9) and (10) are derived for the most general case in 3D cylindrical coordinates. The first three terms represent diffusion of scalars in r,θ and z direction respectively. These are followed by three terms describing transport by advection in the three coordinate directions. The seventh term, that is the reaction term, denotes metabolic decay of drug in the tissue. Identical to their Cartesian counterparts, the two transport equations are coupled through the source term $C_I f$.

In the numerical examples presented later (see Section 5.1), a dimensionless form of the model will be used. To derive the dimensionless equations, the following definitions of non-dimensional space and time were adopted.

$$r^* = \frac{r}{b}, \qquad t^* = \frac{tb^2}{D^0_{r,II}} \tag{11}$$

In the dimensionless coordinates, the governing equations become

$$\begin{aligned}\frac{\partial C^*_I}{\partial t^*} &= \frac{1}{r^*}\frac{\partial}{\partial r^*}\left(D^*_{r,I} r^* \frac{\partial C^*_I}{\partial r^*}\right) + \frac{1}{r^{*2}}\frac{\partial}{\partial \theta}\left(D^*_{\theta,I}\frac{\partial C^*_I}{\partial \theta}\right) + \frac{\partial}{\partial z^*}\left(D^*_{z,I}\frac{\partial C^*_I}{\partial z^*}\right) \\ &\quad -Pe\left[\frac{1}{r^*}\frac{\partial (r^* V^*_r C^*_I)}{\partial r^*} + \frac{1}{r^*}\frac{\partial (V^*_\theta C^*_I)}{\partial \theta} + \frac{\partial (V^*_z C^*_I)}{\partial z^*}\right] - Da_I C^*_I\end{aligned} \tag{12}$$

$$\begin{aligned}\frac{\partial C^*_{II}}{\partial t^*} &= \frac{1}{r^*}\frac{\partial}{\partial r^*}\left(D^*_{r,II} r^* \frac{\partial C^*_{II}}{\partial r^*}\right) + \frac{1}{r^{*2}}\frac{\partial}{\partial \theta}\left(D^*_{\theta,II}\frac{\partial C^*_{II}}{\partial \theta}\right) + \frac{\partial}{\partial z^*}\left(D^*_{z,II}\frac{\partial C^*_{II}}{\partial z^*}\right) \\ &\quad -Pe\left[\frac{1}{r^*}\frac{\partial (r^* V^*_r C^*_{II})}{\partial r^*} + \frac{1}{r^*}\frac{\partial (V^*_\theta C^*_{II})}{\partial \theta} + \frac{\partial (V^*_z C^*_{II})}{\partial z^*}\right] - Da_{II} C^*_{II} + C^*_I f^*\end{aligned} \tag{13}$$

where,

$$\text{Peclet Number, } Pe = \frac{V_{r,0} b}{D^0_{r,II}}; \tag{14}$$

and

$$\text{Damkohler Numbers, } Da_I = \frac{\sigma_I b^2}{D^0_{r,II}}, \text{ and } Da_{II} = \frac{\sigma_{II} b^2}{D^0_{r,II}}. \tag{15}$$

Here the concentration of the nanoparticles C_I, was non-dimensionalized by the initial concentration of nanoparticles in the formulation $C_{I,0}$, while that for the drug C_{II} was non-dimensionalized by the initial concentration of free drug in the formulation $C_{II,0}$. The non-dimensionalized variables are listed in Table 2.1.

Table 2.1: Nondimensional variables used

Notation	Definition
r^*	$r \,/\, b$
t^*	$tb^2 \,/\, D^0_{r,II}$
C^*_I	$C_I \,/\, C_{I,0}$
C^*_{II}	$C_{II} \,/\, C_{II,0}$
$D^*_{r,I}$	$D_{r,I} \,/\, D^0_{r,II}$
$D^*_{\theta,I}$	$D_{\theta,I} \,/\, D^0_{r,II}$
$D^*_{z,I}$	$D_{z,I} \,/\, D^0_{r,II}$
$D^*_{r,II}$	$D_{r,II} \,/\, D^0_{r,II}$
$D^*_{\theta,II}$	$D_{\theta,II} \,/\, D^0_{r,II}$
$D^*_{z,II}$	$D_{z,II} \,/\, D^0_{r,II}$
V^*_r	$V_r \,/\, V_{r,0}$
V^*_θ	$V_\theta \,/\, V_{r,0}$
V^*_z	$V_z \,/\, V_{r,0}$
$C^*_I f^*$	$\frac{C_I}{C_{I,0}} f \frac{C_{I,0}}{C_{II,0}} \frac{b^2}{D^0_{r,II}}$

2.2.2 Modeling of drug release rate from nanoparticles

Drug release from the nanoparticles was assumed to occur solely by diffusion. A biphasic diffusion model [44], originally devised for predicting drug release from a drug eluting stent (DES) coating [45], was adopted and extended to polymeric nanoparticles as the drug concentration in the polymer within the nanoparticles is sufficiently high. This biphasic model is based on the assumption that transport through the dispersed drug phase within the nanoparticles takes place via two discrete modes – the fast mode and the slow mode. The fast mode is the release of drug from highly percolated structure of drug phase within the polymer, and the slow mode is the release of drug from a non-percolated polymer-encapsulated phase of the drug. The model has been previously validated against experimental data and the assumption of biphasic state of drug phase encapsulated within polymer has been corroborated [45], making this concept a natural choice for modeling the drug release rate from the polymeric nanoparticles.

This biphasic drug release rate model developed for the monodisperse case (i.e., same-sized particles) was further enhanced and extended to the polydisperse case (nanoparticles in the formulation having a range of particle sizes). The biphasic drug release rate model for the polydisperse case is

$$\begin{aligned}\frac{M}{M_0} &= \sum_i \alpha_i f_1 \left\{1 - \sum_n \frac{6}{n^2\pi^2} e^{-n^2\pi^2 t D_1 / R_i^2}\right\} \\ &\quad + \sum_i \alpha_i (1 - f_1) \left\{1 - \sum_n \frac{6}{n^2\pi^2} e^{-n^2\pi^2 t D_2 / R_i^2}\right\}\end{aligned} \tag{16}$$

where, M/M_0 is the percent release of drug from all the nanoparticles at time t with M_0 denoting the total weight of drug encapsulated in all the nanoparticles, N_0 (total number of nanoparticles). Consequently, the nondimensionalized drug release rate is given by:

$$\begin{aligned}f^* &= \frac{dM / M_0}{dt^*} = f \frac{C_{I,0}}{C_{II,0}} \frac{b^2}{D^0_{r,II}} \\ &= \frac{6}{D^0_{r,II} / b^2} \left[\sum_i \alpha_i f_1 \frac{D_1}{R_i^2} \sum_n e^{-n^2\pi^2 t D_1 / R_i^2} + \sum_i \alpha_i (1 - f_1) \frac{D_2}{R_i^2} \sum_n e^{-n^2\pi^2 t D_2 / R_i^2} \right]\end{aligned} \tag{17}$$

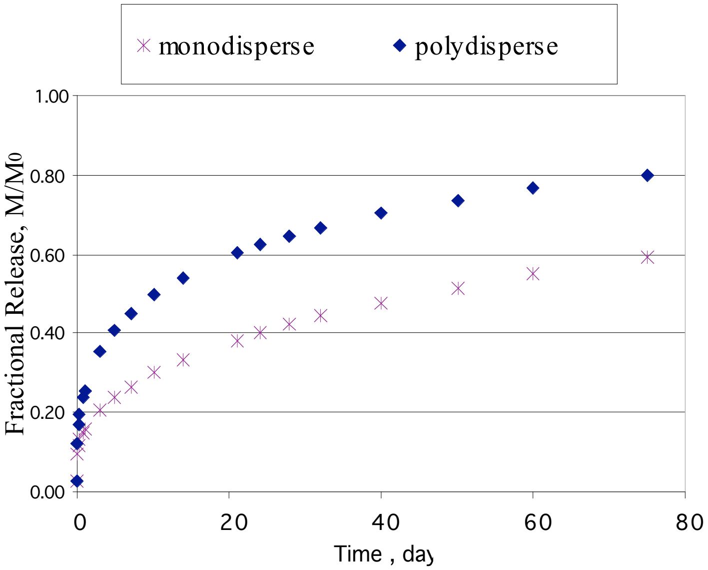

Figure 2.2: Predictive values of drug release from nanoparticles for monodisperse and polydisperse case. [44]

There are three major design parameters, effective diffusivity of slow drug D_1, effective diffusivity of fast drug D_2, and fraction of drug in slow phase f_1, which by manipulating one can obtain a desired release rate profile. Additionally, the drug release rate (RR) can be tailored by mixing different sizes of nanoparticles in the polydisperse case, which provides two additional design parameters, R, the size of the i^{th} nanoparticle in the mixture, and α_i, the fraction by weight of the i^{th} nanoparticle in the formulation. This adds to the flexibility in designing an optimum release rate for a desired drug distribution.

2.2.3 Boundary conditions

To determine appropriate boundary conditions for the lumen side boundary, the following physiological phenomena were considered.

- The loss of particles and free drug accumulated in the wall due to their exposure to blood flow in the lumen that tends to wash them away from the wall into the bloodstream.
- Their propensity to stick/un-stick to the wall depending on the reaction rate (sticking coefficient) for the particular species.
- And finally, the solubility of the particles in the tissue compared to the blood serum through partition coefficients for each species. It is a measure of differential solubility of the chemical substance between two solvents where one of the solvents chosen is typically water. Hence the partition coefficient normally indicates how hydrophilic or hydrophobic a chemical substance is.

The above physiological phenomena were modeled as follows (see Figure 2.3).

Lumen side (at 1):

$$\frac{\partial C_I^{+^*}}{\partial t^*} = K_I' C_I^{-^*} - K_I'' C_I^{+^*} \tag{18}$$

where,

$$C_I^{-^*} = \frac{C_I^-}{C_{I,0}^-} = \exp\left\{\left(-\frac{k_{m,I} b^2}{D_{r,II}^0} \frac{Factor}{h}\right) t^*\right\} \tag{19}$$

and

$$Factor = \frac{A_0 + A_0^{'}}{A_0} \tag{20}$$

Solving for C_I^{+*} gives,

$$\begin{aligned} C_I^{+*} &= \frac{K_I'}{K_I'' - K_I^{+}}\{\exp(-K_I^{+}t^{*}) - \exp(K_I'')\}, \\ \text{where } K_I^{+} &= \frac{k_{m,I}b^2}{D_{II}^{0}}\frac{Factor}{h} \end{aligned} \tag{21}$$

such that, nanoparticle concentration at the lumen-side boundary,

$$C_I^{*}\Big|_1 = C_I^{+*} \tag{22}$$

Similarly the loss of drug to blood flow at the lumen-side boundary is modeled as,

$$C_{II}^{-*} = \frac{C_{II}^{-}}{C_{II,0}^{-}} = \exp\left\{\left(-\frac{k_{m,II}b^2}{D_{r,II}^{0}}\frac{Factor}{h}\right)t^{*}\right\} \tag{23}$$

from which it follows,

$$C_{II}^{+*} = C_{II}^{-*} = exp\left\{\left(-\frac{k_{m,II}b^2}{D_{r,II}^{0}}\frac{Factor}{h}\right)t^{*}\right\} \tag{24}$$

After partitioning into the tissue, the drug concentration at the lumen-side boundary becomes,

$$C_{II}^{*}\Big|_1 = \bar{P}_{II}C_{II}^{+*} \tag{25}$$

where, $\bar{P}_{II}$ is the drug tissue partition coefficient.

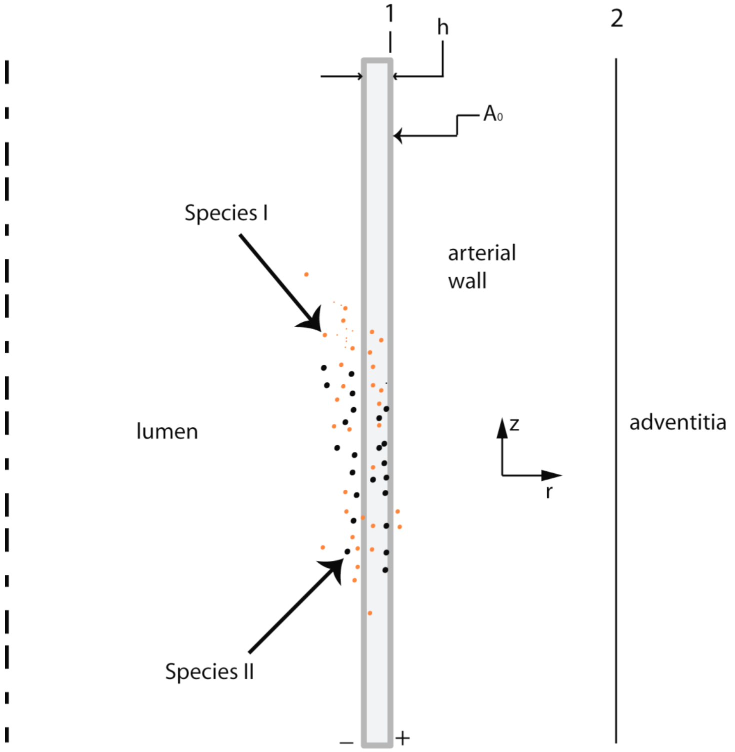

Figure 2.3: Schematic diagram of the cross-section of an artery to explain the boundary conditions.

Adventitia-side (at 2):

$$-D^*_{r,I}\left.\frac{\partial C^*_I}{\partial r^*}\right|_2 = \frac{k_{m,I}b}{D^0_{r,II}}\left(C^*_I\big|_2 - C^*_{I,\infty}\right) \tag{26}$$

$$-D^*_{r,II}\left.\frac{\partial C^*_{II}}{\partial r^*}\right|_2 = \frac{k_{m,II}b}{D^0_{r,II}}\left(C^*_{II}\big|_2 - C^*_{II,\infty}\right) \tag{27}$$

Here,

K'_I = Forward reaction rate (sticking) for the nanoparticles, 1/s

K''_I = Backward reaction rate (un-sticking) for the nanoparticles, 1/s

$\overline{P}_{II}$ = Partition coefficient for the drug

$k_{m,I}$ = Mass transport coefficient for the nanoparticles, cm/s

$k_{m,II}$ = Mass transport coefficient for the drug, cm/s

$C_{I,\infty}$ = Concentration of nanoparticle in the adventitia, gm-mole/ cm^3

$C_{II,\infty}$ = Concentration of drug in the adventitia, gm-mole/ cm^3

Remarks:

1. The expressions for exponential loss at the lumen side, Eq. (19) for the nanoparticles and Eq. (23) for the drug, were obtained by applying unsteady state mass balance for the nanoparticles and the drug in the thin film volume of thickness *h* and an area A_0 at the lumen side boundary (see Figure 2.3), and then analytically solving for concentrations with appropriate boundary conditions.
2. In determining the lumen-side boundary condition for the nanoparticles, it was assumed that backward reaction rate in Eq. (18) is considerably slower compared to the forward reaction rate or the sticking coefficient.
3. For the adventitia-side boundary, a Robin type boundary condition was implemented as presented in Eqs. (26) – (27). As $k_m \rightarrow \infty$, it reduces to a sink boundary condition. Similarly as $k_m \rightarrow 0$ it becomes a flux boundary condition.

2.2.4 Modeling of solute permeation across tissue (IEL) barrier

The species transport across the internal elastic lamina (IEL) between the two homogeneous parts, the intima and the media, were simulated by implementing Kedem and Katchalsky's model for solute transport across tissue barrier [46]. Assuming quasi-steady state, that is, the time for the solute to diffuse across this membrane is much faster than the time for the solute concentration to change on either side of the membrane, the solute transport can be described as follows:

$$J_s = J_v(1-\sigma_i)\frac{C_1 + C_2}{2} + P(C_1 - C_2) \tag{28}$$

where,

J_s = solute flux per unit area, cm/s

J_v = filtration rate or flow of solute, cm/s

σ_i = reflection or retardation factor

C_1 = solute concentration in solvent on the intima side (normalized)

C_2 = solute concentration in solvent on the media side (normalized)

P = diffusive permeability of the membrane to the solute, cm/s

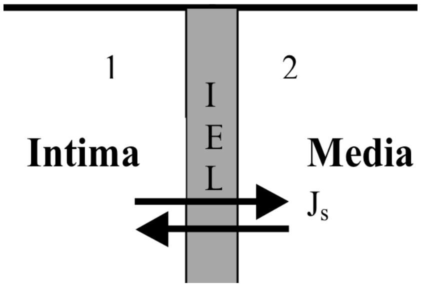

Figure 2.4: Modeling of species transport across the IEL barrier.

The permeability P is related to the diffusion coefficient of the membrane, D_m and the thickness of the barrier, L as follows:

$$P = \frac{\bar{K} D_m}{L} \tag{29}$$

where $\bar{K}$ is the partition coefficient. Eq. (28) accounts for both diffusive and advective transport. When Peclet number, Pe is less than 1.2, the advective contribution can be neglected [46]. In the intima the species transport is highly diffusion dominated, that is, $Pe < 1$. Hence Eq. (28) for the solute flux across the IEL becomes:

$$J_s = P(C_1 - C_2) \tag{30}$$

2.3 JUSTIFICATION FOR THE VELOCITY VECTOR AND THE DIFFUSIVITY TENSOR

The physiological diffusivities D_r, D_θ, and D_z, provided by the medical device design community can be converted to a diffusion tensor **K** in Cartesian coordinate using the formulae presented here. Computations can then be carried out in Cartesian coordinates suitable for complex geometries, using the numerical procedures detailed in Chapter 3.

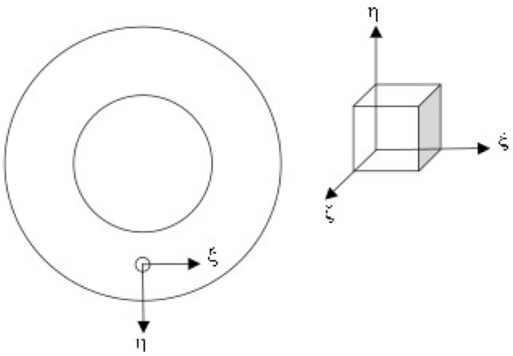

Figure 2.5: Transition from cylindrical to Cartesian coordinates.

The diagonal diffusion tensor in cylindrical coordinate, $\mathbf{D}$ is defined as

$$\mathbf{D} = \begin{bmatrix} D_\theta & 0 & 0 \\ 0 & D_r & 0 \\ 0 & 0 & D_z \end{bmatrix}. \tag{31}$$

The circumferential, radial and axial directions in cylindrical coordinates are associated with corresponding ξ, η and ζ directions, respectively, in the Cartesian description of the geometry. The resulting full 3 by 3 diffusion tensor in Cartesian coordinates thus becomes

$$\mathbf{K} = \hat{\mathbf{J}}\mathbf{D}\hat{\mathbf{J}}^T \tag{32}$$

where,

$$\hat{\mathbf{J}} = \mathrm{orth}(\mathbf{J}) = \left[\hat{\mathbf{J}}_1, \hat{\mathbf{J}}_2, \hat{\mathbf{J}}_3\right], \tag{33}$$

and the Jacobian,

$$\mathbf{J} = \left[\frac{\partial \underset{\sim}{\mathbf{X}}}{\partial \xi}, \frac{\partial \underset{\sim}{\mathbf{X}}}{\partial \eta}, \frac{\partial \underset{\sim}{\mathbf{X}}}{\partial \zeta}\right] = \left[\mathbf{J}_1, \mathbf{J}_2, \mathbf{J}_3\right]. \tag{34}$$

Similarly, the advective velocity vector becomes,

$$\mathbf{u} = \hat{\mathbf{J}}\mathbf{V} \tag{35}$$

where,

$$\mathbf{V} = \left[V_r, V_\theta, V_z\right]. \tag{36}$$

In the above formulation, $\mathbf{J}$ is the Jacobian as defined in Eq. (34). The column vectors of the Jacobian are orthonormalized according to the Gram-Schmidt process, which is expressed in Eq. (33). The corresponding advective velocities in Cartesian coordinates are obtained through a rotation, as in Eq. (35).

Remark:

1. Procedures outlined in Eqs. (31) – (36) are simple to carry out in the isogeometric discretization due to the suitable parametric definition of the geometry. On the other hand, extracting this information from a general, 3D, unstructured hexahedral or tetrahedral mesh is not a simple task. This property makes the NURBS-based approach well suited for arterial drug delivery.

CHAPTER 3

Numerical Formulation

3.1 WEAK FORM OF THE CONTINUOUS PROBLEM

Let $\mathcal{S}$ denote the trial solution and $\mathcal{V}$ weighting function spaces. Defining the solution and the weighting function spaces as:

$$\mathcal{S} = \mathcal{S}_t = \{C(\cdot,t) \mid C(t) \equiv C(\cdot,t) \in H^1(\Omega), C(\mathbf{x},t) = g(\mathbf{x},t), \mathbf{x} \in \Gamma_g\} \tag{37}$$

$$\mathcal{V} = \{w \mid w \in H^1(\Omega), w = 0 \quad \text{on } \Gamma\} \tag{38}$$

respectively, the variational counterparts of (1) – (8) read: find $C_I(t) \in \mathcal{S},\ t \in [0,T]$ and $C_{II}(t) \in \mathcal{S},\ t \in [0,T]$ such that

$$B_I(w_I, C_I) = L_I(w_I), \tag{39}$$

$$\begin{aligned} B_{II}(w_{II}, C_{II}; C_I) &= B_{II}^1(w_{II}, C_{II}) + B_{II}^2(w_{II}, C_I) \\ &= L_{II}(w_{II}), \end{aligned} \tag{40}$$

with

$$\begin{aligned} B_I(w_I, C_I) = (w_I, &\frac{\partial C_I}{\partial t} + \mathbf{u} \cdot \nabla C_I + \sigma_I C_I)_\Omega \\ &+ (\nabla w_I, \mathbf{K}_I \cdot \nabla C_I)_\Omega + (w_I, \lambda_I C_I)_{\Gamma_N}, \end{aligned} \tag{41}$$

$$L_I(w_I) = (w_I, \psi_I + \lambda_I C_{I,\infty})_{\Gamma_N}, \tag{42}$$

and

$$B_{II}^1(w_{II}, C_{II}) = (w_{II}, \frac{\partial C_{II}}{\partial t} + \mathbf{u} \cdot \nabla C_{II} + \sigma_{II} C_{II})_{\Omega} \\ +(\nabla w_{II}, \mathbf{K}_{II} \cdot \nabla C_{II})_{\Omega} + (w_{II}, \lambda_{II} C_{II})_{\Gamma_N}, \tag{43}$$

$$B_{II}^2(w_{II}, C_I) = -(w_{II}, C_I f)_{\Omega}, \tag{44}$$

$$L_{II}(w_{II}) = (w_{II}, \psi_{II} + \lambda_{II} C_{II,\infty})_{\Gamma_N}, \tag{45}$$

$\forall w_I \in \mathcal{V}$ and $\forall w_{II} \in \mathcal{V}$. Here $(\cdot,\cdot)_Q$ denotes the L^2-inner product on $Q = \{\Omega, \Gamma\}$.

3.2 DISCRETIZATION

Let $\mathcal{S}^h \subset S$ and $\mathcal{V}^h \subset \mathcal{V}$ be the finite-dimensional spaces of trial solutions and weighting functions, respectively. The semi-discrete formulation for the coupled linear advection-diffusion-reaction problem is stated as follows: find $C_I^h(t) \in \mathcal{S}^h$ and $C_{II}^h(t) \in \mathcal{S}^h$ such that $\forall w_I \in \mathcal{V}^h$ and $\forall w_{II} \in \mathcal{V}^h$

$$B_I^{MS}(w_I^h, C_I^h) - L_I^{MS}(w_I^h) = 0, \tag{46}$$

$$B_{II}^{MS}(w_{II}^h, C_{II}^h; C_I^h) - L_{II}^{MS}(w_{II}^h) = 0, \tag{47}$$

where

$$B_I^{MS}(w_I^h, C_I^h) = B_I(w_I^h, C_I^h) \\ +\sum_{e=1}^{n_{el}} (\mathbf{u} \cdot \nabla w_I^h + (\nabla \cdot \mathbf{u}) w_I^h - \sigma_I w_I^h) \tau_I, \mathbf{r}_I(C_I^h))_{\Omega_e}, \tag{48}$$

$$L_I^{MS}(w_I^h) = L_I(w_I^h), \tag{49}$$

and,

$$B_{II}^{MS}(w_{II}^h, C_{II}^h; C_I^h) = B_{II}(w_{II}^h, C_I^h; C_{II}^h) \\ +\sum_{e=1}^{n_{el}} (\mathbf{u} \cdot \nabla w_{II}^h + (\nabla \cdot \mathbf{u}) w_{II}^h - \sigma_{II} w_{II}^h) \tau_{II}, \mathbf{r}_{II}(C_{II}^h; C_I^h))_{\Omega_e}, \tag{50}$$

$$L_{II}^{MS}(w_{II}^h) = L_{II}(w_{II}^h), \tag{51}$$

Here the residuals $\mathbf{r}_I$ and $\mathbf{r}_{II}$ are defined as

$$\mathbf{r}_I(C_I^h) = \frac{\partial C_I^h}{\partial t} + \mathbf{u}.\nabla C_I^h - \nabla\cdot(\boldsymbol{K}_I \cdot \nabla C_I^h) + \sigma_I C_I^h, \tag{52}$$

$$\mathbf{r}_{II}(C_{II}^h; C_I^h) = \frac{\partial C_{II}^h}{\partial t} + \mathbf{u}.\nabla C_{II}^h - \nabla\cdot(\boldsymbol{K}_{II} \cdot \nabla C_{II}^h) + \sigma_{II} C_{II}^h - C_I^h f. \tag{53}$$

Eqs. (46) – (53) represent a stabilized formulation of advection-diffusion-reaction, in which

$$\tau_I = (4/\triangle t^2 + {\sigma_I}^2 + \mathbf{u}\cdot\mathbf{G}\mathbf{u} + \mathbf{G}'_I : \mathbf{G}'_I)^{-1/2}, \tag{54}$$

$$\tau_{II} = (4/\triangle t^2 + {\sigma_{II}}^2 + \mathbf{u}\cdot\mathbf{G}\mathbf{u} + \mathbf{G}'_{II} : \mathbf{G}'_{II})^{-1/2}, \tag{55}$$

are the so called stabilization parameters where the tensors $\mathbf{G}$ and $\mathbf{G}'$ are defined as follows

$$\mathbf{G} = \left(\frac{\partial \boldsymbol{\xi}}{\partial \boldsymbol{x}}\right)^T \frac{\partial \boldsymbol{\xi}}{\partial \boldsymbol{x}}, \tag{56}$$

$$\mathbf{G}'_I = \frac{\partial \boldsymbol{\xi}}{\partial \boldsymbol{x}} \mathbf{K}_I \left(\frac{\partial \boldsymbol{\xi}}{\partial \boldsymbol{x}}\right)^T, \tag{57}$$

$$\mathbf{G}'_{II} = \frac{\partial \boldsymbol{\xi}}{\partial \boldsymbol{x}} \mathbf{K}_{II} \left(\frac{\partial \boldsymbol{\xi}}{\partial \boldsymbol{x}}\right)^T. \tag{58}$$

$\frac{\partial \boldsymbol{\xi}}{\partial \boldsymbol{x}}$ is the inverse Jacobian of the element mapping between the parent and the current coordinates of the physical domain and $\triangle t$ is the time step. This stabilization is appropriate for the window of Peclet numbers under consideration that can range from 0.1 to 1000 depending on the tissue properties of the artery wall under healthy and diseased condition (see Chapter 4).

Spatial discretization of the one-way coupled problem makes use of isogeometric analysis based on NURBS, an alternative to standard finite elements, proposed by Hughes et al. [47, 48].

Let,

$$\{N_A(\boldsymbol{x})\}_{A \in J}, \ \boldsymbol{x} \in \Omega \tag{59}$$

denote a set of basis functions defined on all of Ω to be used for the drug representations as follows

$$C_I^h(\boldsymbol{x}, t) = \sum_{A \in J} N_A(\boldsymbol{x}) C_{I,A}(t) \tag{60}$$

$$C_{II}^h(\boldsymbol{x}, t) = \sum_{A \in J} N_A(\boldsymbol{x}) C_{II,A}(t) \tag{61}$$

Likewise,

$$w_I^h(\boldsymbol{x}) = \sum_A N_A(\boldsymbol{x}) W_{I,A} \qquad \text{and} \qquad w_{II}^h(\boldsymbol{x}) = \sum_A N_A(\boldsymbol{x}) W_{II,A}, \tag{62}$$

where again N_A's are NURBS basis functions; and $C_{I,A}$, $C_{II,A}$, $\mathrm{W}_{I,A}$ and $\mathrm{W}_{II,A}$ are the associated control variables. This reduces to usual shape functions and degrees of freedom when classical finite elements are utilized.

Let $\dot{\mathbf{C}}_I = \{\dot{C}_I\}$ and $\dot{\mathbf{C}}_{II} = \{\dot{C}_{II}\}$ denote the vectors of degrees of freedom of time derivatives, and $\mathbf{C}_I = \{C_I\}$ and $\mathbf{C}_{II} = \{C_{II}\}$ represent the vectors of degrees of freedom of concentration for species *I* and *II*, respectively. The above discretization when combined with the formulation of (46) – (58) yields two residual vectors defined as

$$\mathbf{R}^{np} = \{R_A^{np}\} \tag{63}$$

$$\mathbf{R}^{drug} = \{R_A^{drug}\} \tag{64}$$

$$R_A^{np}(\dot{\mathbf{C}}_I, \mathbf{C}_I) = B_I^{MS}(N_A, C_I^h) - L_I^{MS}(N_A), \tag{65}$$

$$R_A^{drug}(\dot{\mathbf{C}}_{II}, \mathbf{C}_{II}; \mathbf{C}_I) = B_{II}^{MS}(N_A, C_{II}^h; C_I^h) - L_{II}^{MS}(N_A), \tag{66}$$

where R_A^{np} and R_A^{drug} represent the nanoparticle and drug transport residuals for the A^{th} basis function, respectively.

3.3 TIME INTEGRATION AND NUMERICAL IMPLEMENTATION

With the equations in semi-discrete form, a time integration scheme is introduced, namely, the generalized-α method proposed by Chung and Hulbert [49] and Jansen, Whiting and Hulbert [50]. This method seeks to solve the system for time t_{n+1} given the computed quantities at time t_n such that the nonlinear residuals vanish at intermediate times. That is, it seeks to satisfy

$$R_A^{np}(\dot{\mathbf{C}}_I^{n+\alpha_m}, \mathbf{C}_I^{n+\alpha_f}) = 0 \tag{67}$$

$$R_A^{drug}(\dot{\mathbf{C}}_{II}^{n+\alpha_m}, \mathbf{C}_{II}^{n+\alpha_f}; \mathbf{C}_I^{n+\alpha_f}) = 0 \tag{68}$$

Here the intermediate time steps are defined as

$$(\cdot)^{n+\alpha_m} = (\cdot)^n + \alpha_m((\cdot)^{n+1} - (\cdot)^n) \tag{69}$$

$$(\cdot)^{n+\alpha_f} = (\cdot)^n + \alpha_f((\cdot)^{n+1} - (\cdot)^n) \tag{70}$$

A one-parameter family of second-order accurate and unconditionally stable time integration schemes is obtained by defining γ employing the following parameterization of the intermediate time levels:

$$\gamma = \frac{1}{2} - \alpha_f + \alpha_m, \tag{71}$$

$$\alpha_f \geq \alpha_m \geq \frac{1}{2}, \tag{72}$$

The parameters α_m and α_f are chosen in order to ensure accuracy and stability of the method. For first-order equations in time, Chung and Hulbert in [49] demonstrated that the method is second-order accurate and unconditionally stable given the following conditions.

$$\alpha_m = \frac{1}{2}\left(\frac{3-\rho_\infty}{1+\rho_\infty}\right) \quad , \tag{73}$$

$$\alpha_f = \frac{1}{1+\rho_\infty}, \tag{74}$$

where the parameter $\rho_\infty \in [0,1]$ is the spectral radius of the amplification matrix as $\triangle t \rightarrow \infty$ that controls high frequency damping [50].

Although the underlying equations are linear in $\mathbf{C}_I$ and $\mathbf{C}_{II}$, the following predictor-corrector solution strategy is used with a single corrector step.

Predictor stage: Set

$$\mathbf{C}_I^{n+1} = \mathbf{C}_I^n \tag{75}$$

$$\dot{\mathbf{C}}_I^{n+1} = \frac{\gamma - 1}{\gamma}\dot{\mathbf{C}}_I^n \tag{76}$$

Corrector stage:

- Evaluate at the α-levels

$$\dot{\mathbf{C}}_I^{n+\alpha_m} = \dot{\mathbf{C}}_I^n + \alpha_m(\dot{\mathbf{C}}_I^{n+1} - \dot{\mathbf{C}}_I^n) \tag{77}$$

$$\mathbf{C}_I^{n+\alpha_f} = \mathbf{C}_I^n + \alpha_f(\mathbf{C}_I^{n+1} - \mathbf{C}_I^n) \tag{78}$$

- Use these α-level values to assemble the residual and the tangent matrix of the linear system and then solve for $\Delta\dot{\mathbf{C}}_I^{n+1}$ using a preconditioned GMRES (Generalized Minimal Residual Method) algorithm (see Saad and Shultz [51]) to a specified tolerance.

$$\frac{\partial \mathbf{R}^{np}(\dot{\mathbf{C}}_I^{n+\alpha_m}, \mathbf{C}_I^{n+\alpha_f})}{\partial \dot{\mathbf{C}}_I^{n+1}}\Delta\dot{\mathbf{C}}_I^{n+1} = -\mathbf{R}^{np}(\dot{\mathbf{C}}_I^{n+\alpha_m}, \mathbf{C}_I^{n+\alpha_f}) \tag{79}$$

- Use $\Delta\dot{\mathbf{C}}_I^{n+1}$ to update $\dot{\mathbf{C}}_I^{n+1}$ and $\mathbf{C}_I^{n+1}$ as

$$\dot{\mathbf{C}}_I^{n+1} = \dot{\mathbf{C}}_I^{n+1} + \Delta\dot{\mathbf{C}}_I^{n+1}, \tag{80}$$

$$\mathbf{C}_I^{n+1} = \mathbf{C}_I^{n+1} + (\gamma\Delta t)\Delta\dot{\mathbf{C}}_I^{n+1}, \tag{81}$$

At this point a nanoparticle field is calculated at the next time step. Now the drug concentration is obtained as

Predictor stage: Set

$$\mathbf{C}_{II}^{n+1} = \mathbf{C}_{II}^{n} \tag{82}$$

$$\dot{\mathbf{C}}_{II}^{n+1} = \frac{\gamma - 1}{\gamma}\dot{\mathbf{C}}_{II}^{n} \tag{83}$$

Corrector stage:

- Evaluate at the α-levels

$$\dot{\mathbf{C}}_{II}^{n+\alpha_m} = \dot{\mathbf{C}}_{II}^{n} + \alpha_m(\dot{\mathbf{C}}_{II}^{n+1} - \dot{\mathbf{C}}_{II}^{n}) \tag{84}$$

$$\mathbf{C}_{II}^{n+\alpha_f} = \mathbf{C}_{II}^{n} + \alpha_f(\mathbf{C}_{II}^{n+1} - \mathbf{C}_{II}^{n}) \tag{85}$$

- Take $\mathbf{C}_{I}^{n+1}$ from (81) to get

$$\mathbf{C}_{I}^{n+\alpha_f} = \mathbf{C}_{I}^{n} + \alpha_f(\mathbf{C}_{I}^{n+1} - \mathbf{C}_{I}^{n}) \tag{86}$$

- Use these α-level values to assemble the residual and the tangent matrix of the linear system and then solve for $\Delta\dot{\mathbf{C}}_{II}^{n+1}$ using a preconditioned GMRES algorithm to a specified tolerance.

$$\frac{\partial \mathbf{R}^{drug}(\dot{\mathbf{C}}_{II}^{n+\alpha_m}, \mathbf{C}_{II}^{n+\alpha_f}; \mathbf{C}_{II}^{n+\alpha_f})}{\partial \dot{\mathbf{C}}_{II}^{n+1}} \Delta\dot{\mathbf{C}}_{II}^{n+1} = -\mathbf{R}^{drug}(\dot{\mathbf{C}}_{II}^{n+\alpha_m}, \mathbf{C}_{II}^{n+\alpha_f}; \mathbf{C}_{I}^{n+\alpha_f}) \tag{87}$$

- Use $\Delta\dot{\mathbf{C}}_{II}^{n+1}$ to update the drug solution to the next time step

$$\dot{\mathbf{C}}_{II}^{n+1} = \dot{\mathbf{C}}_{II}^{n+1} + \Delta\dot{\mathbf{C}}_{II}^{n+1}, \tag{88}$$

$$\mathbf{C}_{II}^{n+1} = \mathbf{C}_{II}^{n+1} + (\gamma\triangle t)\Delta\dot{\mathbf{C}}_{II}^{n+1}, \tag{89}$$

It may be worth noting that the residuals in (67) and (68) are evaluated at intermediate time steps while the derivatives in (79) and (87) are taken at time step $n+1$.

CHAPTER 4

Parameter Selection and Solution Approach

4.1 MODELING CONSIDERATIONS FOR THE ARTERY WALL GEOMETRY

Coronary artery walls are multilayered with distinct features present in each homogenous component. When an artery becomes diseased, it undergoes significant changes morphologically that affect material and hence transport properties. In this section the salient features of a healthy and a diseased artery wall are described as a prelude to approaching the central theme of this chapter, that is, the selection of relevant parameters for both healthy and diseased artery cases presented in Section 4.2.

4.1.1 Healthy artery

Figure 4.1 shows a typical artery wall composition in detail. An appreciable amount of specialization is evident even at this macro level:

- **Endothelium**—a monolayer of flat cells lining the arterial wall that separates it from the lumen. Very thin with a mean thickness of 4.6 μm.
- **Intima**—the innermost layer containing connective tissue and a few smooth muscle cells.
- **Internal Elastic Lamina (IEL)**—a very distinct, usually folded, membrane composed of elastic tissues with fenestral pores separating the intima from the media.

- **Media**—a thick layer, containing alternative layers of connective tissue (collagen fibers and elastic fibers) and smooth muscle cells.
- **External Elastic Lamina (EEL)**—a thin membrane that separates the media from the adventitia.
- **Adventitia**—the outermost covering of the vessel composed of loose connective tissue. Adventitia in most large arteries contains lymphatics and vasa-vasorum, a network of micro vessels that return the blood to the general circulation.

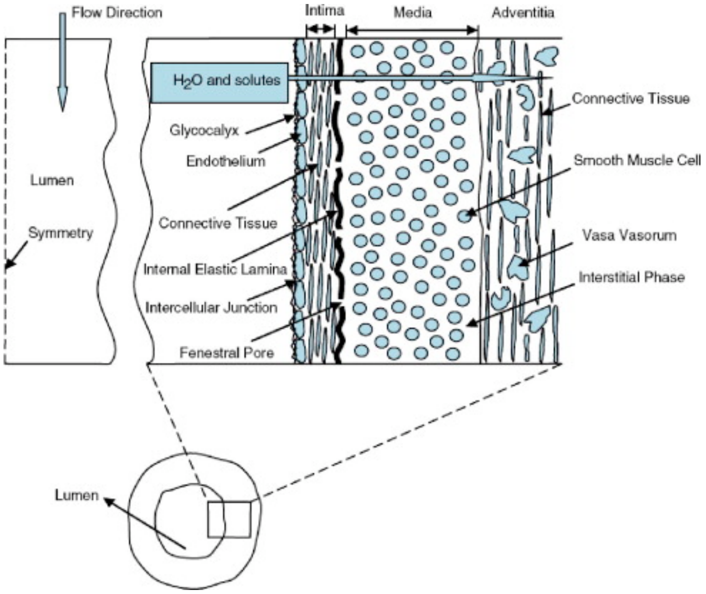

Figure 4.1: Healthy artery wall model. A typical artery wall composition, taken from [25]. This is a schematic of the longitudinal cross-section of artery wall geometry. Typical dimensions can be found in Table 4.1.

Transmural diffusion is driven by the steep concentration gradient across the artery wall created by the metabolic consumption of drug that takes place in the media. On the other hand, the lymphatics and vasa vasorum in the adventitia constantly drain solutes from the extra-cellular space. There is experimental evidence that the adventitia poses a substantially lower resistance to transport compared to the media, even without the clearance through the adventitial microcirculation [52]. Due to this fast diffusion of drug through the adventitia, it has been argued that there is no appreciable concentration gradient across the thickness of this layer. Therefore, the adventitia can be considered as a large sink for molecules that diffuse across the intima and the media through the extra-cellular space. This phenomenon can be mimicked by a sink type boundary condition (a constant concentration that can be higher than the average medial concentration) at the media-adventitia interface. These observations allow lumping of the adventitia and replacing it with a Robin type boundary condition at the media-adventitia interface as detailed in Section 2.2.3. Therefore in this work two homogeneous layers, the intima and the media separated by the IEL, were considered ignoring the endothelium and adventitia. Their contributions were incorporated through appropriate boundary conditions.

A medium to large sized healthy human coronary artery wall can be on an average 1 mm in thickness. Table 4.1 lists the dimensions of these two constituent layers of a typical Left Anterior Descending (LAD) coronary artery wall for both a healthy and a diseased artery as reported in [53]. The values in parentheses are the averages of all the thickness data taken from histomorphological studies referred to in [54]. Since the thickness of the intima and media vary widely with age, gender, disease condition and stage, etc., it is very difficult to select a representative idealized artery wall model. The selected dimensions for the two main homogeneous layers under consideration, intima and media, are provided in Table 4.1 (the last two rows in green) with their corresponding material properties presented in Section 4.2.

Table 4.1: Coronary artery wall dimensions in mm. [53, 54]

	Healthy	**Diseased**
Wall thickness with Adventitia	1±0.1	1.9±0.3
Adventitia	0.54±0.2	0.92±0.2
Wall thickness without Adventitia	0.46 to 0.5 (0.4 to 0.5)	0.98 to 1.0 (0.6 to 0.9)
Intima + Media	0.34±0.1	0.78±0.3
Intima thickness	<0.3 choose 0.15	0.65
Media	0.35	0.35

4.1.2 Diseased artery with a vulnerable plaque

The arterial remodeling associated with the disease process does not affect the media significantly, while the intima thickens appreciably because of lipid accumulation and the resulting smooth muscle cell proliferation (see Table 4.1). Figure 4.2 illustrates these morphological changes (see Sections 1.1 – 1.2 for a more detailed account) that lead to the formation of vulnerable plaques characterized by two distinct regions within the intima, a large lipid-rich necrotic core (> 40% of plaque area) and a fibrous cap (< 165 μm) that separates it from the lumen.

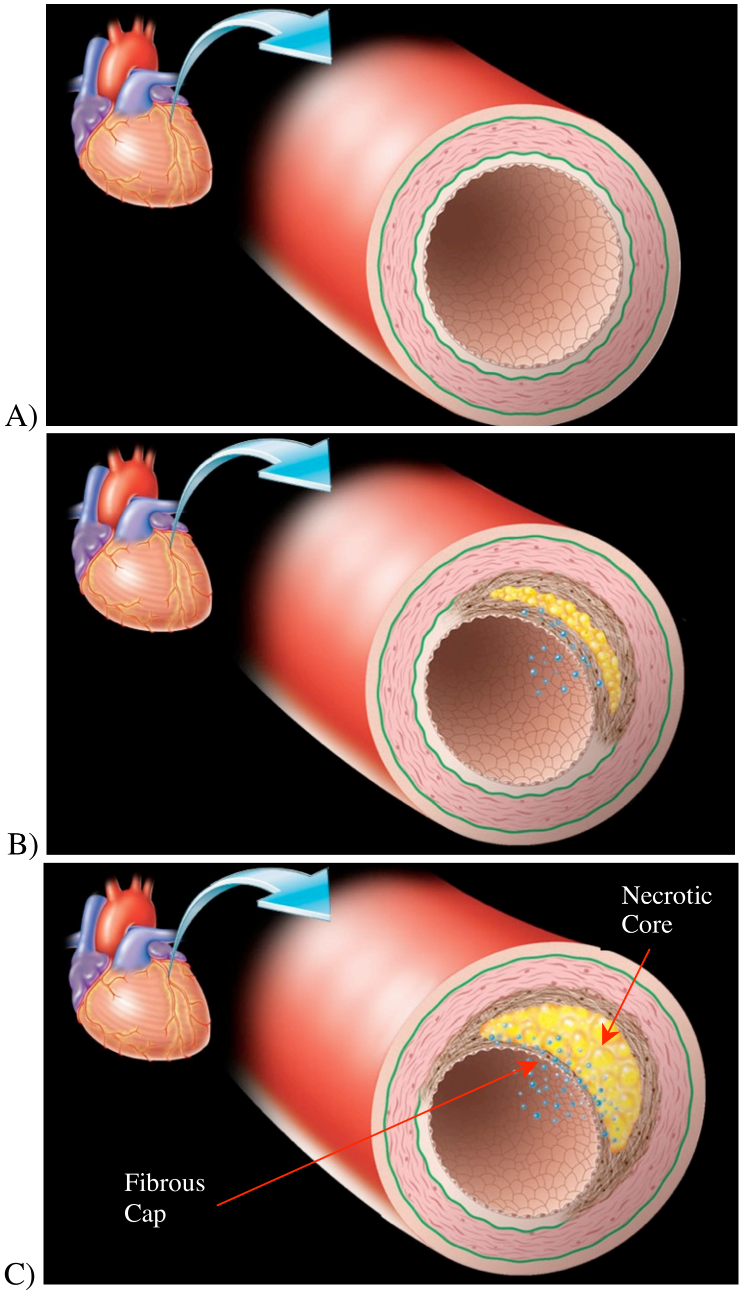

Figure 4.2: A schematic of the disease process in an artery wall. A) A cross section of a normal coronary artery, B) Intima thickening and lipid accumulation, C) Formation of a vulnerable plaque with a necrotic core encased by a fibrous cap.

4.2 PARAMETER SELECTION

The solution of the coupled transport model relies on a number of physical parameters; each of them may vary over a wide range, depending on physiological conditions. This makes modeling a bit of a challenge because there is a dearth of physiological data in the literature. In this section the parameters selected for both normal and diseased artery cases are presented. These parameters have been chosen in accordance with experimental evidence or some rationalization based on previous experiences that are consistent with typical drug transport scales. The major parameters used and the rationales behind their selection are discussed below.

4.2.1 Advective velocity

The interstitial space of arterial tissue can be thought of as a network of channels and pores. The fluid path is rather tortuous in the void space of this porous medium. As the structures of the pores are not known for arterial tissue, a continuum approach is used to describe the fluid flow in porous medium where the porous medium is assumed to be of uniform material as proposed by Darcy in 1856. According to Darcy's law the fluid velocity is proportional to the hydrostatic pressure gradient in a homogeneous and isotropic medium. A hydrostatic pressure difference of 60 to 100 mm Hg exists across the artery wall tissue resulting in advective transport from the lumen toward the adventitia. As an initial approximation, the three advective velocity components, V_r, V_θ and V_z are assumed to be spatially uniform and only the radial component is considered to be nonzero. That is,

$$V_r = V_0, \quad \text{and} \quad V_\theta = V_z = 0. \tag{90}$$

In the literature, where it is often referred to as filtration velocity, typical values of the radial velocity are of the order of 10^{-6} cm/s [22, 39, 42, 55]. Initial computations for the 1D case, and then the 3D axisymmetric case, were carried out with the advective velocity value obtained from the physiological Peclet number, Pe for the drug of interest. With a diffusivity 10^{-9} cm^2/s, a Peclet number of $Pe \approx 0.1$ (typically $Pe < 1$) was assumed to be representative of physiological conditions for the drug Everolimus (similar to Sirolimus and Rapamycin presented later in Section 4.2.3 as drugs of interest). This assumption was largely based on previous experience with experiments investigating transport behavior from drug eluting stents [56]. A summary of these parameters can be found in Table 4.1. However for the 3D multilayer artery wall models, both the idealized and patient-specific geometry, parameters were selected based on experimental data as described below.

According to Meyer et al. [22], filtration velocity has been experimentally measured to be 1.78e-6 cm/s for a transmural pressure jump of 70 mm Hg across the artery wall. This has been found to be consistent with the numbers reported by Tarbell et al. [57] and Huang et al. [58], as reported in [25]. Since larger molecules are reflected by the porous structure of tissue resulting in retarded advective flow, the filtration velocity is multiplied by a sieving coefficient, γ, to account for this phenomenon.

Table 4.2: Summary of some parameters

Parameter	Unit	Species I	Species II	Comment	Ref.
V_r^*	-	1	1	$V_r^* = \frac{V_r}{V_{r,0}}$; $V_r = V_{r,0} f_r(r,z,\theta,t)$	
V_θ^*	-	0	0	$V_\theta^* = \frac{V_\theta}{V_{r,0}}$; $V_\theta = V_{\theta,0} f_\theta(r,z,\theta,t)$	
V_z^*	-	0	0	$V_z^* = \frac{V_z}{V_{r,0}}$; $V_z = V_{z,0} f_z(r,z,\theta,t)$	
D_r^*	-	1/1000	1	$D_r^* = \frac{D_r}{D_{r,II}^0}$	
D_θ^*	-	1/1000	1	$D_\theta^* = \frac{D_\theta}{D_{r,II}^0}$	
D_z^*	-	1/1000	1	$D_z^* = \frac{D_z}{D_{r,II}^0}$	
$D_{r,II}^0$	cm^2/s	10e-9		Everolimus in calf carotid artery	[56]
σ	1/s	0	≈ 10e-5	0.006/hr for Everolimus	[56]
b	cm	0.1		Thickness of a typical porcine coronary artery 0.8 ± 0.2 mm.	[59]
$\bar{P}$	-	-	10	Everolimus in calf carotid artery	[56]
K_I'	1/s	(0.0033)	-	For the NPs	[56]
K_I''	1/s	(1.65e-6)			[56]
k_m	cm/s	(10e-5)[1]	2.44e-7	LDL: 2.2e-6; Paclitaxel: 2.44e-7	[38, 56, 60]
Factor	-	1		1-2 fluid-solid interface	
h	cm	0.001			

---

[1] Items within parentheses are assumed properties based on typical drug transport time scales.

As a starting point, the advective velocity is assumed to be the same across the artery wall for both the nanoparticles (NP) and the drug. From Table 4.2, the advective velocity of LDL in intima was calculated to be, $V_r = u_{filt} \times \gamma$ = 1.78e-6 x 0.0171 ≈ 3e-7 cm/s. Similarly, Edelman et al. [61] have reported V_r for the drug Paclitaxel in bovine carotid arteries to be 3.2e-7 cm/s with a transmural pressure difference of 60 mm Hg. Based on these observations, V_r = 3e-7 cm/s appears to be a reasonable approximation for the radial component of advective velocity.

4.2.2 Metabolic reaction rate

The importance of the reaction term depends on the drug used, tissue characteristics, and other physiological factors. The reactive term acts as a sink for drug concentration. A typical value for the consumption rate for LDL is 10^{-4} 1/s [25]. For Everolimus, in-house data [56] indicate a rate of 0.006/hr ≈ 10^{-5} 1/s. For the nanoparticles, this parameter is set to zero as these nanoparticles are not assumed to be biodegradable in the calculations.

4.2.3 Effective diffusivity and permeability

4.2.3.1 Healthy artery

Nanoparticles

Drug-encapsulated polymeric nanoparticles are typically 50 – 200 nm hydrophobic spherical particles. The transport properties of these NPs are comparable with those of macromolecules like LDL (MW ≈ 2500 kDa), which are 25 – 50 nm and likewise hydrophobic/lipophilic (with affinity to lipid) in nature. Vafai et al. [25] reported the following parameters for macromolecular transport in artery walls based on the work of Karner et al. [24], Stangeby and Ethier [30], and references therein.

Table 4.3: Nanoparticle transport properties for different artery wall layers based on [25]

Properties	**Endothelium**	**Intima**	**IEL**	**Media**	**Ref.**
Diffusivity, D (cm^2/s)	8.145e-13	5e-8	3.18e-11	5e-10	[25]
Porosity, ε	0.0005	0.96	0.004	0.15	[27, 30, 38, 58, 62]
Effective diffusivity, D_{eff} (cm^2/s)	4.08e-16	4.8e-8	1.27e-13	7.5e-11	
Permeability, P (cm/s)			1.59e-7		[24]
Sieving Coefficient, γ	0.0145	0.171	0.171	0.134	[25]
Filtration velocity, u_{filt} (cm/s)	1.78e-6				[22]

In Table 4.3, the effective diffusivity for each homogeneous wall layer was computed by multiplying free diffusivity with porosity accounting for hindered diffusion through the arterial structure. The effective diffusivity for the nanoparticles was assumed to be isotropic due to lack of data in the literature with evidence to the contrary (unlike hydrophobic drugs which show clear evidence of anisotropic diffusion). Furthermore, assuming that both LDLs and NPs are large molecules compared to the solvent water, according to the Stokes-Einstein theorem, the diffusivity should be inversely proportional to the radius of the solute. Therefore, the effective diffusivity for LDL (in green) has been scaled by a factor of 5 since typical LDL size is 25 – 50 nm whereas NP size is usually somewhere between 50 to 200 nm. The parameters used in the simulations are listed in Table 4.4.

Table 4.4: Nanoparticle transport properties used for different artery wall layers

Properties	Intima	IEL	Media
Effective diffusivity, D_{eff} (cm^2/s)	9.6e-9		1.5e-11
Permeability, P (cm/s)		3.14e-8	

Drug

Low molecular weight (MW) hydrophobic drugs have shown appreciable therapeutic effect in local drug delivery systems [63]. For this work, immunosuppressant drugs Rapamycin or Sirolimus (0.954 kDa) and Paclitaxel (0.854 kDa) were selected as representative drugs for the luminal drug delivery system of interest. These are hydrophobic or lipophillic drugs commercially used in drug eluting stents. These drugs have been studied extensively by Edelman and co-workers [23, 60, 61, 64, 65] for their arterial transport properties. Table 4.4 lists effective diffusivities and permeabilities for different hydrophobic species found in the literature along with their corresponding sources.

Table 4.5: Transport properties of different hydrophobic compounds

	Intima		**IEL**		**Media**		**Ref.**
Species \ Properties	D_z, D_θ	D_r	D_{IEL}	P_{IEL}	D_z, D_θ	D_r	
Rapamycin (0.954 kDa)	6e-5	8e-8		(1e-7)	6e-7	8e-10	[65]
Paclitaxel (0.854 kDa)	7e-5	2e-8		(1e-7)	7e-7	2e-10	[65]
HRP (44 kDa)			2.4e-11	2.4e-7			[66]
Albumin (66 kDa)			2.4e-10	2.4e-6[2]		1.3e-8	[67]

---

[2] Based on IEL thickness of 1 micrometer. Numbers withinin parentheses are estimated values. Numbers in green correspond to the References.

There is a three order of magnitude difference between the effective diffusivities in planar (θ and z), and radial (r) directions in the media. On the other hand, the diffusivities in the intima are in general approximated to be one hundred times faster than that in the media according to Huang et al. [26]. This observation is in essence supported by Hwang et al. in [64], where it has been argued that neo-intimal diffusivity and planar medial diffusivity should be of the same order because of absence of elastin fiber barriers in the region. Hence the diffusivities in the intima were approximated to be two orders of magnitude higher than that in the media, as presented in Table 4.5.

Tarbell et al. [38] observed that for low Peclet number flows, IEL pore structure, and consequently IEL permeability, had a significant influence on tissue uptake and medial concentration for a low molecular weight solute like Adenosine Tri-Phosphate or ATP (0.507 kDa). On the other hand, for a high-molecular-weight (MW) solute LDL with a convection-dominated flow through the interstitial space, the medial tissue uptake was not affected by IEL pore structure. Extrapolating these results to the drugs of interest (MW approximately 0.8-0.9 kDa), Rapamycin and Paclitaxel are expected to be transported by a diffusion-dominated mechanism ($Pe < 1$) and, influenced greatly by the IEL pore structure.

Penn et al. [66] reported IEL permeability in rat aorta for a tracer enzyme Horseradish Peroxide, HRP (≈ 44 kDa) to be 2.4e-7 cm/s, whereas, Fry et al. [68] found IEL permeability in dog aorta for albumin (≈ 66 kDa) to be one order of magnitude greater than that, that is ≈ 2.4e-6 cm/s (assuming IEL thickness of 1 micrometer). But this could be due to facilitated transport of protein. Considering the fact that Sirolimus and Paclitaxel have lower MW than HRP and may not show protein (say albumin) facilitated transport to the same degree, it is reasonable to expect the drug IEL permeability to be somewhere in between that for HRP and albumin. Hence it was approximated to be ≈ 1e-7 cm/s.

4.2.3.2 Diseased artery

Although there exists animal models with lipid-rich or neointimal (due to restenosis) lesions, drug transport properties through these lesions are not available in the literature due to their wide range of variability. However, researchers have shed some light on the possible behavior of these drugs under diseased conditions based on their observations regarding the general transport properties in healthy arteries. For example, drug diffusion in hyperplastic neointimal layer should be isotropic because there is little variation in smooth muscle cell orientation in this region. Similarly, this observation can be extended to the vulnerable (lipid-laden) plaque and isotropic diffusion can be attributed to both the fibrous cap and the lipid core. Furthermore, while hydrophobic drugs and nanoparticles will have a higher affinity to the lipid core, both the IEL and the atherosclerotic plaque act as barriers to macromolecular (i.e., NP) transport. So is the case with drug transport but to a lesser degree [64]. On the other hand Lee et al. [69] concluded that the IEL does not pose a significant barrier between the intima and the media in the atherosclerotic process, indicating that IEL permeability for drugs may be higher in diseased arteries compared to healthy ones. There seems to be a lack of consistent data in the literature quantifying the variability in transport properties induced by the disease process. Therefore, the diseased artery was simulated largely by incorporating geometric and structural modifications (along with their corresponding material properties) caused by the progression of atherosclerosis, for example, lipid accumulation, intima thickening and fibrous cap formation, while keeping the transport properties for the unaltered layers (i.e., the healthy part of the intima and the media) the same as in the healthy case. This is a major assumption that needs to be further investigated through a sensitivity analysis.

The fibrous cap is made of collagen fibers and smooth muscle cells. With increasing collagen content, the diffusivity through the extra cellular matrix decreases [70]. Hydrophobic drug Retinoic acid (≈ 0.3 kDa) has a permeability of 120e-4 cm/hr with a partition coefficient of 18 in collagen film. With collagen film viscosity of about 100 cp, Retinoic acid diffusivity is reported to be 3.25e-4 cm/hr [71]. But intuitively, for a larger molecule like LDL, effective diffusivity can be expected to be lower than Retionic acid. Hence, using the Stokes-Einstein equation,

$$\frac{D_{LDL}}{D_{Retinoic}} \approx \left(\frac{M_{w\_LDL}}{M_{w\_Retinoic}} \right)^{-1/3} \tag{91}$$

the effective diffusivity for the NPs can be roughly estimated to be D_{fc} = 4.5e-9 cm^2/s. The effective drug diffusivity in the fibrous cap was derived applying the same rationale (see Table 4.6).

In the diseased case, the extra-cellular space of the necrotic core is rich in lipid content. Properties of lipid/oil, such as olive oil, can be used to represent the transport behavior of this drug through the lipid core [72]. The viscosity of olive oil is about 85 times that of water. The Stokes-Einstein relation predicts the diffusion coefficient for LDL to be 85 times less in oil. Therefore, assuming structural hindrance (porosity) characteristics are similar to the intima, the diffusivity of the nanoparticles in lipid core is determined by scaling D_{intima} by a factor of 85 to get D_{lipid} = 1.13e-10 cm^2/s. On the drug side, due to its high affinity to lipid, hindrance due to binding and unbinding (often referred to as reversible binding) of the drug to lipid or protein sites need to be accounted for. As a crude approximation, the effective diffusivity of Paclitaxel in olive oil was computed from its diffusivity in blood [73] and then scaled by octanol-water partition coefficient for the drug ($\approx 10^{4.5}$) [56], as proposed by Taylor et al. [40], to get the effective drug diffusivity in the lipid core. Table 4.6 lists the transport properties used for the diseased parts of the artery wall.

Table 4.6: Transport properties of nanoparticles and the drug in the diseased parts of the artery wall [3]

Species	Properties	Fibrous cap	Lipid core
NP	Effective diffusivity, D_{eff} (cm^2/s)	4.5e-9	1.13e-10
Drug	Effective diffusivity, D_{eff} (cm^2/s)	6.23e-8	1.45e-13

4.2.4 Boundary conditions

Using the parameters presented in Table 4.1 that appear in the lumen-side boundary condition equations introduced in Section 2.2.3, the resulting time

---

[3] Properties for the diseased portion only. For the intima, IEL and the media see Tables 5.2 and 5.3

varying concentration for the nanoparticles and the free drug that may be present in the formulation are as shown in Figure 4.3 and Figure 4.4, respectively. The nanoparticles partition into the artery wall and reach a maximum concentration within a few minutes of administration, after which, they slowly deplete to zero in approximately 21 days. This is a consequence of competition between the rate of forward reaction ("sticking") and backward reaction ("un-sticking") of nanoparticles. The forward and backward reaction rates or sticking coefficients are design parameters for the nanoparticles that are often manufactured to have special surface characteristics to enhance sticking. Based on experiences in the medical device industry, a forward reaction rate, K_I' = 1/10 per minute with a time constant of 10 minutes, and backward reaction rate, K_I'' = 1/10080 per minute with a time constant of 7 days were chosen.

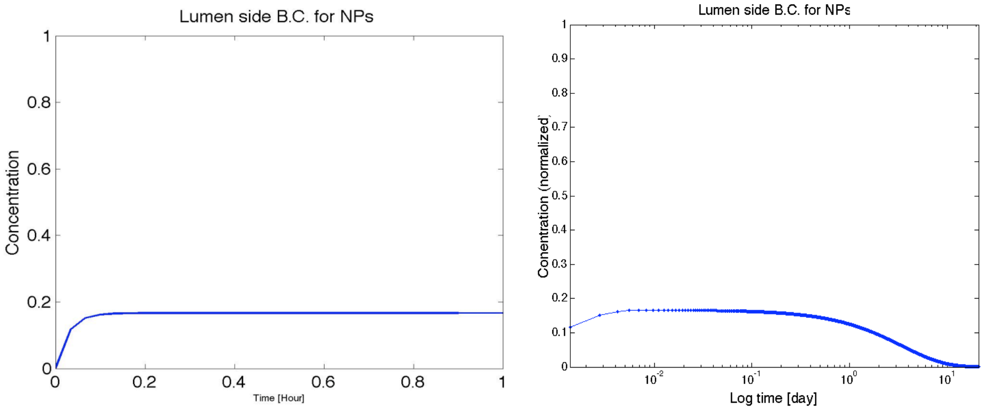

(a) (b)

Figure 4.3: Lumen-side boundary condition for the nanoparticles: (a) when $K_I' >> K_I''$, (b) when K_I'' is not negligible.

In the 1D (Section 5.1) and 3D axisymmetric (Section 5.2) calculations it was assumed that $K_I' >> K_I''$, which implies that once the nanoparticles partition into the tissue at the lumen-side boundary, they remain attached for the time period under consideration, that is 7 days of simulation time (see Figure 4.3a). The rest of the 3D simulations were performed with a more realistic assumption that K_I'' is not negligible (see Figure 4.3b).

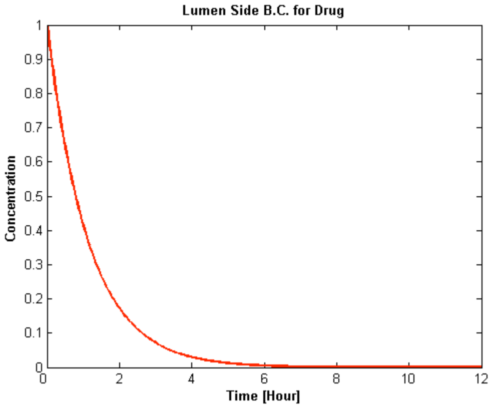

Figure 4.4: Lumen-side boundary condition for the free drug present in the formulation.

The formulation released into the bloodstream by design may contain free drug in addition to the drug encapsulated within the nanoparticles. Typically anywhere from 40 to 200 mg of free drug is added to the solution for every 200 mg of drug that is encapsulated in the nanoparticles. This is one of the design parameters that can be tweaked for better efficacy. In this work, a formulation of 220 mg of free drug for 200 mg of encapsulated drug was used to determine if there is a noticeable effect of the presence of free drug on drug distribution. Figure 4.4 depicts the exponential loss of the free drug to blood flow at the lumen-side boundary where it takes about 6 hours for the drug to be completely washed away.

An investigation of the effect of adventitia-side boundary condition on drug distribution revealed that there is little or no difference in the time-varying concentration profiles within the artery wall between zero-flux and zero-sink type boundary condition, especially in regions away from this boundary. A similar observation was made by Yang and Vafai in [39] where it was demonstrated that LDL concentration in intima, IEL and media are independent of the boundary condition at this media-adventitia interface. A zero concentration sink boundary condition was employed at the adventitia-side for both species, as it appeared to be the natural choice for reasons explained previously in Section 4.1.2.

4.2.5 Drug release rate

Typically, by design, the nanoparticles release 30% of the entire drug encapsulated by the end of day 1, and a 70% release is achieved by the end of first week [56]. Manipulating the design parameters D_1, D_2 and f_1 in the bi-phasic drug

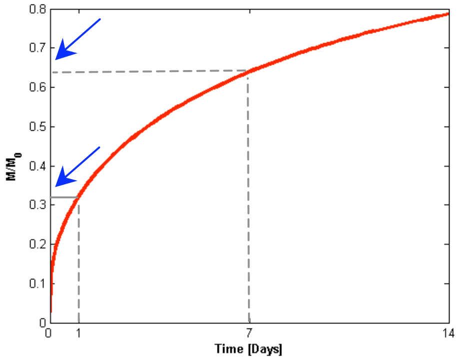

Figure 4.5: Tailored bi-phasic (monodisperse case) drug release rate profile used in the simulations achieving a 30% drug-release by day 1, and a 65% release by day 7.

release model presented previously in Section 2.2.2, the resulting drug release rate profile used in the simulations is presented in Figure 4.5.

4.3 SOLUTION APPROACH

Isogeometric analysis employing quadratic NURBS was used for spatial discretization. As a first approximation, the arterial wall was assumed rigid in computations for simplicity, as the primary focus was placed on the transport-reaction formulation. A residual-based multiscale method was used to solve the coupled transport equations while generalized–α method was adopted for time advancing. The numerical code was first verified against a simple 1D pure diffusion problem with known analytical solution (see Appendix A). Then simulations were run for 7 days with a time step of 2 minutes on several 3D NURBS-based geometries of interest.

The YZβ discontinuity capturing method [74] was employed to address potential stabilization issues related to the jump condition across the IEL.

CHAPTER 5

Application to Idealized Artery Geometry

A cubic geometry of unit dimensions was generated to verify the in-house numerical code developed against a 1D diffusion problem with known analytical solution (see Appendix A) and to study the effect of dominant dimensionless numbers on drug distribution (see Section 6.1). This model was further utilized in the selection of an optimal discretization for a set of physiological parameters (see Table 4.2). Since nanoparticles (NPs) have a very low diffusive coefficient, often of the order of 10^{-12} cm^2/s, they tend to stay close to the lumen side boundary over a considerable duration of time. To capture nanoparticle transport in this so-called boundary layer, the mesh was refined near the boundary as shown in the Figure 5.1. This 1D mesh was then mapped onto the 3D idealized cylindrical geometry with the dimensions shown Figure 5.1b in accordance with typical values found in the literature (see Table 4.1).

5.1 IDENTIFICATION OF DOMINANT PARAMETERS

A study of the effect of dimensionless numbers, namely Peclet number and Damkohler number, on drug distribution was carried out in order to gain insight into the parameter sensitivity of drug distribution. The equations for the coupled transport model as detailed in Sections 2.1 − 2.3 were solved using the solution approaches presented in Section 4.2. The computations were performed on the 1D geometry (see Figure 5.1a) over a range of values:

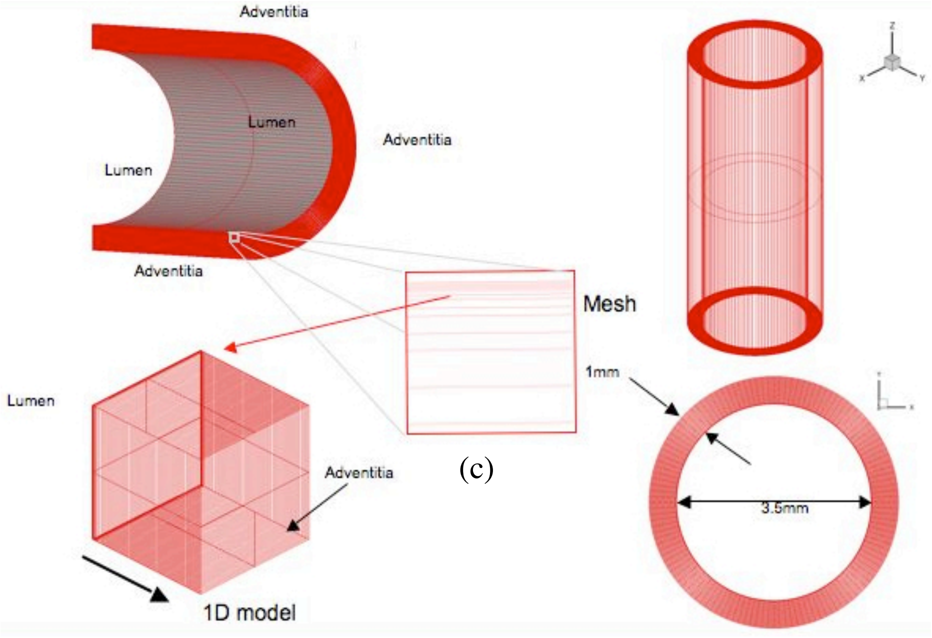

(a) (b)

Figure 5.1: NURBS meshes used: (a) Cubic mesh for 1D analysis (b) 3D cylindrical single-patch NURBS mesh for the idealized healthy coronary artery wall segment model.

Pe = [0.01 to 1] while keeping Da constant, and

Da = [1.7 to 1700] while keeping Pe constant,

Here the species subscripts were omitted for simplicity.

Table 5.2 shows the time evolution of drug concentration over the thickness of the artery wall for four different cases. In all four cases, drug concentration increases sharply with distance to a peak value before decreasing (at a slower rate) asymptotically to zero for all times. With time this peak penetrates deeper into the artery wall. This indicates that the peak concentration follows the transport of the nanoparticles (NPs), because at a given time, the depth of penetration of the peaks is the same for all Pe or Da.

Drug transport is a diffusion dominated process, hence, the purely diffusive case, $Pe = Da = 0$ (see Table 5.2a) was considered first. The response of the system with varying Pe and Da was studied with respect to this reference case.

5.1.1 Effect of Peclet number on drug distribution

The Peclet number compares the diffusion term in the direction of the motion to the advective component. To investigate the influence of advective velocity on drug distribution compared to diffusion, simulations were carried out for three different values of Peclet number within physiological ranges. A comparison of Table 5.2(a) and (b) shows that although the concentration profiles maintain the same shape in general, the peaks are now sharper with increasing Pe. A decreasing Pe essentially brings about a sharp drop in the peak concentration value at all times.

Figure 5.3 demonstrates a strong influence of advective velocity on drug distribution. A higher concentration and a deeper penetration of drug can be observed due to advective forces acting on the nanoparticles, as well as the drug released from them. This can be expected since the advective velocity acting radially carries the nanoparticles, and hence the released drug away from the wall. At later times a more uniform distribution is observed. There is a possibility of the solution becoming unrealistic beyond a critical Pe, a hint of which can be seen in the case $Pe \approx 1$.

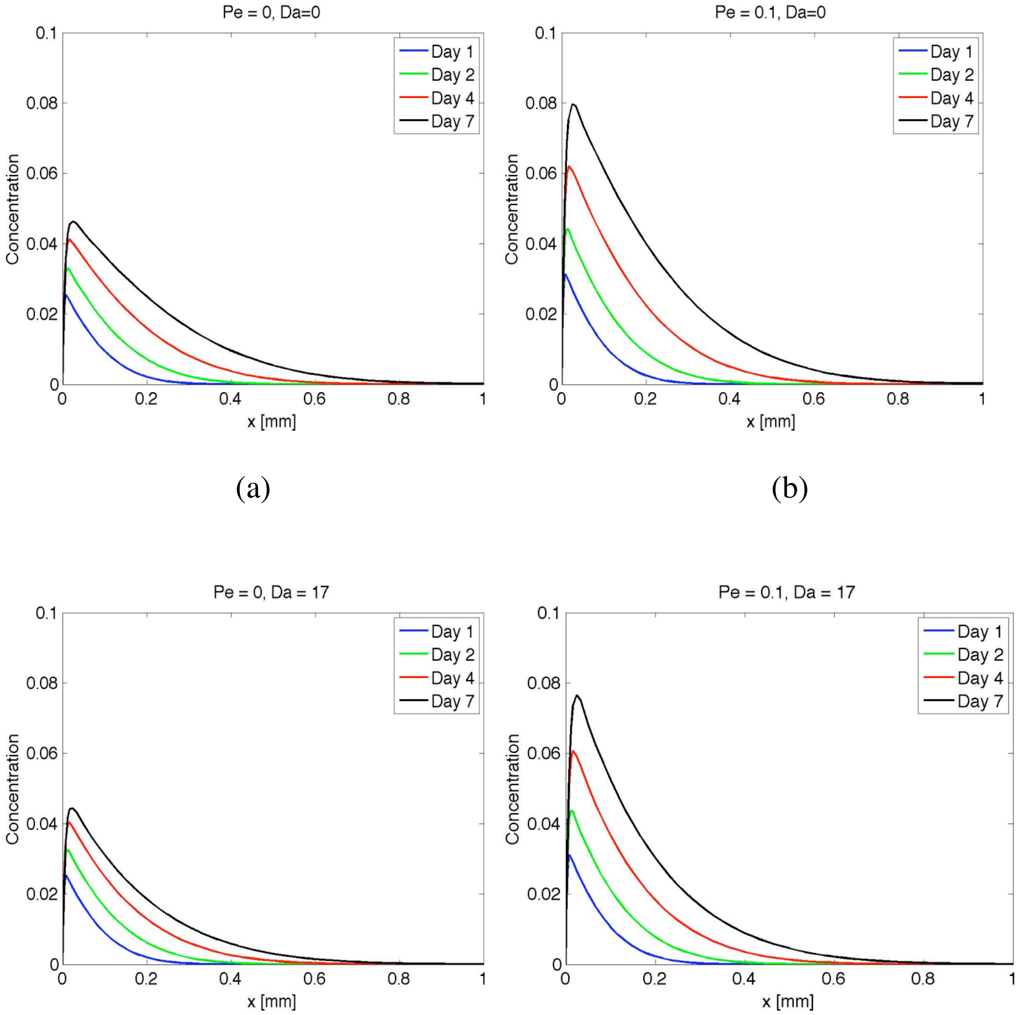

(a) (b)

(c) (d)

Figure 5.2: Drug concentration in the arterial wall at various times during simulation for the cases: (a) $Pe = 0$, $Da = 0$; (b) $Pe = 0.1$, $Da = 0$; (c) $Pe = 0$, $Da = 17$; (d) $Pe = 0.1$, $Da = 17$.

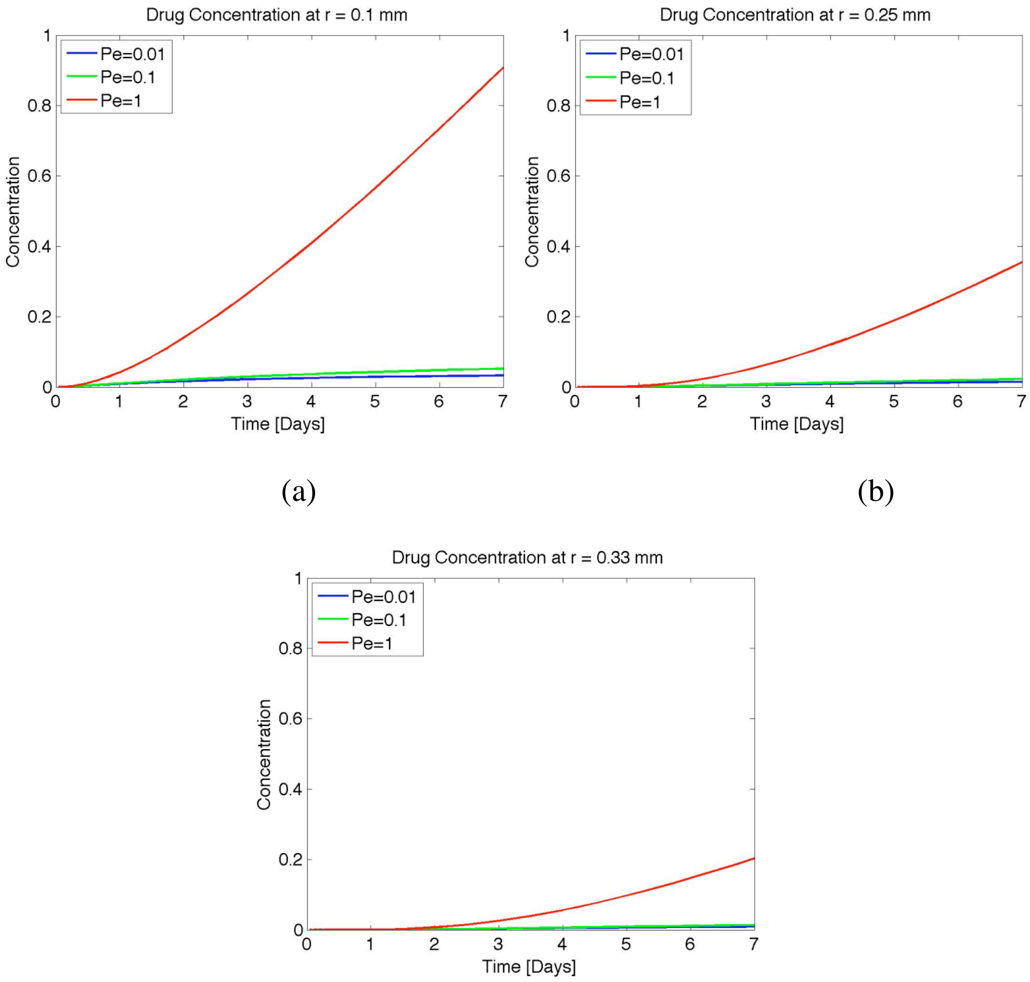

(a) (b)

(c)

Figure 5.3: Influence of Peclet number on drug distribution. Concentration of drug at different cross-sections of the artery: (a) r = 0.1 mm or 1/10 depth, (b) r = 0.25 mm or 1/4 depth, and (c) r = 0.33 mm or 1/3 depth of the artery thickness.

5.1.2 Effect of Damkohler number on drug distribution

Damkohler number can be defined as the ratio of diffusive time scale and metabolic reaction time scale. It quantifies the relative importance of chemistry with respect to fluid dynamics. In other words, Damkohler number represents the time for a chemical reaction to occur relative to the time it takes a particle to diffuse through the control volume.

Figure 5.4 depicts drug distribution at four increasing values of Da. A higher Da expedites the drug consumption and reduces concentration while preserving the concentration profile shapes at fixed times. Variation of concentration with Da though negligible at initial times, becomes significant at later instants. The concentration profiles seem to flatten and then decrease linearly with time. As the Da is increased in steps of one order of magnitude, from 2 to 20, the concentration does not diminish as drastically as it does beyond that point, i.e., from $Da \approx 20$ to 200, or 200 to 2000.

A comparison of Figure 5.2(a) and Figure 5.2(c) reveals comparable drug distribution with concentration values remain within 1%. Though the peak value and the shape of the concentration profiles are preserved for all times, drug penetration suffers noticeably with increasing Da. This trend is repeated when Figure 5.2(b) and Figure 5.2(d) are compared as well.

To summarize, both the Peclet number and the Damkohler number are dominant in the transport process. Effect of varying Pe is similar to that of Da, though more sensitive in the latter case.

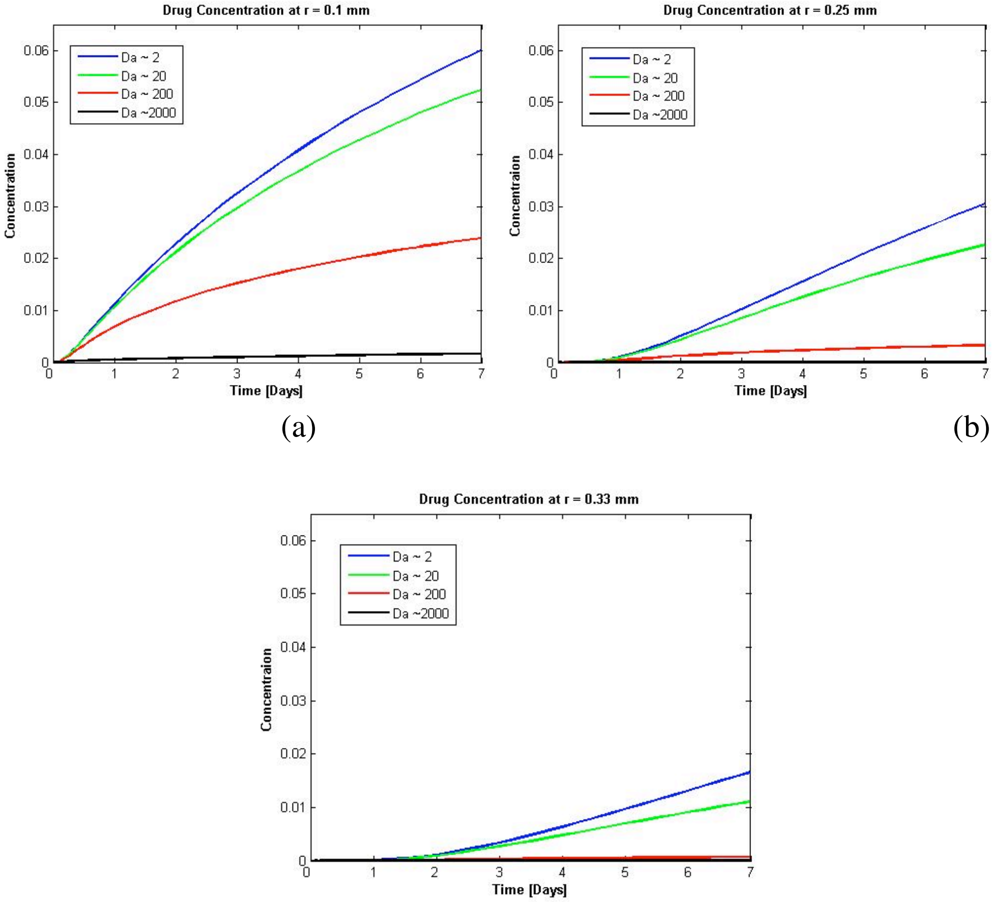
Drug Concentration at r = 0.1 mm

Drug Concentration at r = 0.25 mm

Drug Concentration at r = 0.33 mm

(a) (b)

(c)

Figure 5.4: Influence of Damkohler number on drug distribution. Concentration of drug at different cross-sections of the artery: (a) r = 0.1 mm or 1/10 depth, (b) r = 0.25 mm or 1/4 depth, and (c) r = 0.33 mm or 1/3 depth of the artery thickness.

5.1.3 Effect of boundary conditions on drug distribution

An investigation of the effect of adventitia-side boundary condition on drug distribution demonstrated that there is little or no difference in the time-varying concentration profiles between zero-flux and zero-sink type boundary condition. The shape of the concentration profiles (see Figure 5.5) remains essentially the same for all times. However, there is a slight change in concentration near the adventitia-side boundary for the non-zero sink type boundary condition case. Here the constant concentration at the boundary forces a slight rise in concentration values near the adventitia. Even then, the presence of drug in the adventitia side does not affect drug distribution near the in the intima or the media and the concentration profiles remain the same in both size and shape, up to 60% depth into the artery wall. These observations are in agreement with the findings in [25]

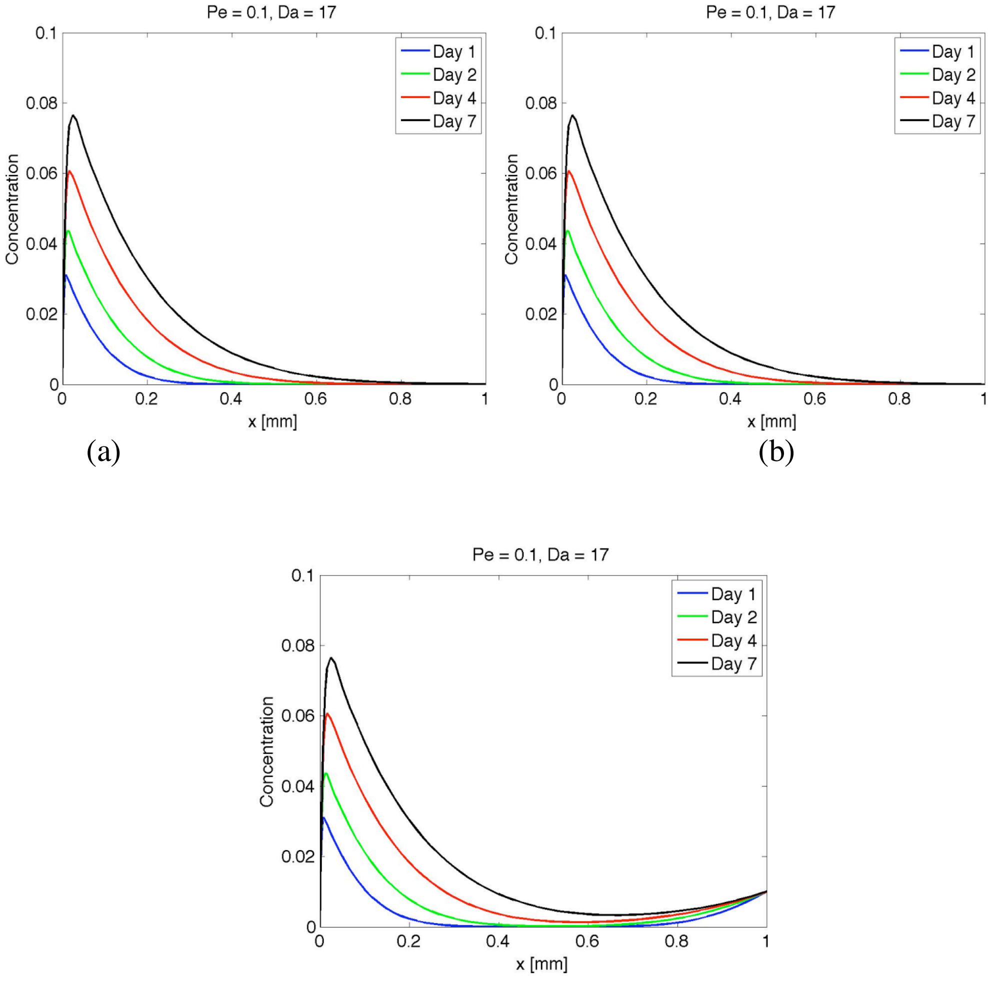

(a)

(b)

(c)

Figure 5.5: Influence of adventitia-side boundary condition (B.C.) on drug distribution. Concentration of drug in the arterial wall at various times for: (a) zero flux B.C., (b) zero sink B.C., and (c) nonzero sink B.C. where normalized concentration at the boundary is 0.01.

5.2 DRUG DISTRIBUTION IN A 3D HOMOGENEOUS ARTERY WALL MODEL

In a healthy artery wall, the media makes up almost 2/3 of the inner artery wall (intima-media) thickness. Therefore, for simplicity it was assumed that a single layer homogeneous wall model with just the media was sufficient to capture the overall artery wall transport characteristics. Initial calculations were performed on this geometry to produce axisymmetric results and to compare these results with those of the multi-layer realistic artery wall model in order to gain an appreciation for the effect of wall inhomogeneity on drug distribution.

Using the parameters in Table 4.1, and applying the same numerical procedures in Section 3.1-3.3 and solution approach described in Section 4.3 (as in the 1D case) simulations were carried out for the idealized cylindrical homogeneous coronary artery wall model (see Figure 5.1) for two specific cases:

Case 1: No free drug in the formulation

Simulations were run for 7 days assuming the formulation released into the bloodstream did not contain free drug, that is, the entire drug was encapsulated within the nanoparticles. This implies that the drug concentration for the lumen side boundary was set to zero for all times. Results are presented in Figure 5.6 where the distribution of the nanoparticles and the drug are displayed side-by-side at various times. Since transport in the artery wall is a diffusion dominated process, the very low nanoparticle diffusivity makes the nanoparticle penetration barely noticeable in these pictures even after 7 days. A close-up view is provided in Figure 5.7, which shows evidence of very slow penetration of the artery wall, by the nanoparticles. On the other hand, the drug penetrates approximately 1/8 of the thickness of the artery in 24 hours, while it takes about 7 days for the drug to reach about 1/3 of the thickness of the artery (qualitatively).

Case 2: With free drug in the formulation

Same simulations were carried out for 7 days assuming the formulation released into the bloodstream contained free drug in addition to the encapsulated drug within the nanoparticles. Figure 4.4 depicts the time varying lumen-side boundary condition for the drug used for this case.

Results are presented in Figure 5.8, which shows the spatial distribution of the drug at various times. Drug distribution data for the first few hours confirms the decaying of free drug concentration at the lumen-side boundary due to their loss to blood flow in the lumen. By the end of day 1 the entire free drug is washed away from the lumen-side boundary and drug concentration reaches a minimum. From that point onward, drug concentration picks up gradually with time (see concentration for day 4 and then day 7), and penetration depth increases as the slowly moving nanoparticles act as a source of drug, much like in Case 1. Over a period of 7 days, the depth of penetration by the drug is approximately the same with no significant difference in concentration compared to Case 1. This demonstrates the effect of free drug in the formulation, which can provide an initial burst of high drug concentration near the wall, after which it is up to the slow and controlled release of the drug from the nanoparticles to provide the necessary therapeutic effect.

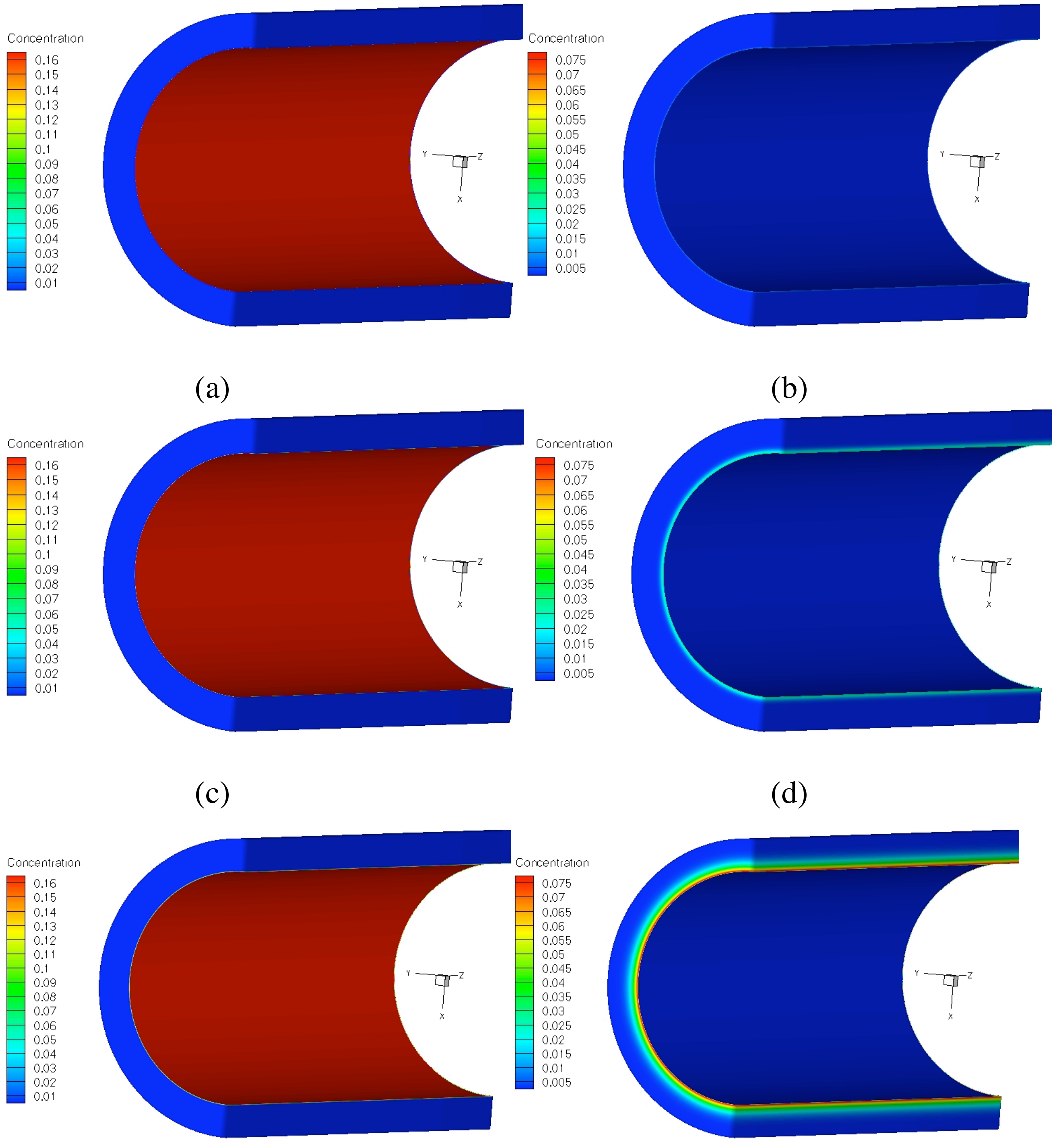

(a) (b)

(c) (d)

(e) (f)

Table 5.6: Temporal and spatial distribution of drug-encapsulated nanoparticles and the drug with no free drug in the formulation (Case 1). Nanoparticle concentration in the arterial wall at: (a) t = 1 hr, (c) t = 1 day, (e) t = 7 days. Corresponding drug concentration at: (b) t = 1 hr, (d) t = 1 day, and (f) t = 7 days.

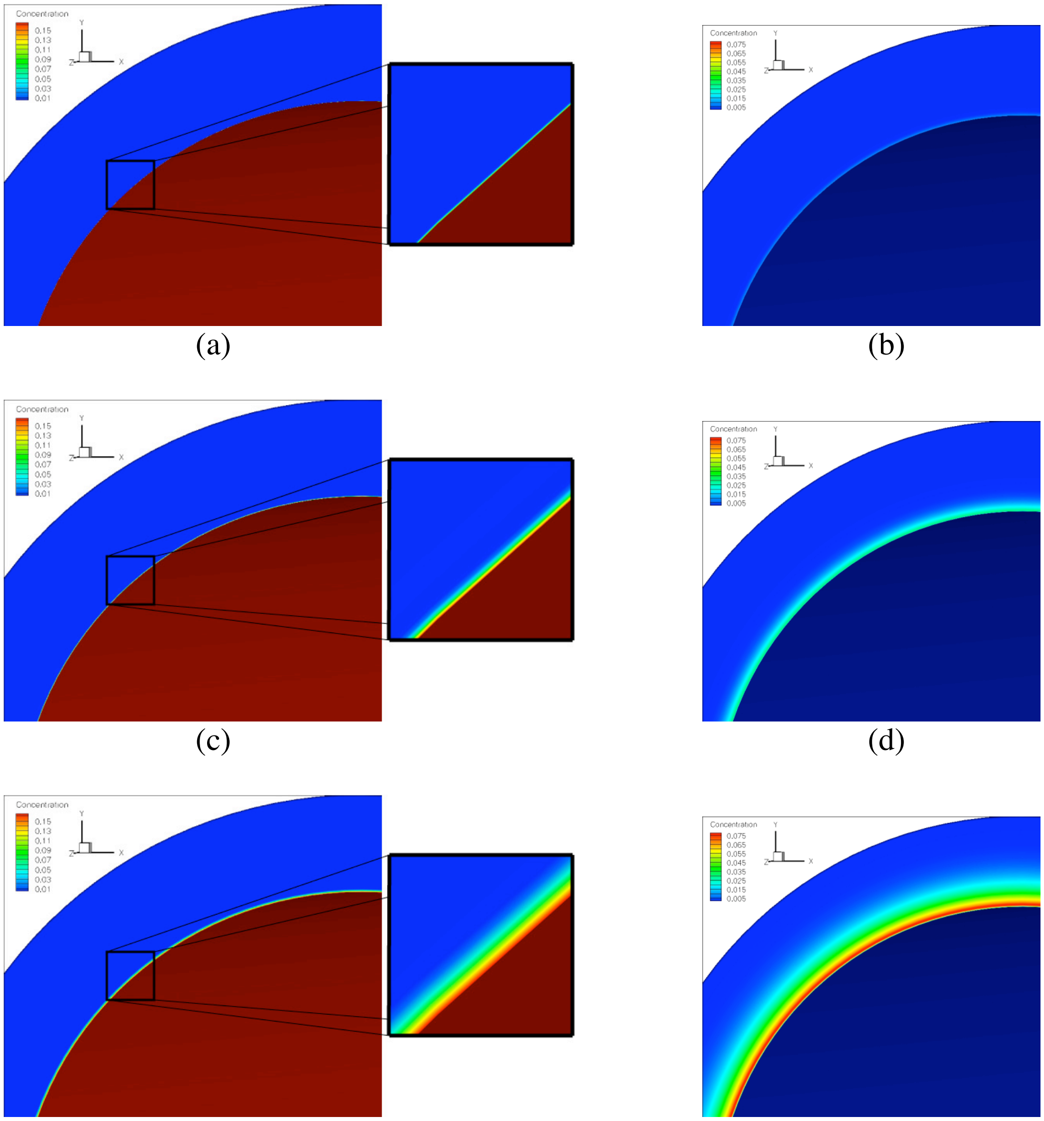

(a) (b)

(c) (d)

(e) (f)

Table 5.7: A close-up view of the temporal and spatial distribution of drug-encapsulated nanoparticles and the drug with no free drug in the formulation (Case 1). Nanoparticle concentration in the arterial wall at various instants during simulation: (a) t = 1 hr, (c) t = 1 day, (e) t = 7 days. Corresponding drug concentration at various instants during simulation: (b) t = 1 hr, (d) t = 1 day, and (f) t = 7 days.

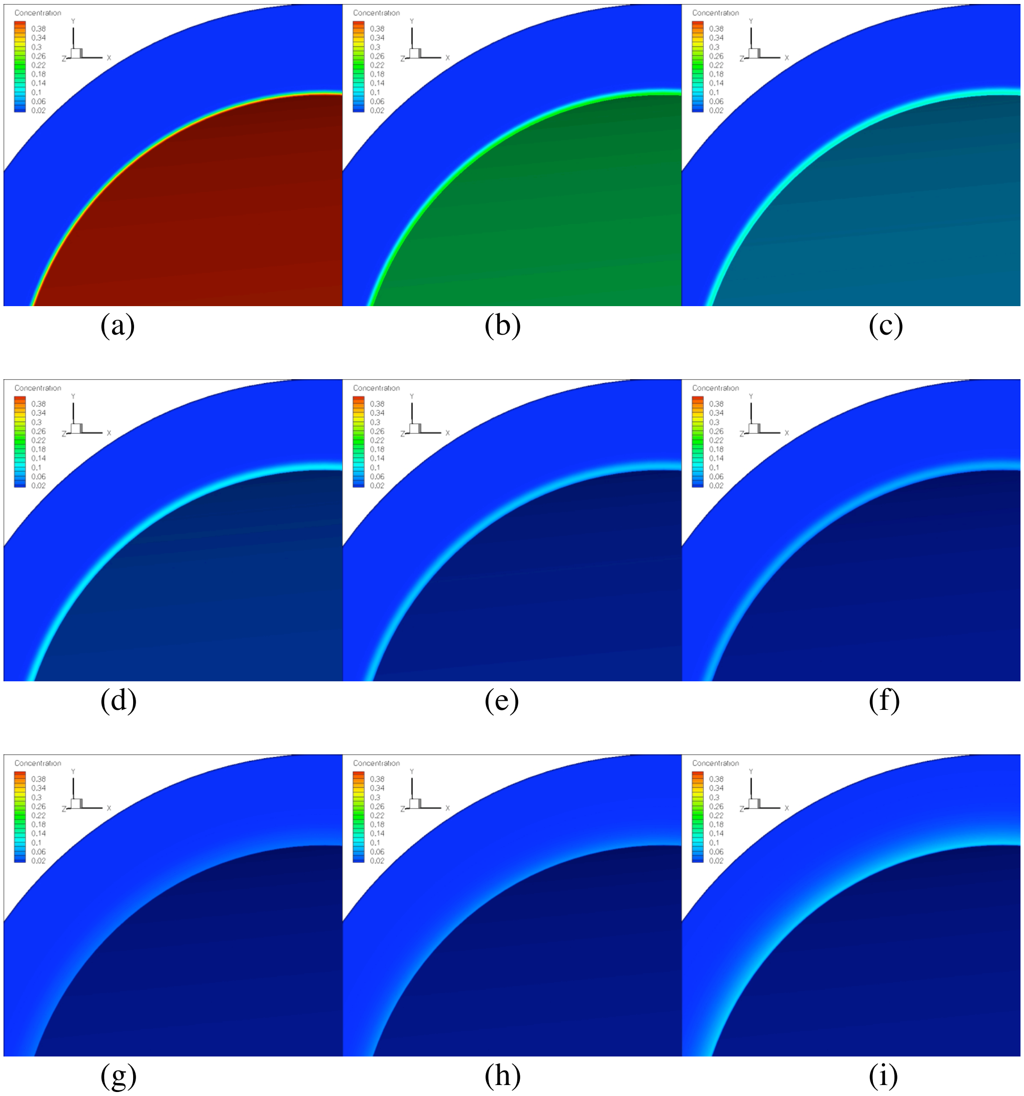

Table 5.8: Temporal and spatial distribution of drug with free drug in the formulation (Case 2). Drug concentration in the arterial wall at various instants during simulation: (a) $t = 1$ hr, (b) $t = 2$ hrs, (c) $t = 3$ hrs, (d) $t = 4$ hrs, (e) $t = 5$ hrs, (f) $t = 6$ hrs, (g) $t = 1$ day, (h) $t = 4$ days, and (i) $t = 7$ days.

5.3 DRUG DISTRIBUTION IN A 3D MULTILAYER ARTERY WALL MODEL

As presented previously in Section 4.1, the coronary artery wall model under consideration is comprised of mainly two concentric layers, 1) the intima, 2) the media, with IEL separating the two homogeneous parts. Starting out with an idealized normal artery wall model, a straight cylindrical tube with wall composition divided into its constituent layers of anatomically relevant dimensions with appropriate material properties assigned, a vulnerable plaque characterized by a fibrous cap and a lipid pool underneath was incorporated in the coronary artery segment to study the effect of plaque heterogeneity on drug distribution under diseased conditions.

5.3.1 Drug distribution in a normal artery wall

In this section, the application of the computational tool-set to an idealized multilayered coronary artery wall model under healthy condition is discussed. The details of the geometric model and the corresponding NURBS mesh generated are presented in Figure 5.9a and 5.9b respectively. Using the parameters selected for this case (Section 5.2) and applying the solution approach described in Section 5.3, the mathematical model was solved for 7 days with a time step of 2 minutes. The results are discussed below.

Figure 5.10 shows the temporal and spatial distribution of nanoparticles in terms of concentration normalized against the initial concentration of nanoparticles available at the lumen-wall interface for tissue uptake. Nanoparticle transport in the intima is diffusion dominated ($Pe < 1$). Diffusivity through the intima is almost three orders of magnitude higher than that in the media. As a result it takes less than an hour for the nanoparticle “diffusion” front to reach the IEL and about 6 hours for it to spread throughout the intima. From there onward, nanoparticle distribution remains fairly uniform across the intima at any given time. This agrees well with the work of Vafai et al. [25] and references therein. Note the axisymmetric nature of distribution.

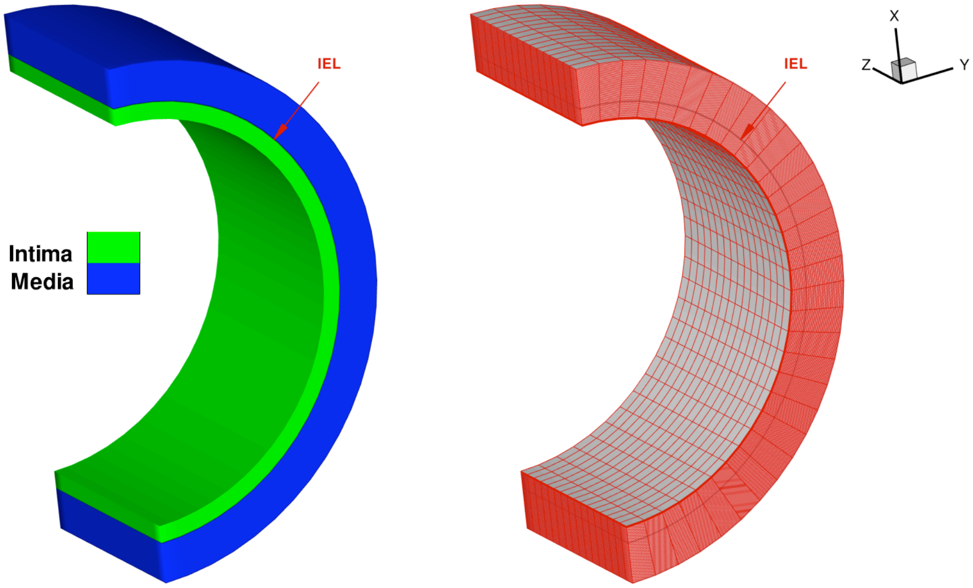

a) b)

Figure 5.9: a) The idealized normal coronary artery wall geometry with a lumen diameter of 3.5 mm and 0.5 mm wall thickness. The intima makes up approximately 1/3 of the artery wall thickness. b) The corresponding mesh consisting of 2240 NURBS element.

The IEL poses a barrier to nanoparticle transport. It takes an appreciable concentration gradient to develop across the IEL for the nanoparticles to overcome this resistance and penetrate the media (see B and C in Figure 5.10).

However, once the front reaches the media around t = 12 hours, it is mostly the advective forces ($Pe > 1$) that drives it through this slowly diffusive region toward the adventitial sink. There is a steep concentration gradient ahead of the front, while the concentration of nanoparticles in the region behind this front becomes largely uniform because of advective forces sweeping the nanoparticles away from the IEL. In about 48 hours the so-called "diffusion" front reaches the adventitia and starts clearing out through the adventitial sink. By day 4, the spatial distribution of nanoparticles is more or less uniform throughout the artery wall and reaches the same concentration level as that at the lumen-side boundary, which depletes slowly over time due to the loss of nanoparticles through the blood-wall interface. At the end of day 7 this uniform nanoparticle concentration reduces to 10% of the initial (at $t = 0$) lumen-side boundary concentration.

Drug transport shows a similar behavior to that of the nanoparticles, demonstrating the coupled nature of transport. Figure 5.11 depicts the temporal and spatial distribution of drug in the artery wall at different points in time during simulation. Drug concentration appears to be substantially lower in the intima compared to the rest of the artery wall. Furthermore, evidence of drug movement through the intima is barely noticeable.

A closer inspection of drug transport behavior during early times with a better time resolution provides a few useful insights (see Figure 5.11c). Although diffusion is relatively fast, drug distribution is not uniform in the intima during this time as suggested by Figure 5.11a. In fact a positive concentration gradient (opposite to the direction of advective flow) develops within a few hours of administration due to accumulation of drug against the IEL barrier. This can be explained by considering a couple of factors discussed below.

In diagrams I and J of Figure 5.11c, there is evidence of free drug penetration into the intima. The concentration gradient (higher drug concentration at the lumen-side boundary) drives the free drug into the tissue largely by way of diffusion ($Pe < 1$). However, with time, the free drug source at the lumen-wall interface decreases exponentially and it becomes a sink for drug within 6 hours of nanoparticle administration in the lumen. In the meantime on the nanoparticle front, aided by a constant (or very slowly decreasing with a significantly higher timescale of depletion) source at the lumen-side boundary, the nanoparticles penetrate the intima significantly within the first hour (see Figure 5.10a), and then starts accumulating near the IEL barrier. Although initially the free drug was a significant source of drug in the intima, within a few minutes the nanoparticles take over as the primary source, and then within a few hours, become the only source of drug. Therefore, as demonstrated in diagram C of Figure 5.11a, drug concentration becomes higher away from the lumen-side boundary as a direct consequence of a higher nanoparticle concentration in that region (see corresponding nanoparticle distribution in Figure 5.10). This creates a concentration gradient in a direction opposing the advective flow. Diffusive forces drive the drug toward the lumen (acting against the opposing advective forces) where it gets washed away by the blood flow. The intima never becomes a region of high drug concentration because of this fast depletion of drug through the lumen side boundary. The ratio of time constant for the exponential loss of drug and advective time scale through the intima dictates the relative rate of depletion of drug through the lumen side.

Interestingly enough, according to Figure 5.11a(B) as well as Figure 5.11c(L), there is a hint of surge in drug concentration in the intima around $t = 1$ hour, which implies that the drug gets trapped within the intima in synchronization with the nanoparticles (see Figure 5.10a(B)). As soon as the nanoparticles are able to overcome the IEL resistance and make their way into the media, drug concentration in the media increases substantially. Hence, medial concentration of drug is largely dependent on the extent of penetration of nanoparticles beyond the IEL barrier. This implies that there may not be a significant build up of drug concentration gradient across the IEL barrier for it to overcome because of its fast depletion through the lumen. Hence, a sharp increase in drug concentration can be observed in the media at $t = 12$ hours even though there is not a significant buildup of drug on the intima side of the IEL. Here the source of drug is largely the nanoparticles. Contribution from the intima side appears to be negligible.

The motion of the drug diffusion front in the media gets retarded by the metabolic decay or binding of drug to binding sites spread all over the media. Furthermore, because of this consumption of drug a region of lower drug concentration can be found lagging behind the diffusion front (essentially the NP front) in the media unlike the nanoparticles. By the end of day 7 the artery wall becomes free of drug due to its clearance through the adventitial sink and metabolic consumption in the media. Figure 5.12 provides a side-by-side comparison of the nanoparticle and drug distributions at various times.

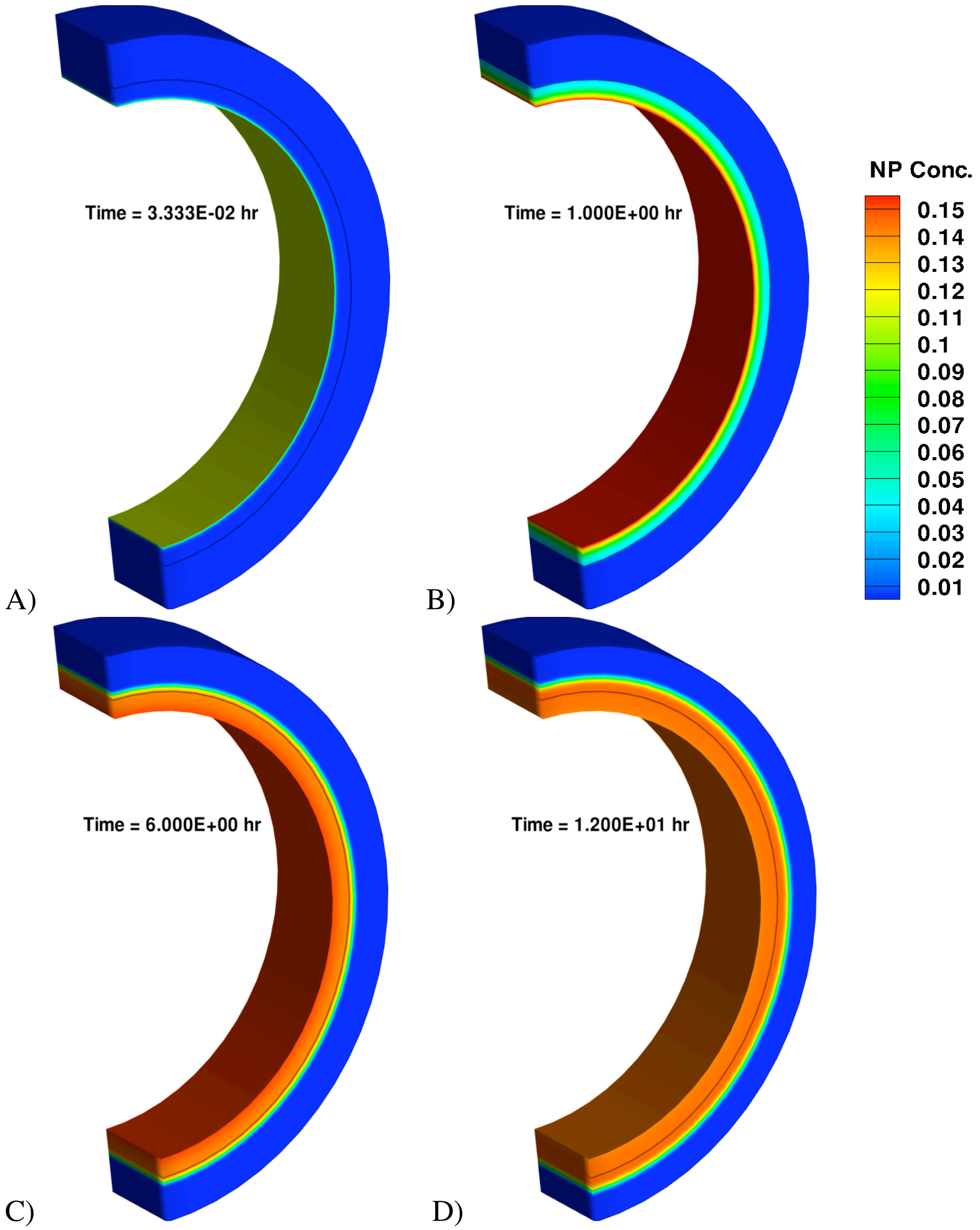

Figure 5.10a: Distribution of nanoparticles in an idealized coronary artery wall segment under normal condition at A) $t = 2$ mins, B) $t = 1$ hr, C) $t = 6$ hrs, and D) $t = 12$ hrs in terms of concentration (normalized).

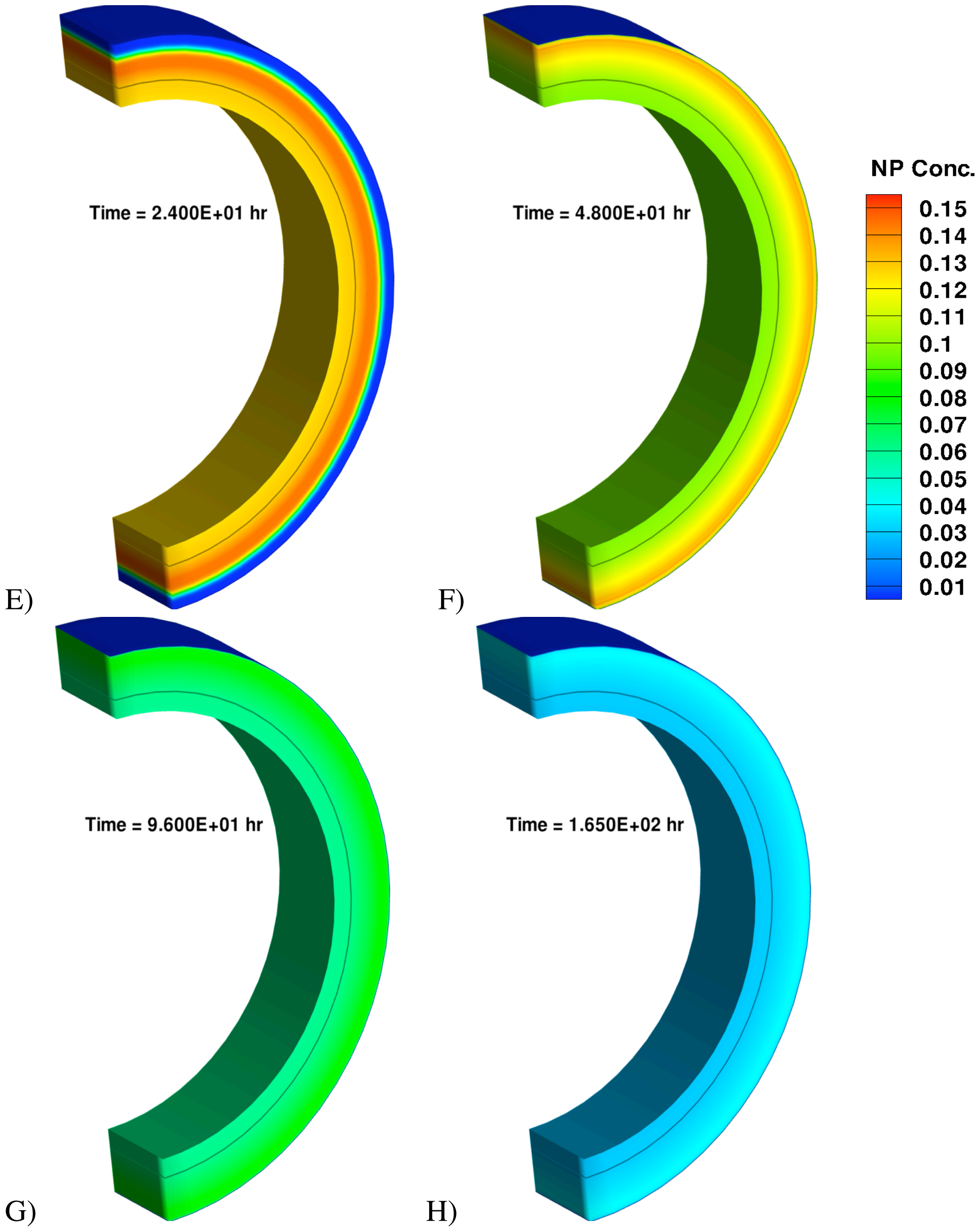

Figure 5.10b: Distribution of nanoparticles in an idealized coronary artery wall segment under normal condition at E) *t* = 1 day, F) *t* = 2 days, G) *t* = 4 days, and H) *t* = 7 days in terms of concentration (normalized).

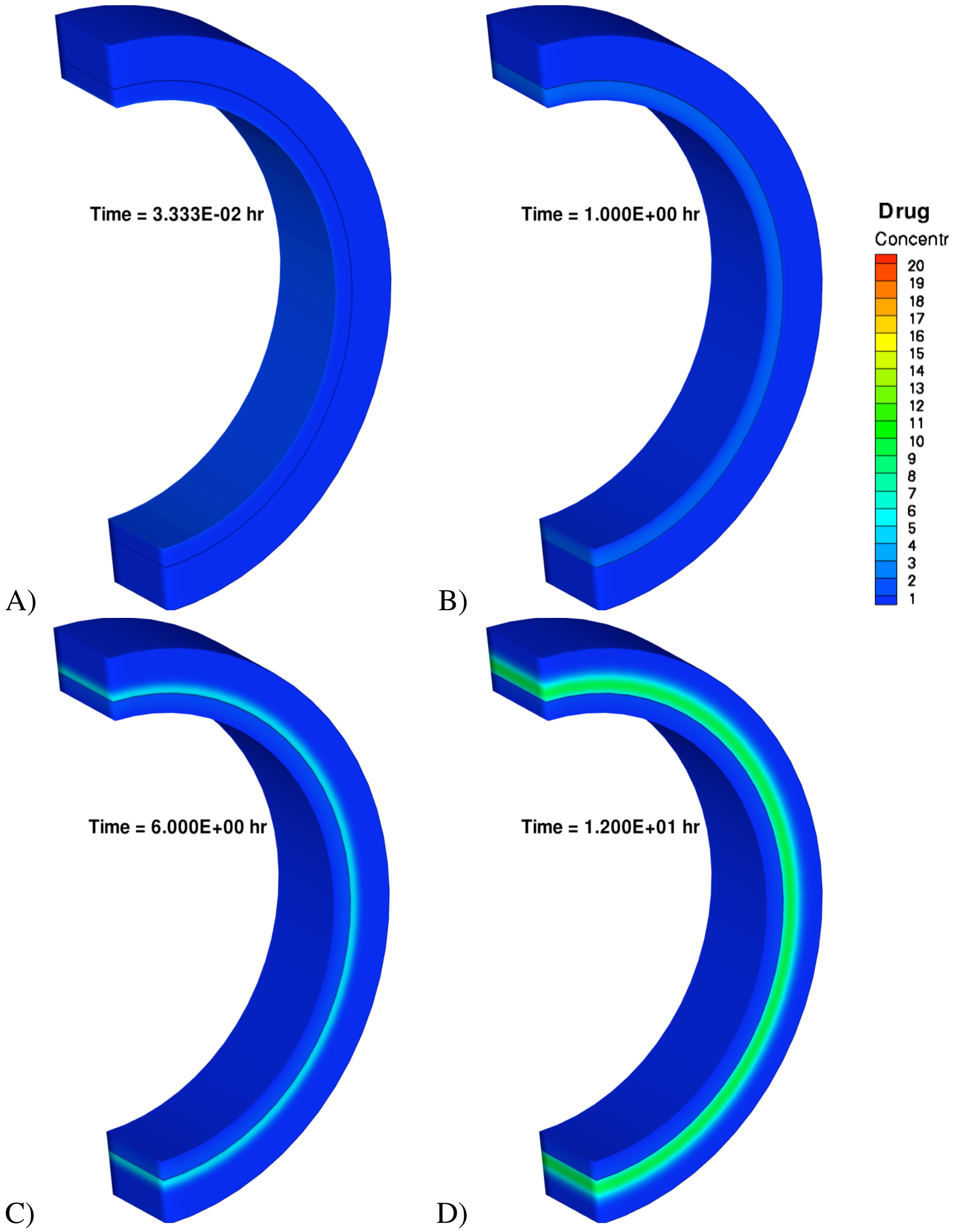

Figure 5.11a: Drug distribution in terms of concentration (normalized) in an idealized coronary artery wall segment under normal condition at A) $t = 2$ mins, B) $t = 1$ hr, C) $t = 6$ hrs, and D) $t = 12$ hrs.

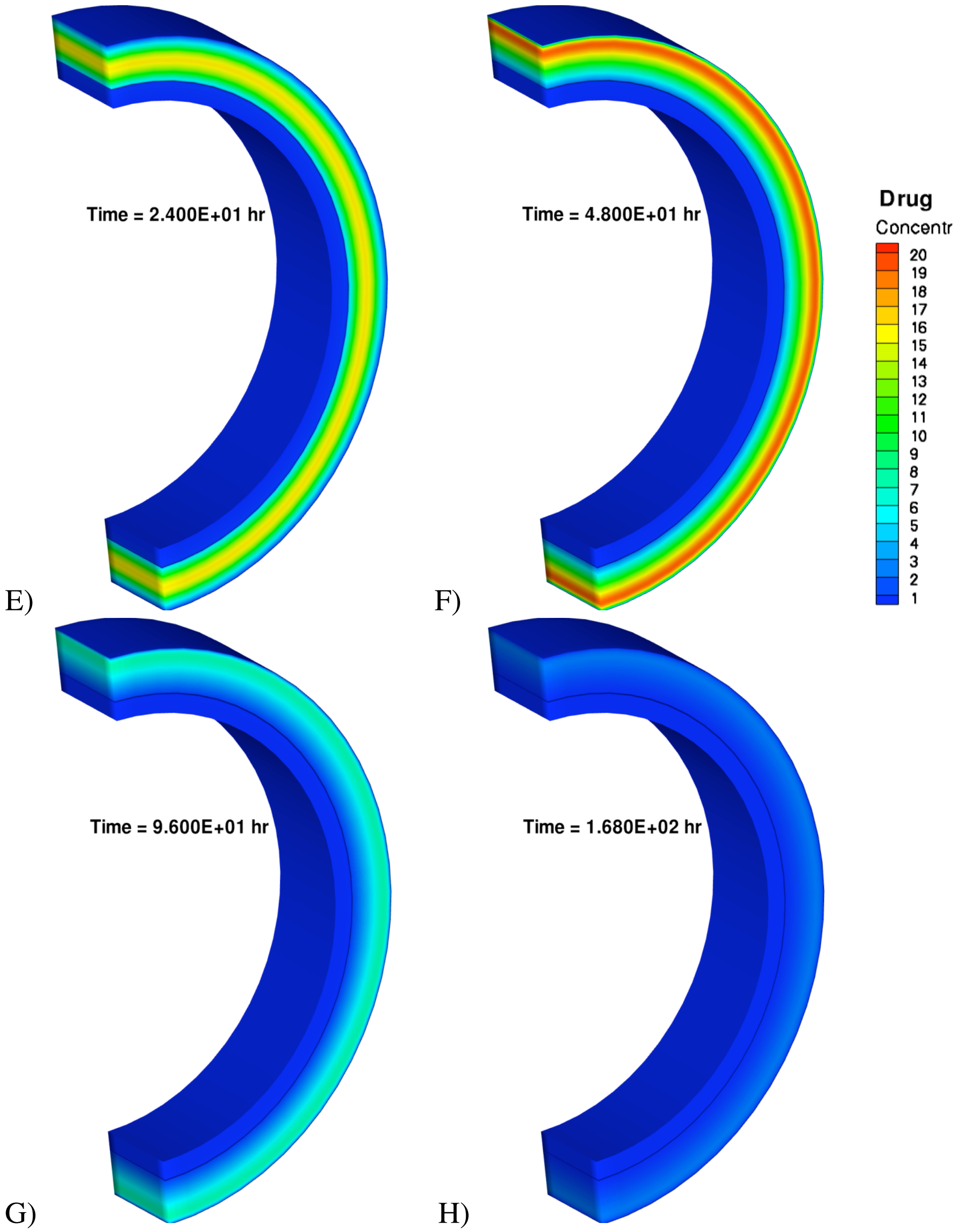

Figure 5.11b: Drug distribution in terms of concentration (normalized) in an idealized coronary artery wall segment under normal condition at E) $t = 1$ day, F) $t = 2$ days, G) $t = 4$ days, and H) $t = 7$ days.

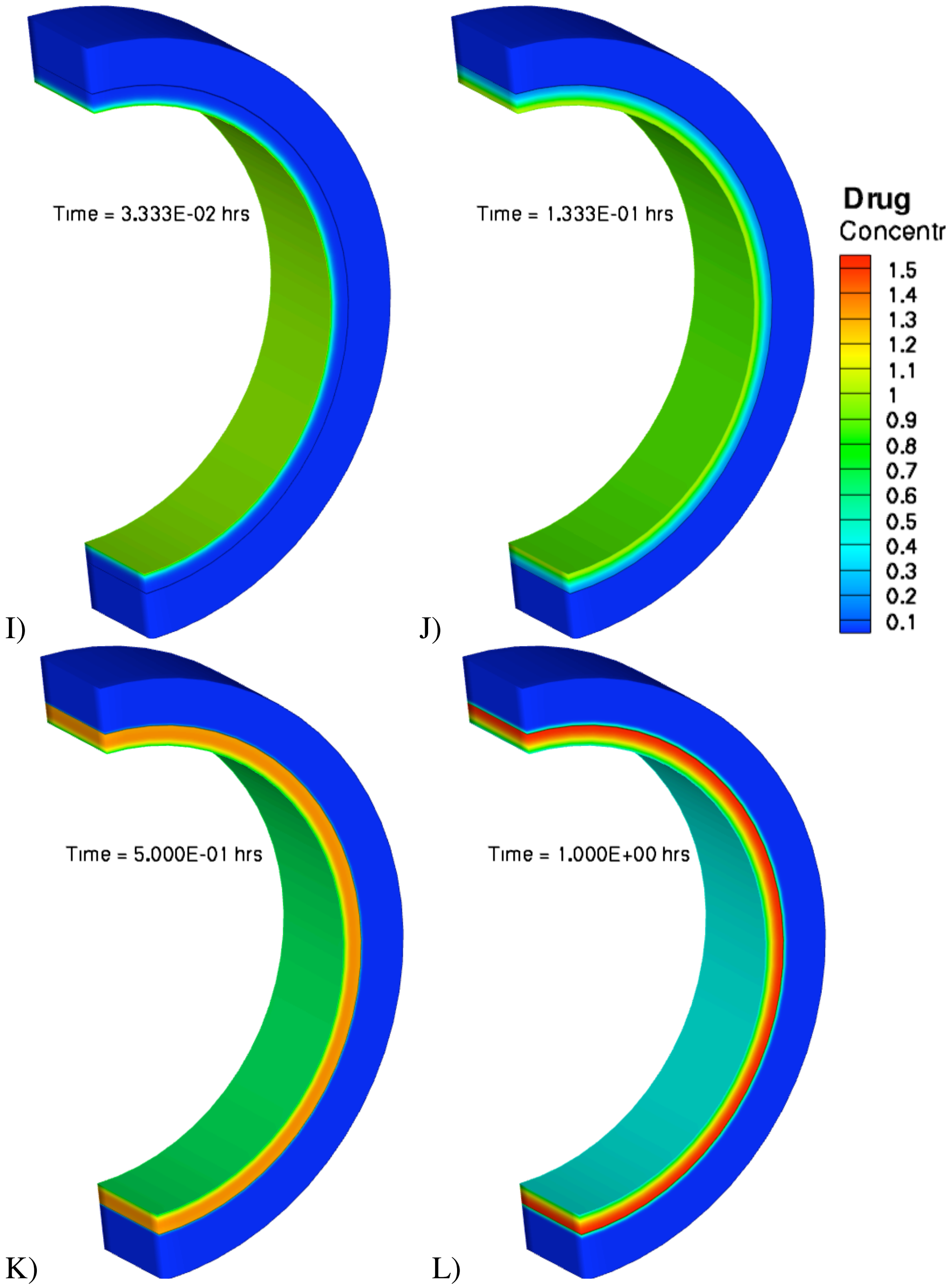

Figure 5.11c: Drug distribution in terms of concentration (normalized) in an idealized coronary artery wall segment under normal condition at I) *t* = 2 mins, J) *t* = 16 mins, K) *t* = 30 mins, and L) *t* = 60 mins.

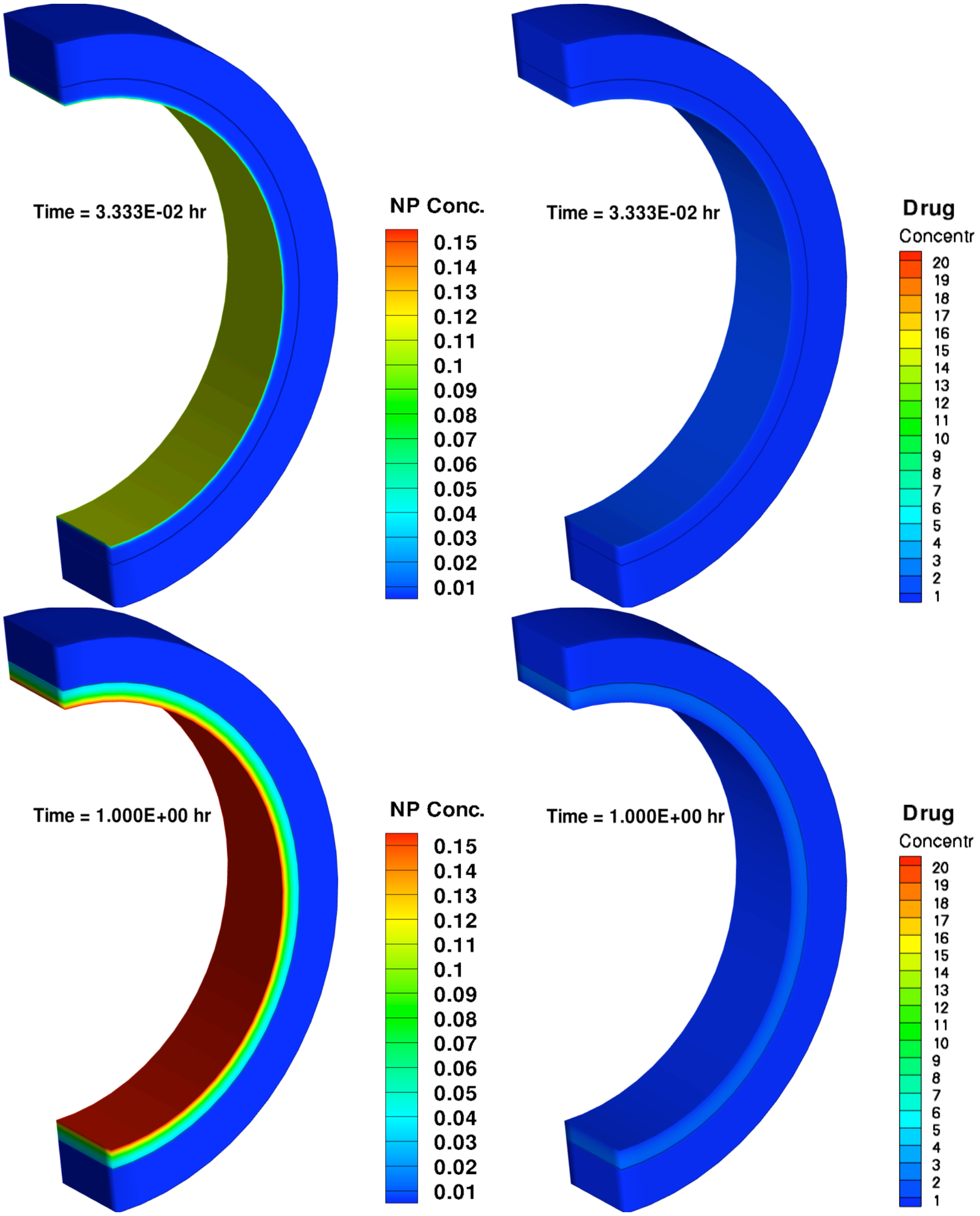

Figure 5.12a: Distribution of nanoparticles (left) and the drug (right) in an idealized coronary artery wall segment under normal condition at *t* = 2 mins (top) and *t* = 1 hr (bottom), in terms of concentration (normalized).

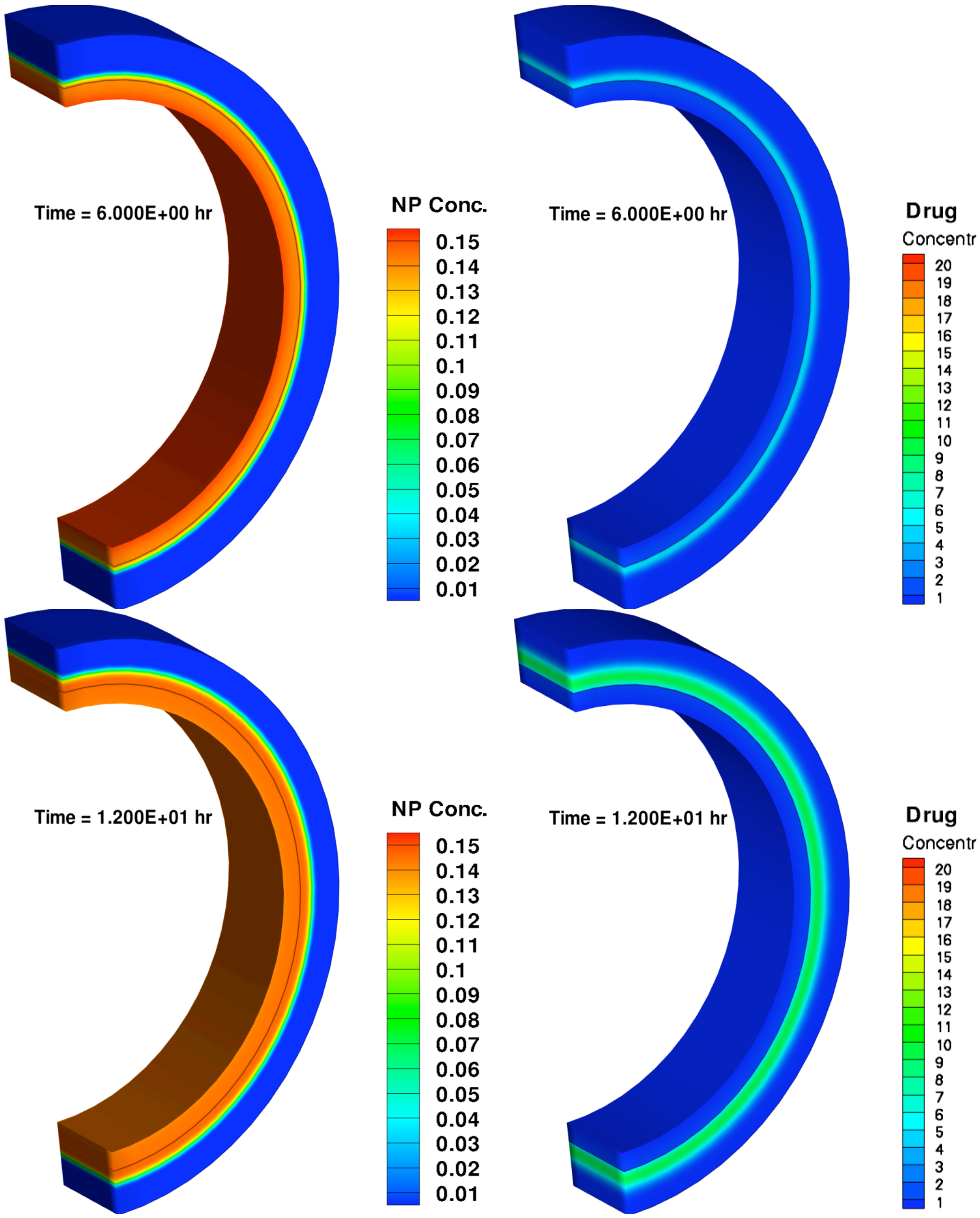

Figure 5.12b: Distribution of nanoparticles (left) and the drug (right) in an idealized coronary artery wall segment under normal condition at t = 6 hrs (top) and t = 12 hrs (bottom), in terms of concentration (normalized).

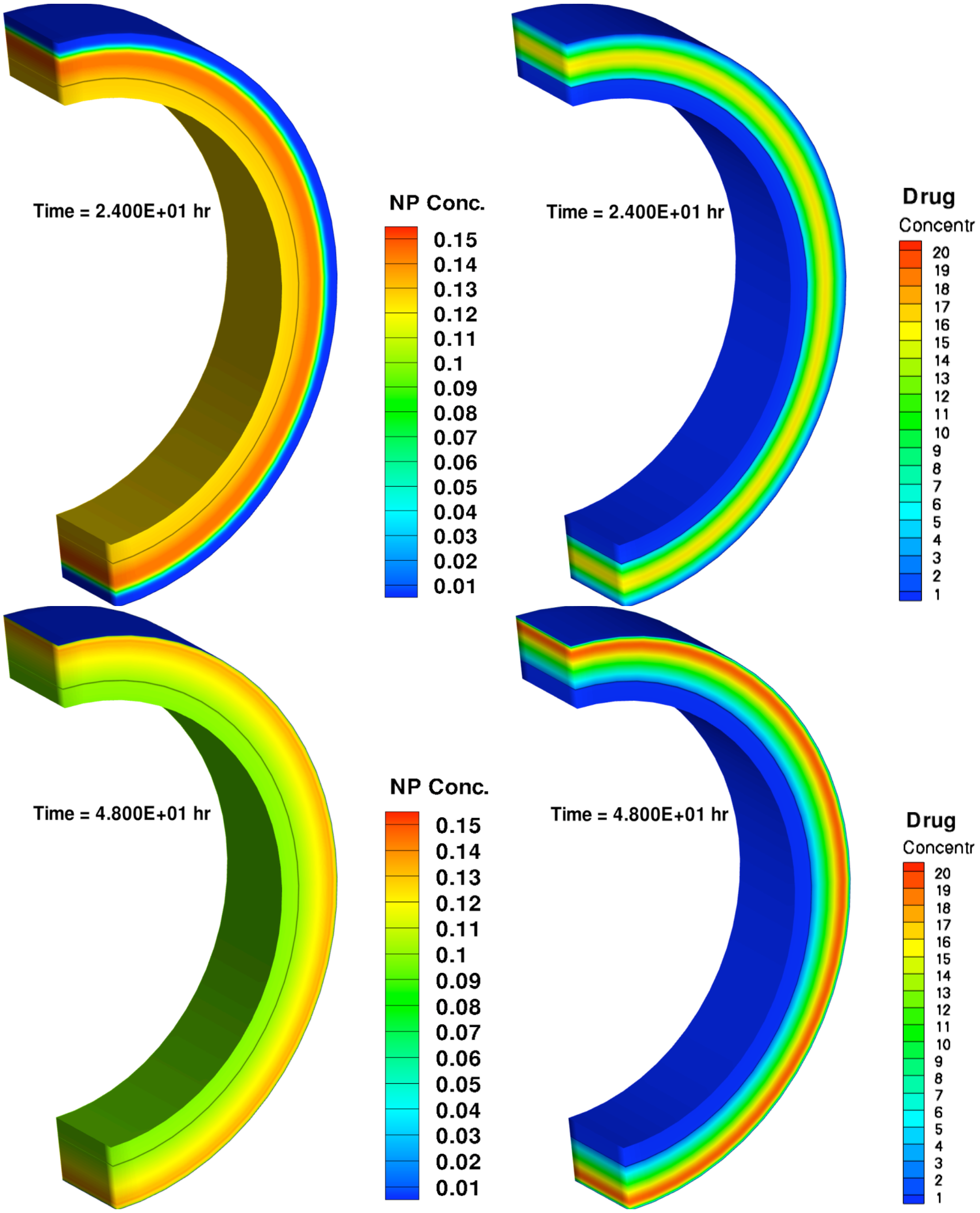

Figure 5.12c: Distribution of nanoparticles (left) and the drug (right) in an idealized coronary artery wall segment under normal condition at *t* = 1 day (top) and *t* = 2 days (bottom), in terms of concentration (normalized).

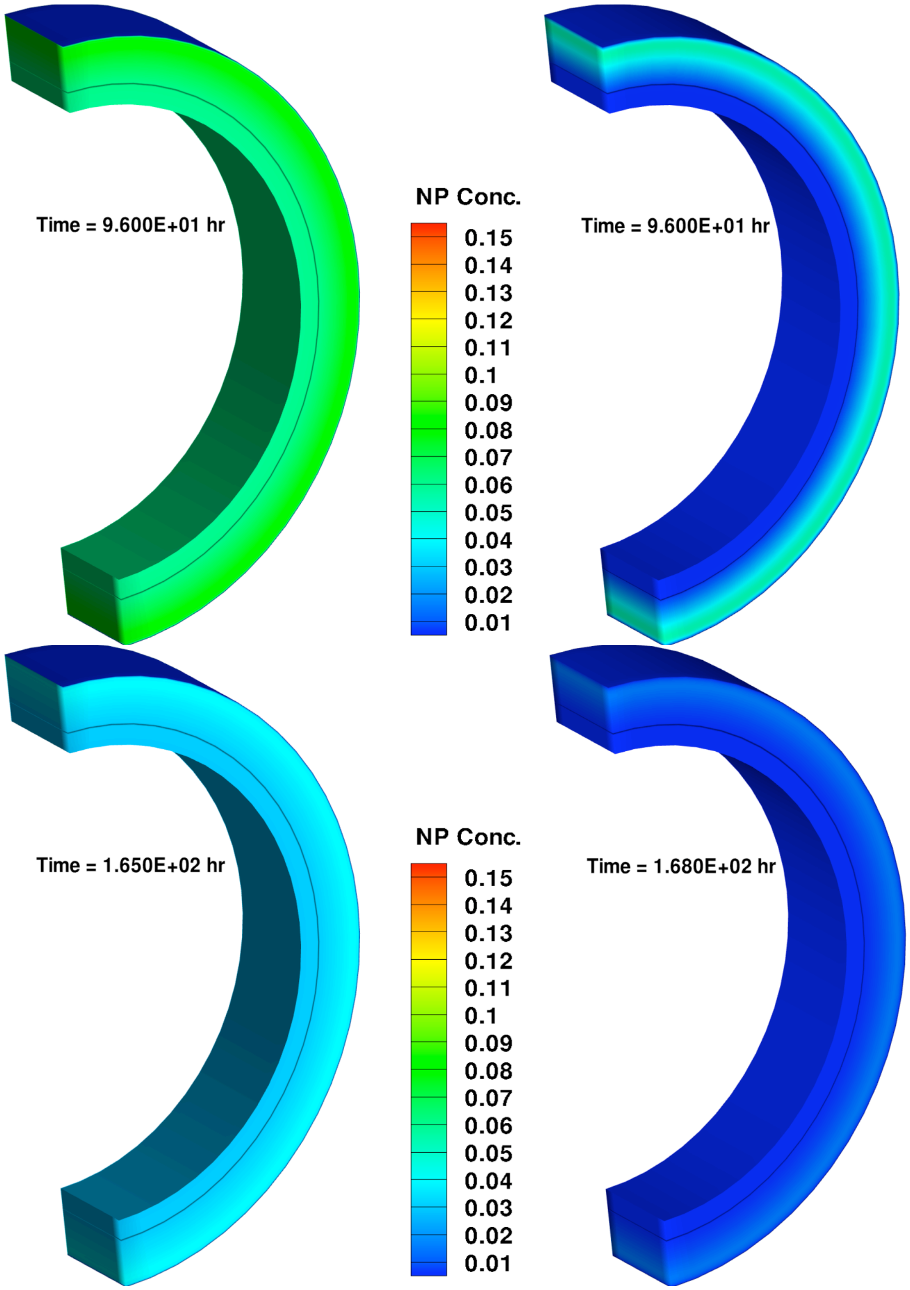

Figure 5.12d: Distribution of nanoparticles (left) and the drug (right) in an idealized coronary artery wall segment under normal condition at *t* = 4 days (top) and *t* = 7 days (bottom), in terms of concentration (normalized).

5.3.2 Drug distribution in a diseased artery wall with a vulnerable plaque

A vulnerable plaque model with a lipid core encased by a very thin fibrous cap was incorporated in the idealized multilayered cylindrical wall model. The plaque dimensions were determined by the necrotic core angle, radius of the artery lumen and relative core thickness [75]. For a plaque with a necrotic core arc angle of $\theta = 85$ degrees, the core thickness can be approximated to be $b = 0.5$ mm with a longitudinal plaque length of $c = 5$ mm. Fibrous cap thickness is typically less than 90 μm. The idealized plaque was placed at the center of the artery wall segment. Figure 5.13 shows the NURBS mesh generated for this model, while Figure 5.14 details the structure and composition, along with relevant dimensions.

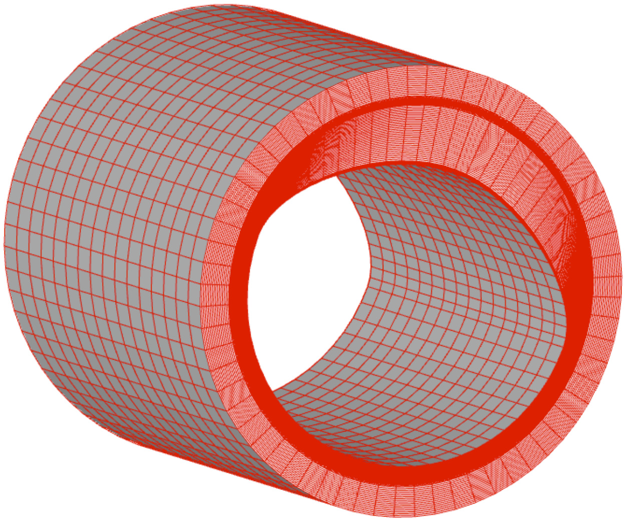

Figure 5.13: A cut-away view of the idealized diseased artery wall mesh, consisting of 20480 NURBS elements.

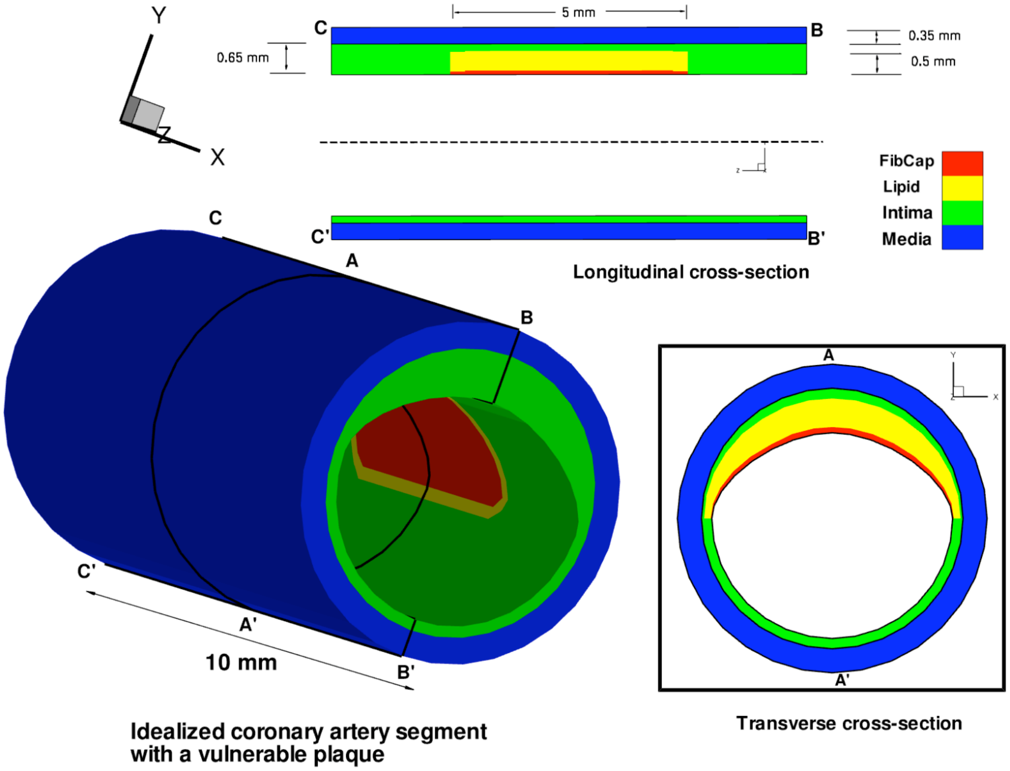

Longitudinal cross-section

Idealized coronary artery segment with a vulnerable plaque

Transverse cross-section

Figure 5.14: Diseased artery wall model with a vulnerable plaque. This is a schematic of the transverse cross-section of the artery wall (bottom) taken half way through the longitudinal length, highlighting the lipid rich necrotic core encased by the fibrous cap of the vulnerable plaque, along with the longitudinal cross-section of the artery wall model (top) showing increased intimal thickness.

The diseased artery has been modeled to have four distinct regions with varying diffusive properties, where $D_{inima} > D_{fc} > D_{media} > D_{lipid}$. While the healthy part of the diseased artery shows a similar transport behavior to that of a normal artery as discussed in Section 6.3.1, for the diseased part it is considerably different. In fact, the existence of the plaque has a significant bearing on the overall drug distribution within the artery wall. The temporal and spatial distribution of nanoparticles is presented in Figure 5.15. Note the distribution is highly 3D in nature.

Much like the healthy or normal artery case, there is fast diffusion of nanoparticles within the intima, making the intimal concentration fairly uniform. On the other hand, though the nanoparticles penetrate the fibrous cap fairly quickly, the radial transport through the lipid core is slow and retarded. As a result, while the nanoparticles reach the IEL within an hour in the healthy parts, there is hardly any penetration of the lipid core (the target region). Soon enough these nanoparticles start migrating from the healthy part of the arterial media into the diseased portion by way of planar diffusion (isotropic). Therefore, it can be said that the healthy part of the artery wall essentially acts as a nanoparticle reservoir and enhances transport to the diseased part.

The nanoparticle concentration in the lipid core reaches a maximum within 24 to 48 hours. After this period, it diminishes with time. By the end of day 4 the nanoparticle distribution becomes largely uniform throughout the artery wall.

Figure 5.15 shows the corresponding time evolution of drug concentration in the diseased artery. Drug diffusion is highly anisotropic, that is, diffusivity in the planar direction is almost three orders of magnitude faster than the radial direction. The much faster planar diffusion (anisotropic) facilitates drug transport into the diseased part significantly. A comparison of item F in Figure 5.15b with that of Figure 5.16b illustrates this point very well. At time t = 48 hours, there is an appreciable spatial variation of nanoparticle concentration. The highest nanoparticle concentration occurs in the healthy part of the media and the lipid core within the diseased part of the same cross-section. The corresponding drug distributions show a slightly different picture. The medial concentration of drug is fairly uniform on both the healthy and diseased sides, indicating that in addition to the drug released from the nanoparticles that have made their way into the diseased part, much of the drug comes from the healthy part of the media (a high nanoparticle concentration area) because of faster planar diffusion. Therefore, although the radial transport of drug through the lipid core never makes it to the media, this influx of drug from the planar (circumferential and axial) direction substantially increases the medial drug concentration earlier than expected (between 24 to 48 hours of administration).

Furthermore, during this time period, the lipid core attracts and accumulates the hydrophobic drugs released from the nanoparticles trapped within. This provides a long residence time for the drugs, enhancing their potential therapeutic effect in the target region.

After reaching a maximum around day 2, drug concentration in the lipid core diminishes due to its transport to the surrounding outer intima with a two orders of magnitude faster diffusivity. The medial concentration suffers a similar fate because of this so called dumping of drug in the intermediate intima layer, in addition to the medial consumption of drug. By the end of the week, the diseased artery is cleared of any drug traces.

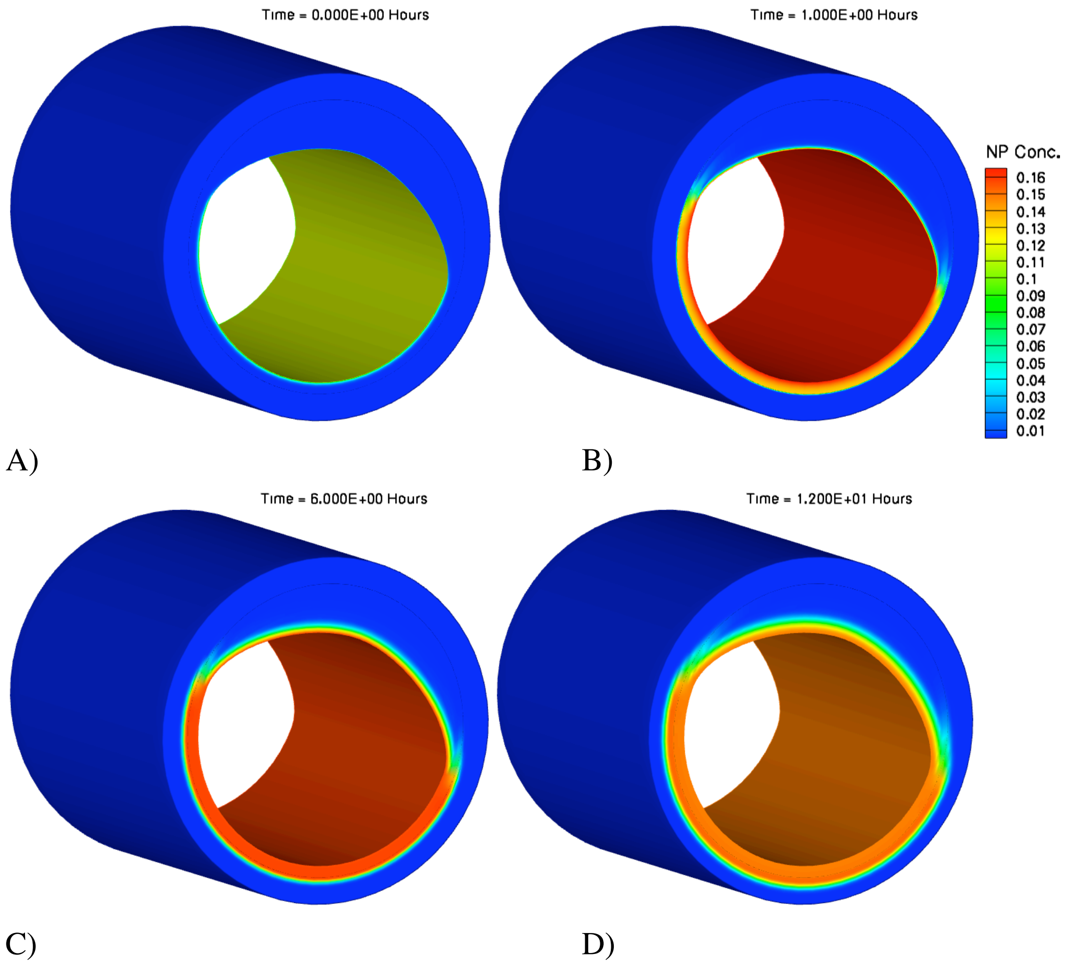

Figure 5.15a: Distribution of nanoparticles in an idealized coronary artery wall segment with a vulnerable plaque under diseased condition at A) t = 2 mins, B) t = 1 hr, C) t = 6 hrs, and D) t = 12 hrs in terms of concentration (normalized).

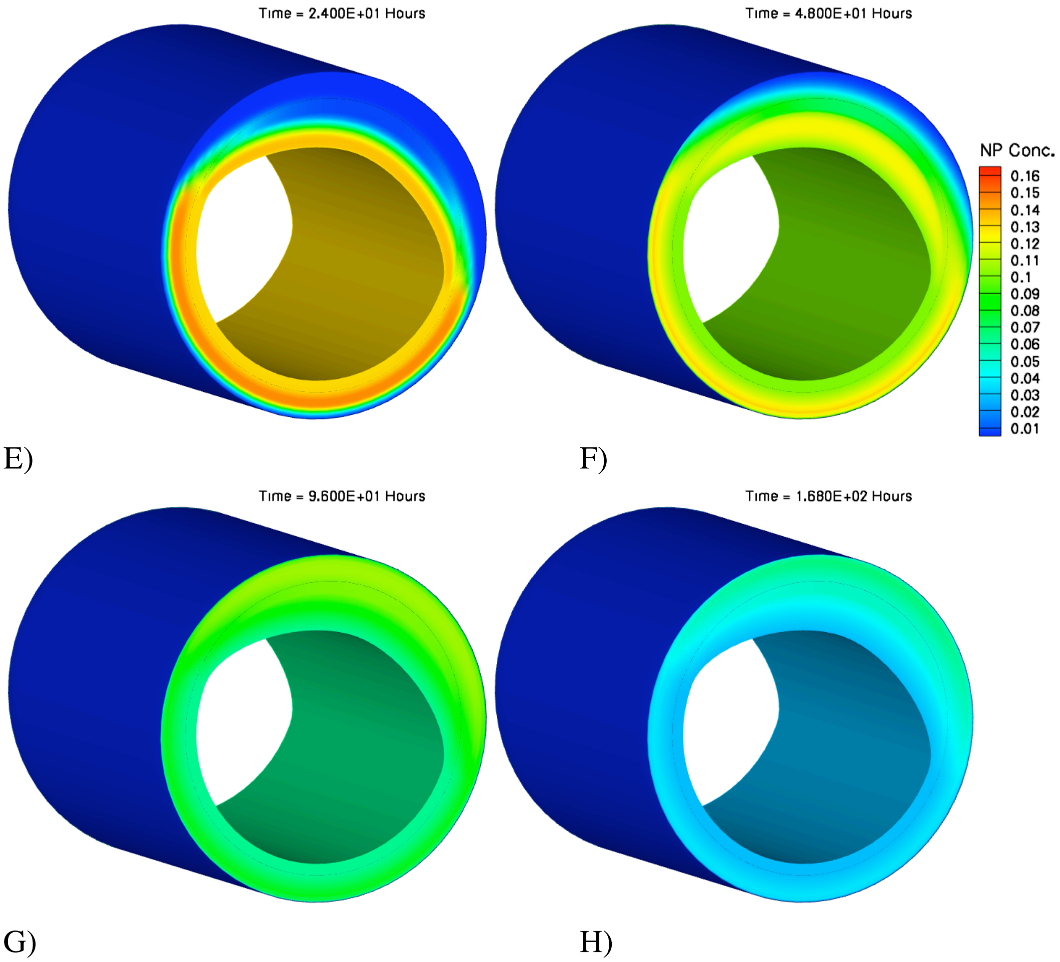

Figure 5.15b: Distribution of nanoparticles in an idealized coronary artery wall segment under diseased condition characterized by a vulnerable plaque at E) $t = 1$ day, F) $t = 2$ days, G) $t = 4$ days, and H) $t = 7$ days in terms of concentration (normalized).

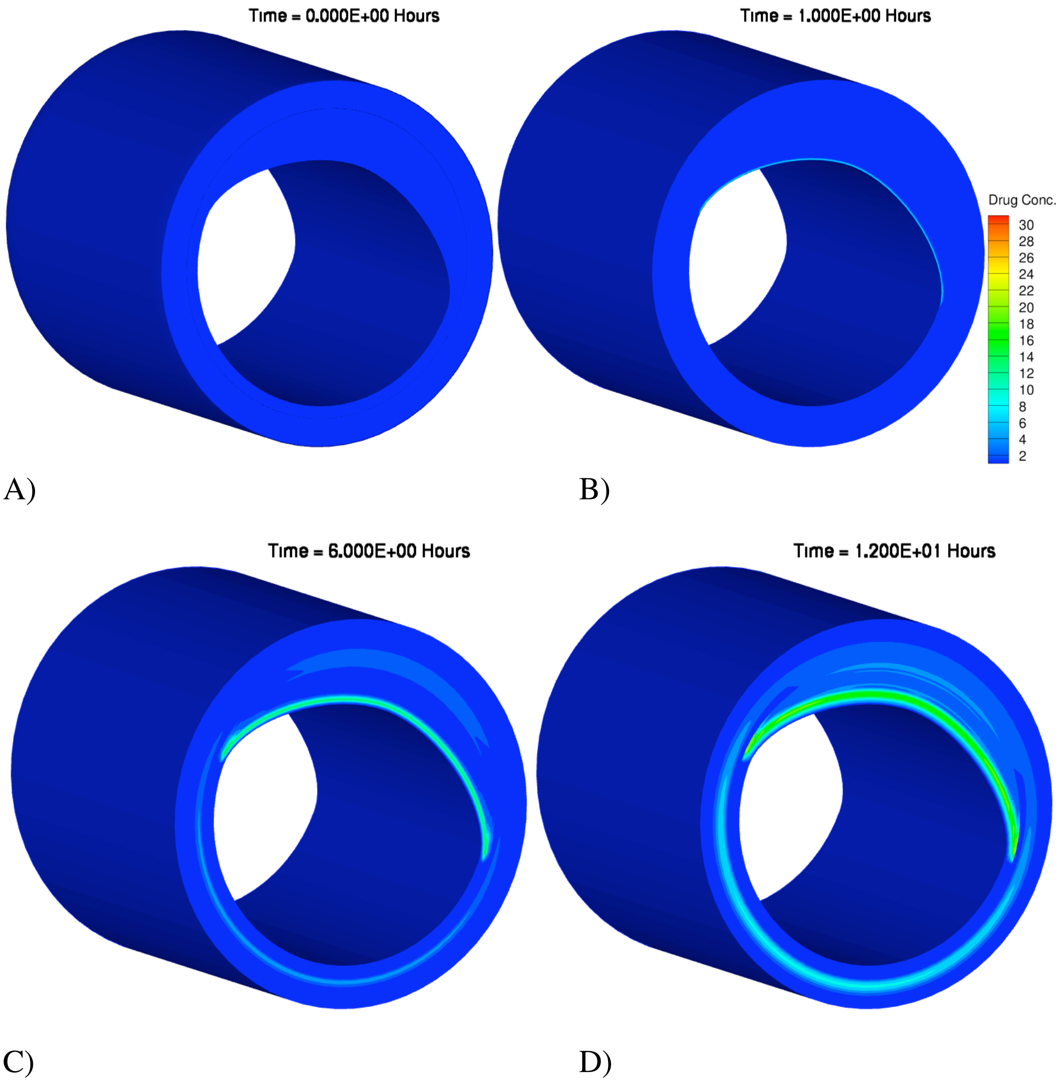

A) B) C) D)

Figure 5.16a: Drug distribution in an idealized coronary artery wall segment with a vulnerable plaque under diseased condition at A) t = 2 mins, B) t = 1 hr, C) t = 6 hrs, and D) t = 12 hrs in terms of concentration (normalized).

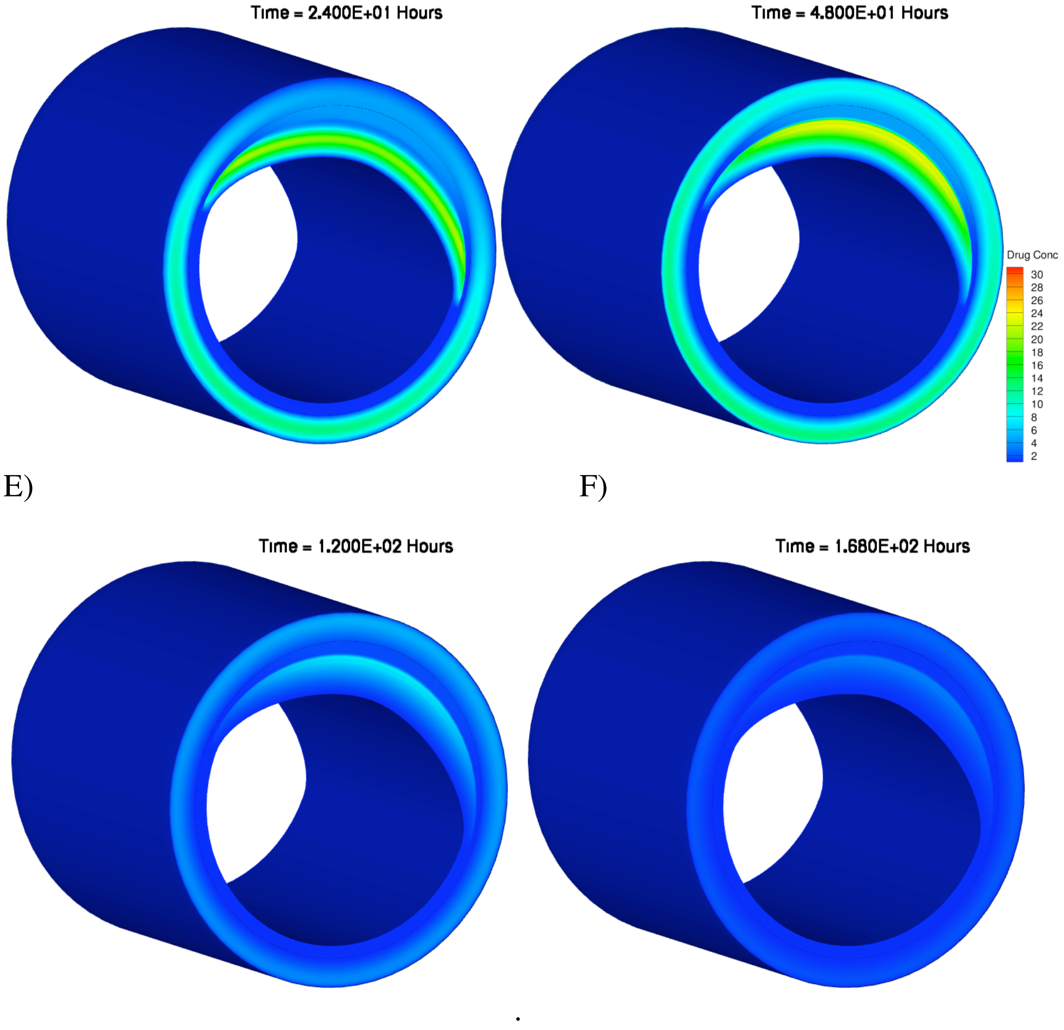
Time = 2.400E+01 Hours

Time = 4.800E+01 Hours

Time = 1.200E+02 Hours

Time = 1.680E+02 Hours

E)

F)

G)

H)

Figure 5.16b: Drug distribution in an idealized coronary artery wall segment under diseased condition characterized by a vulnerable plaque at E) t = 1 day, F) t = 2 days, G) t = 4 days, and H) t = 7 days in terms of concentration (normalized).

CHAPTER 6

Application to Patient-Specific Geometry

A chain of specific procedures, referred to as the vascular modeling pipeline, developed by Zhang et al. [76] has been used to construct hexahedral solid NURBS for patient-specific geometric modeling of the Left Coronary Artery (LCA) directly from CT imaging data. Figure 6.1 illustrates the steps in building this geometric model using a portion of the coronary arterial tree of a healthy over 55 volunteer obtained from 64-slice CT angiography.

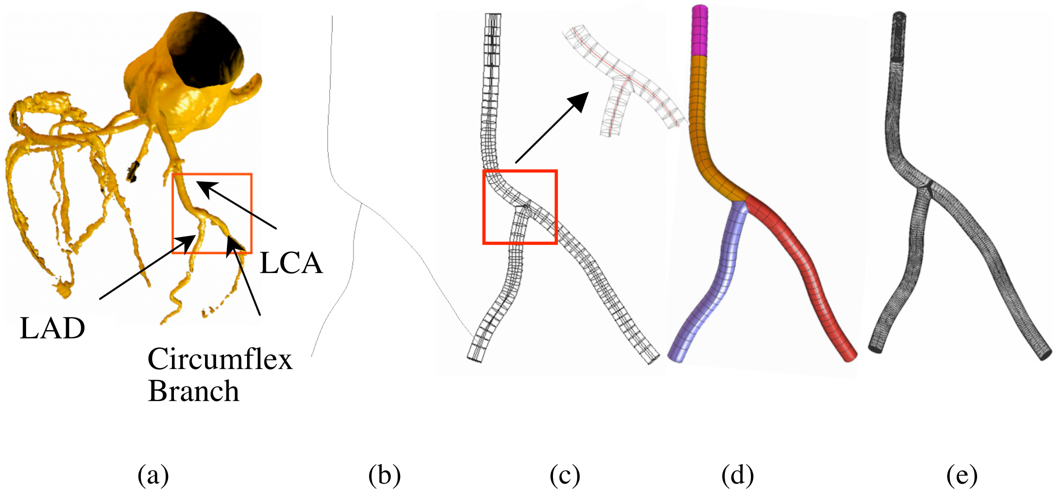

Figure 6.1: Skeleton-based sweeping method and meshing. (a) isocontour of LCA, (b) path, (c) sweeping along the path—templated circle translated and rotated to each cross-section, (d) solid NURBS mesh, (e) NURBS wire-mesh. [76]

The hexahedral solid NURBS model for the lumen generated by Zhang et al. (see Figure 6.1) was modified to include an artery wall of uniform thickness surrounding the lumen using isogeometric modeling techniques [47]. The lumen boundary was extended radially by 15% of the radius of the lumen. This generated an artery wall with a thickness of 0.6 mm approximately, which was then decoupled from the lumen to obtain the patient-specific coronary artery wall geometry.

6.1 DRUG DISTRIBUTION IN A NORMAL ARTERY WALL

Figure 6.2 shows the details of the healthy artery wall model. There are four patches along the length of the LCA with each patch again split into two concentric patches at approximately 1/3 depth into the artery wall thickness. The inner patch represents the intima, while the outer patch represents the media. This geometric discontinuity at the intima-media interface was essential to implement the Kedem-Katchalsky model for concentration jump condition across the IEL (see Section 2.2.4). The corresponding NURBS mesh used in the simulations can be found in Figure 6.3.

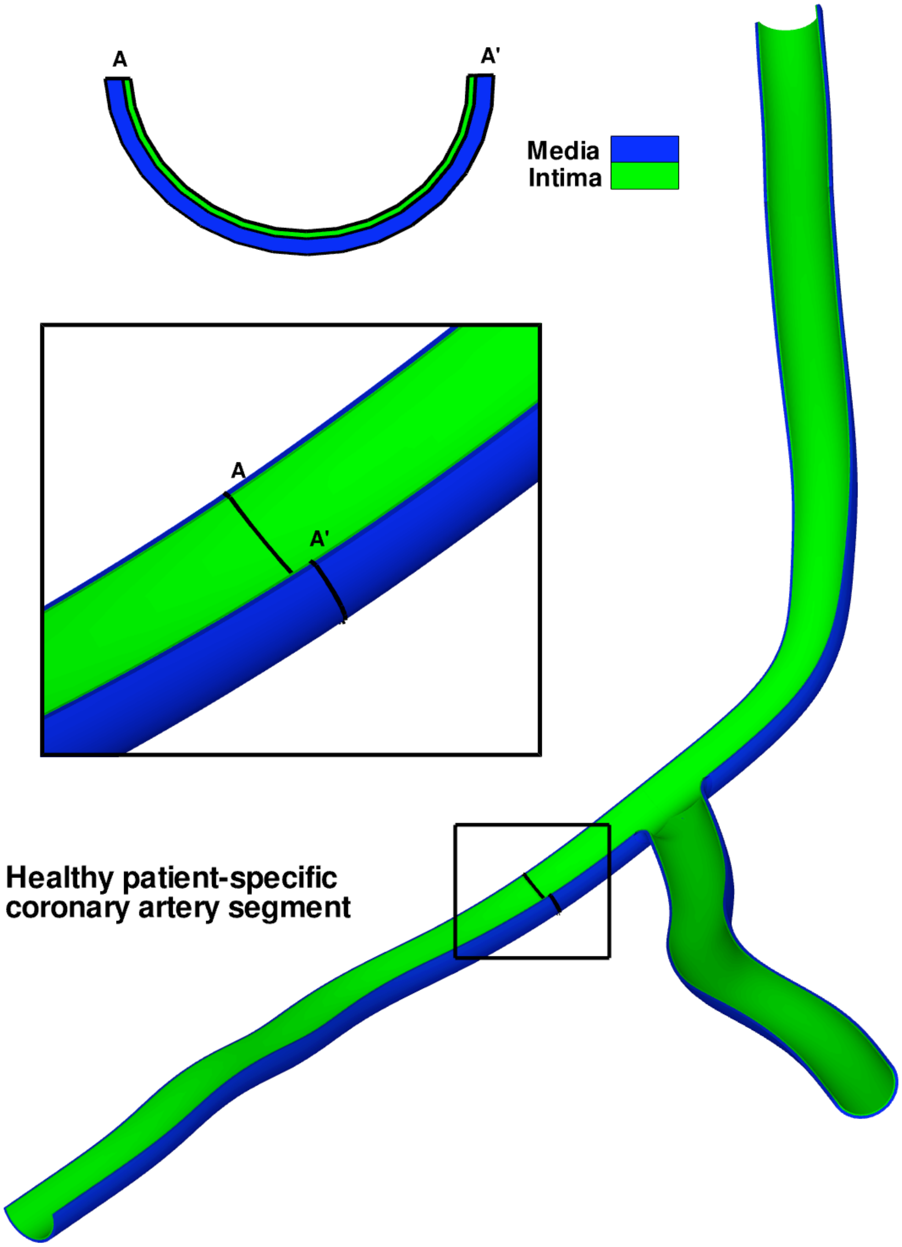

Figure 6.2: Schematic of the cut away view of a healthy patient-specific left coronary artery segment showing the intima in green and the media in blue. A cross-section is taken along A-A' highlighting these two homogeneous parts separated by the IEL.

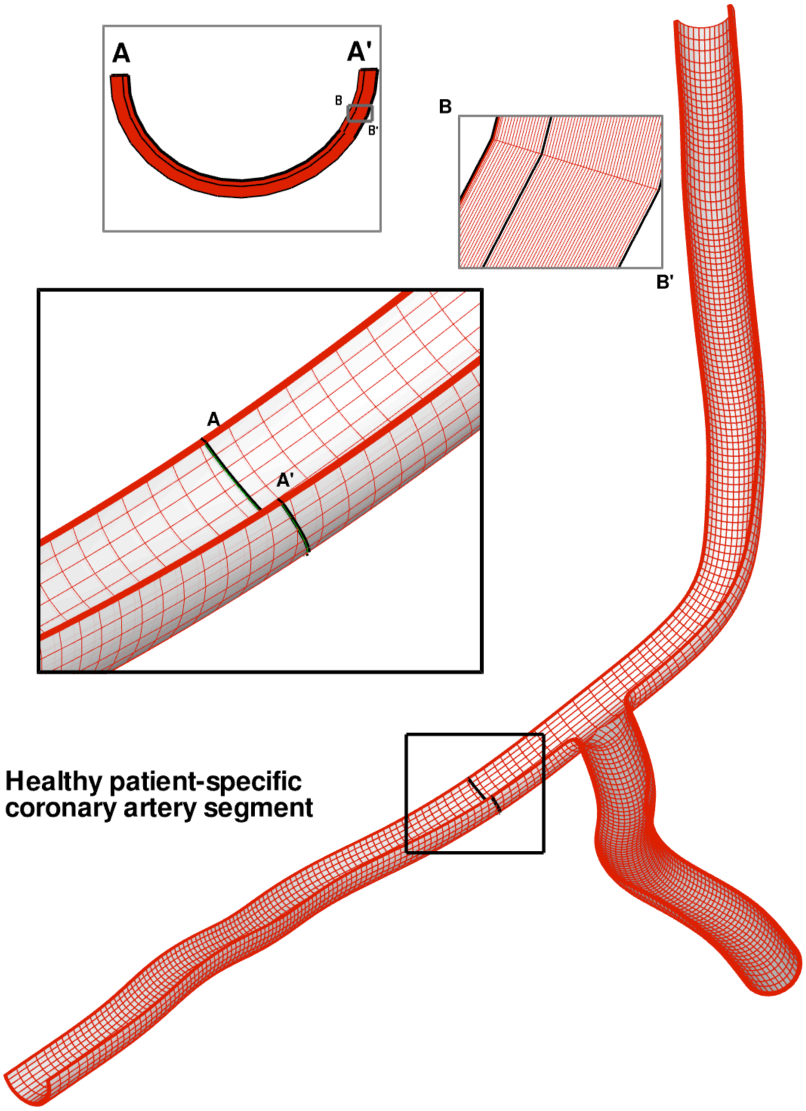

Figure 6.3: A cut-away view of the three-dimensional hexahedral NURBS mesh used for the normal (healthy) patient-specific coronary artery wall segment used in simulation. The artery geometry was divided into four NURBS patches along the length of the segment, while each of these patches were split in two along the radial direction at the location of the internal elastic lamina. The model consists of 121, 212 control points, solved over 7 days with a time step of 2 minutes.

The nanoparticle wall deposition for the patient specific artery was obtained from a complementary work carried out by Calo et al. [36]. The simulation setup is shown in Figure 6.4. A catheter releases drug-encapsulated nanoparticles radially into the lumen, with/without free drug in the solution, of the same coronary artery segment under consideration, that is, the LCA over six cardiac cycles. Although blood flow washes away the majority of these nanoparticles, some of the nanoparticles marginate toward the artery wall. Here the assumption is that the particles that reach the outer diameter of the lumen are available for tissue uptake. A Navier-Stokes solver coupled to the scalar advection-diffusion equation was used in a computational framework to get the temporal and spatial distribution of nanoparticles at the wall. The wall deposition thus obtained was then normalized against the highest nanoparticle concentration to get the spatial distribution of nanoparticles at the lumen-wall interface (see Figure 6.5). Quite expectedly, the nanoparticles accumulate near the bifurcation area. Flow through this recirculation zone is delayed as the residence time of circulating elements is prolonged. Such flow separation has been reported to enhance platelet [77] and thus nanoparticle deposition.

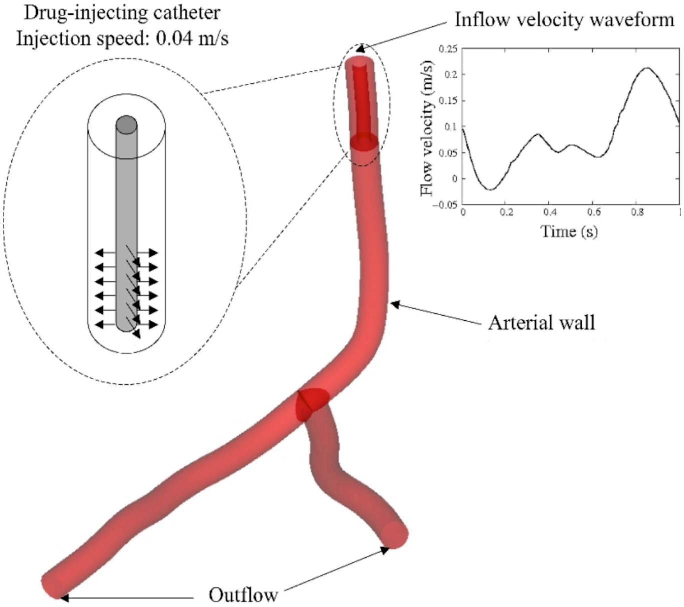

Figure 6.4: Schematic describing the problem setup for the simulation of catheter-based local drug and drug-encapsulated nanoparticle delivery. [36]

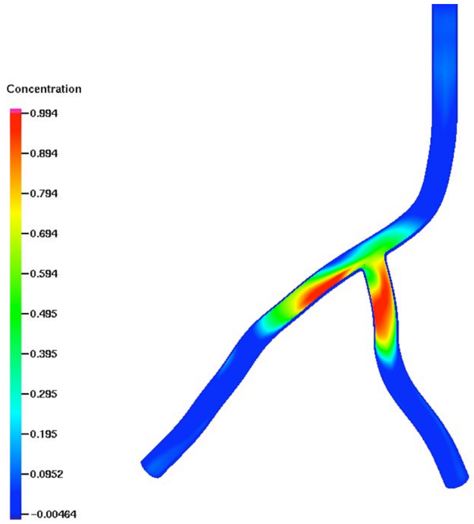

Figure 6.5: The nanoparticle wall deposition data at $t = 0$ that acts as the lumen side boundary condition for the artery wall transport model, decoupled from the lumen.

In Figure 6.6, the location of the three representative transverse slices are presented, which are taken in order to investigate time evolution of local drug distribution in a healthy patient-specific coronary artery segment. These locations were chosen such that the results can be compared with those for the diseased artery case, where slice 1 goes through the vulnerable plaque (see Figure 6.13). Slice 2 and 3 are there to provide insight into the effect of plaque heterogeneity on overall drug distribution of the artery wall segment, hence, will be discussed with the diseased case in Section 6.2.

It has already been established that the spatial distribution of nanoparticles at a given point in time greatly influences local drug distribution. Due to this closely coupled nature of transport between the two, the time evolution of drug can be best understood if it is analyzed side-by-side with the nanoparticles.

Let us first consider slice 1 which happens to be at a region with a relatively dense wall deposition of nanoparticles. This spatial variation in the nanoparticle concentration at the lumen side boundary has a significant effect on the overall time evolution of nanoparticle distribution, and therefore drug distribution, when compared to the idealized case where the nanoparticle wall deposition was uniform at the lumen-side boundary. As the nanoparticles near the more dense wall deposition region penetrate the intima radially (see Figure 6.8a), one can clearly see nanoparticle movement in the circumferential direction within the intima due to comparable planar diffusion (isotropic). Hence, they are now able to access areas that did not have a significant wall deposition at the outset.

This implies that although nanoparticle wall deposition may be highly localized, once they penetrate the artery wall, they tend to spread out toward a more uniform distribution.

Similar to the idealized case, the nanoparticles (where available) largely remain within the intima during the first 12 hours since their release, though their distribution is more 3D in nature. Apart from this variation in spatial concentration introduced by the inhomogeneous initial wall deposition, the overall nanoparticle transport characteristics are comparable to the idealized case because of its assumed isotropic diffusion.

Drug distribution on the other hand is no longer axisymmetric and shows considerable variation compared to the idealized case because of the cumulative effect of a number of factors. First thing to note is the relatively low intensity of drug concentration compared to the ideal case as a direct consequence of two phenomena. Firstly, the spatial variation of nanoparticle concentration within a wide range of values, which means for a given control volume, the number of nanoparticles at play here is significantly lower than in the idealized case. Secondly, due to the 3D nature of the problem, the considerably faster planar (both circumferential and axial) diffusion drives much of the drug away from these pockets of higher concentration of nanoparticle that translates to higher drug availability.

According to Figure 6.9 and 6.10 the drug appears to accumulate preferably at a specific region. This pocket of higher drug concentration first appears around 6 hours into the simulation. With time this region grows wider in the planer direction up to a maximum, after which it starts depleting. A close inspection of Figure 6.10b(E) reveals a slow emergence of another region with localized high drug concentration at approximately 120 degrees to the first one.

The growth and shrinking of this high concentration region may be attributed to the initial burst of drug release from nanoparticles such that the drug availability peaks around 24 hours, then diminishes with time (see Figure 4.5). Consequently, drug concentration reaches a peak at the end of day 1 at these two locations.

Apart from that, this peculiar behavior of localization of drug to create a high concentration region is most likely a consequence of 3D geometry induced complex transport forces at play. Interestingly, these two so-called pockets are located at either end of the higher nanoparticle concentration region (the yellow band in item E of Figure 6.8b) that appears in the media at t = 24 hours. The highly anisotropic drug diffusivity coupled with the cumulative effect of nanoparticle wall deposition in the surrounding area may have had a superimposing effect and contributed to this phenomenon.

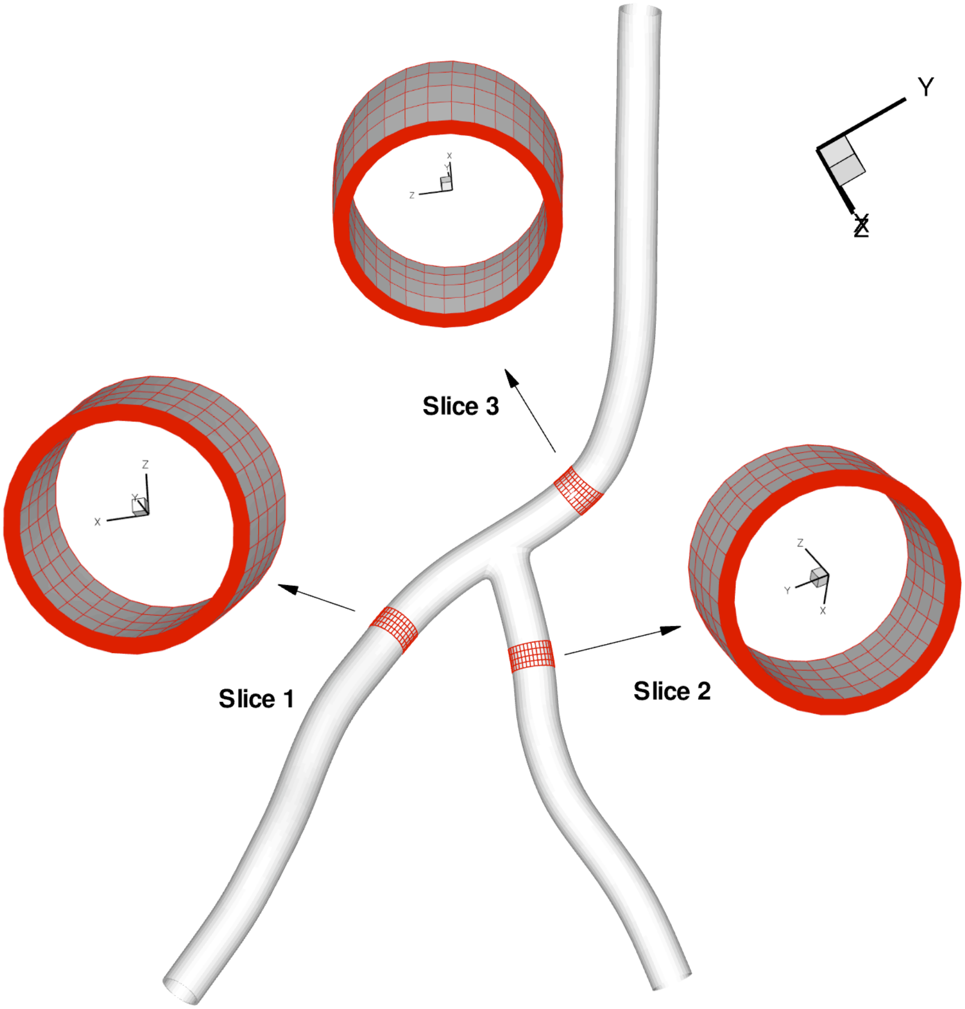

Figure 6.6: Schematic of the patient-specific coronary artery model under normal condition, showing the location and orientation of the slices 1, 2 and 3 under consideration.

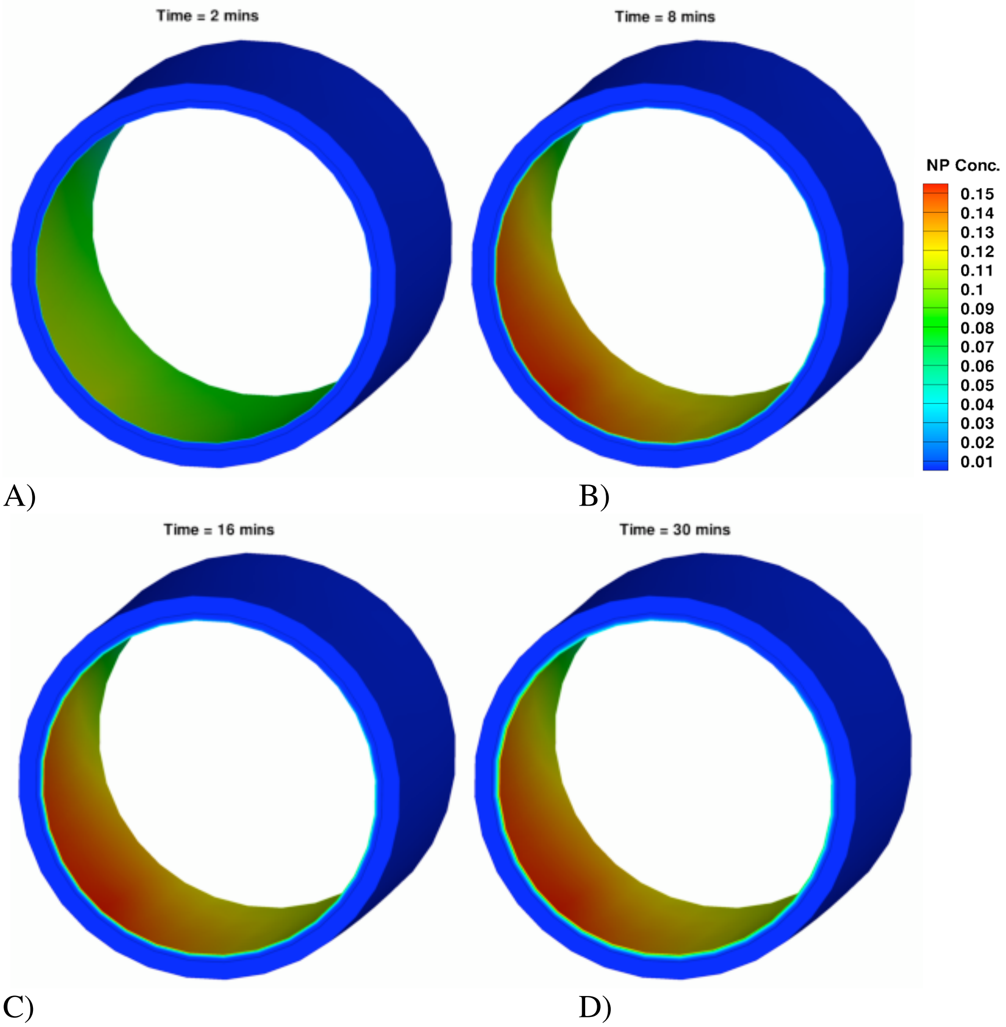

Figure 6.7: Distribution of nanoparticles at slice 1 of the patient-specific coronary artery wall segment under normal condition at A) t = 2 mins, B) t = 8 mins, C) t = 16 mins, D) t = 30 mins in terms of concentration (normalized).

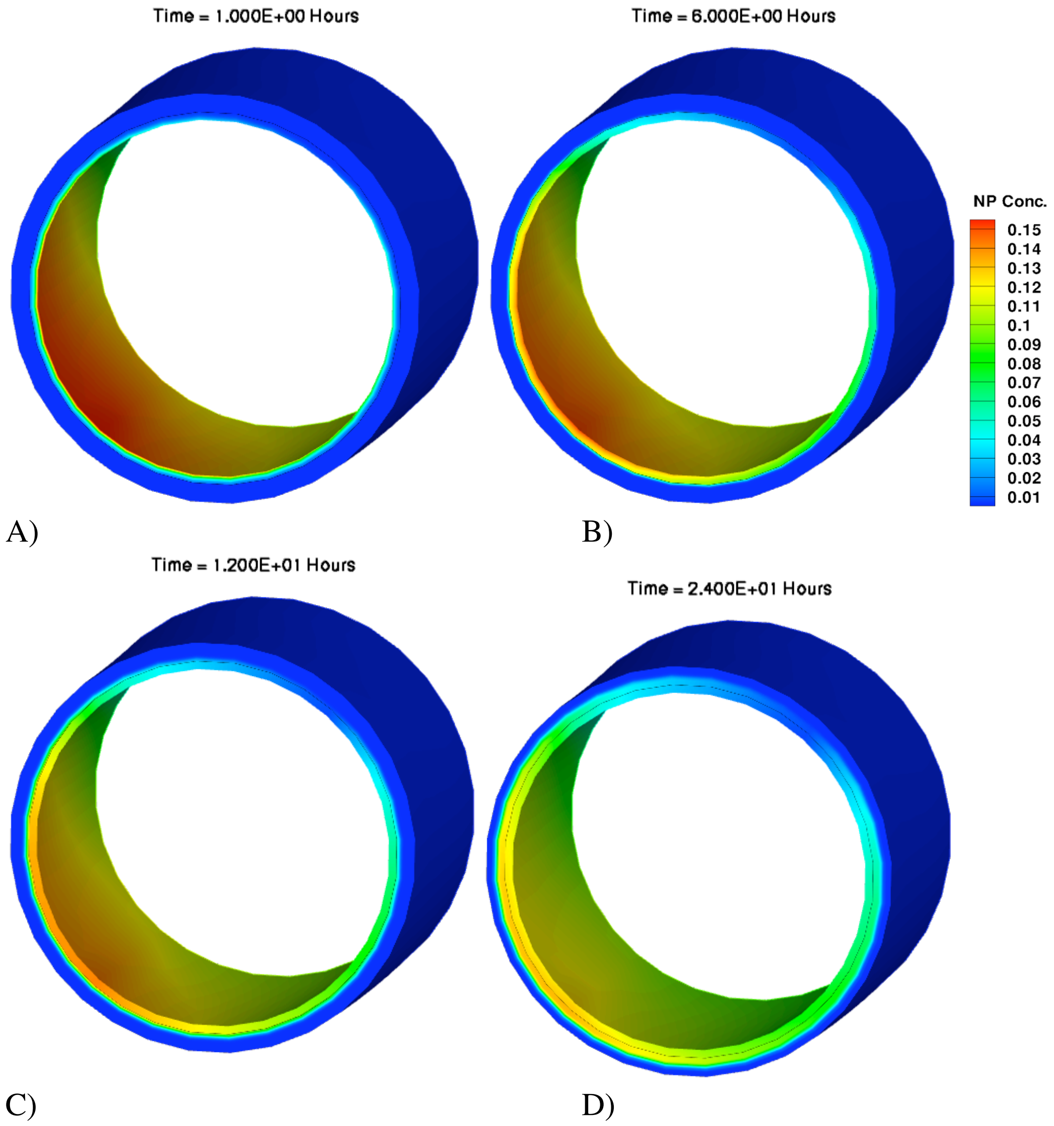

Figure 6.8a: Distribution of nanoparticles at slice 1 of the patient-specific coronary artery wall segment under normal condition at A) t = 2 mins, B) t = 1 hr, C) t = 6 hrs, and D) t = 12 hrs in terms of concentration (normalized).

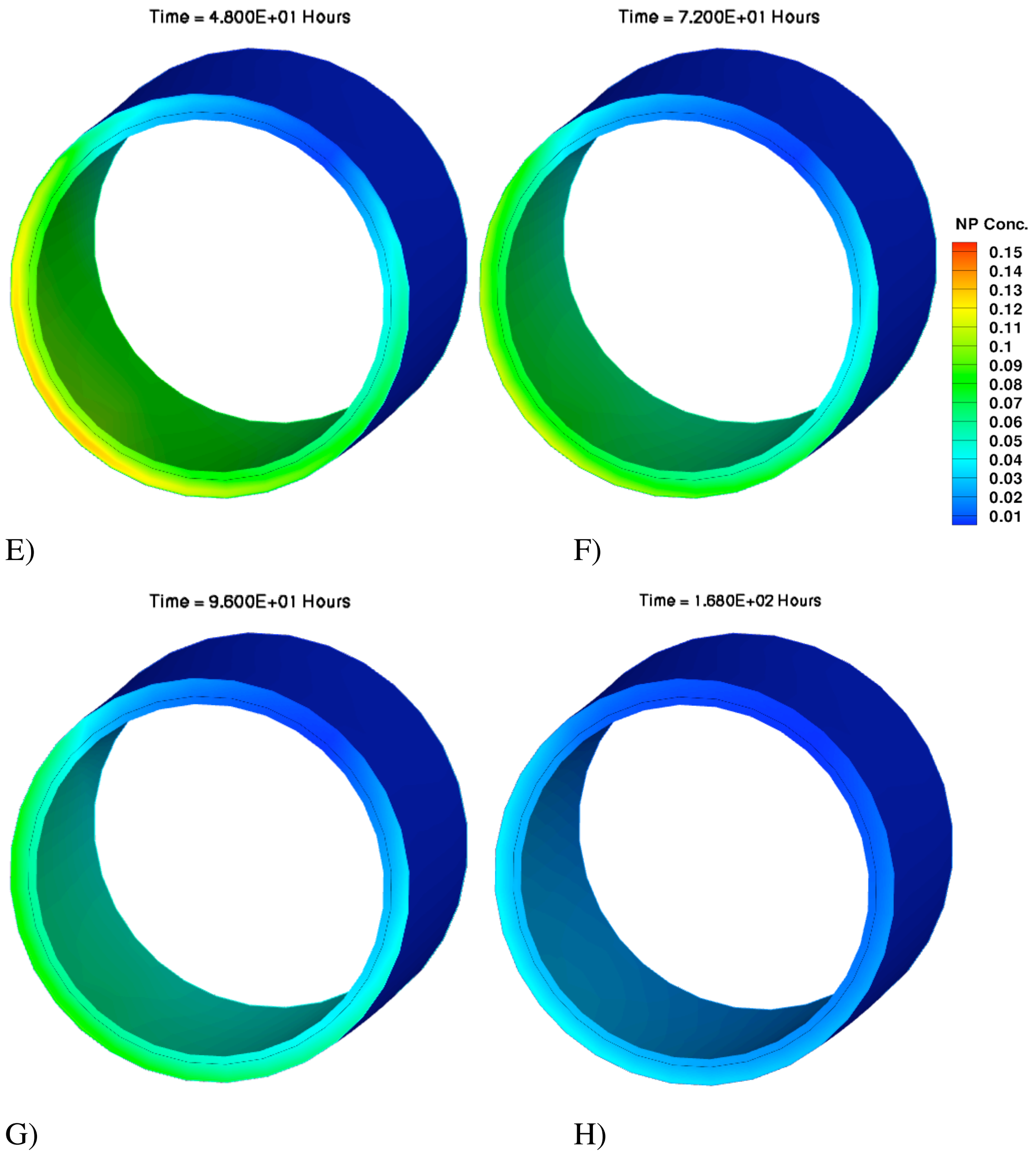

Figure 6.8b: Distribution of nanoparticles at slice 1 of the patient-specific coronary artery wall segment under normal condition at E) *t* = 1 day, F) *t* = 2 days, G) *t* = 4 days, and H) *t* = 7 days in terms of concentration (normalized).

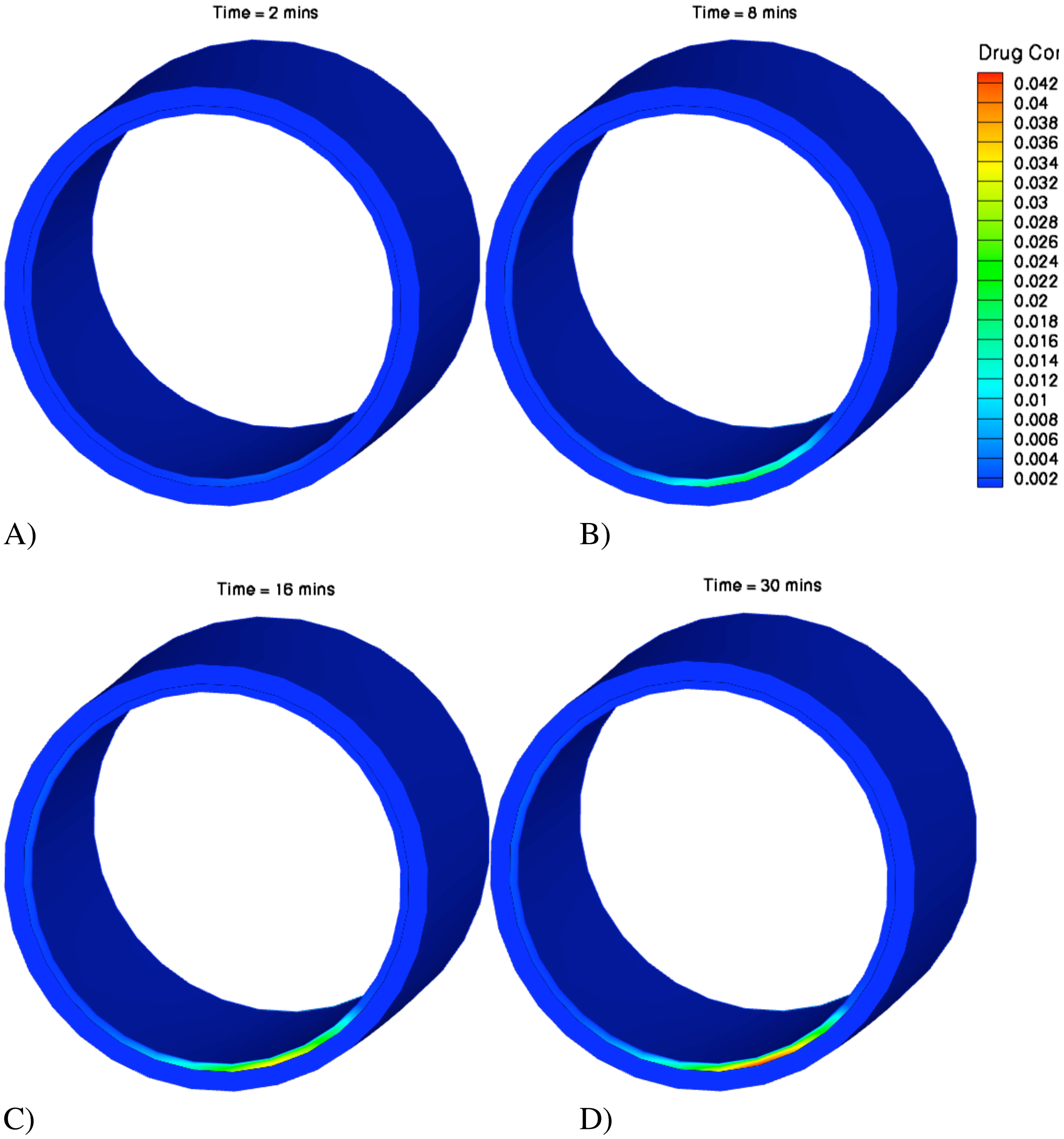

A) B) C) D)

Figure 6.9: Drug distribution at slice 1 of the patient-specific coronary artery wall segment under normal condition at A) *t* = 2 mins, B) *t* = 8 mins, C) *t* = 16 mins, D) *t* = 30 mins, in terms of concentration (normalized).

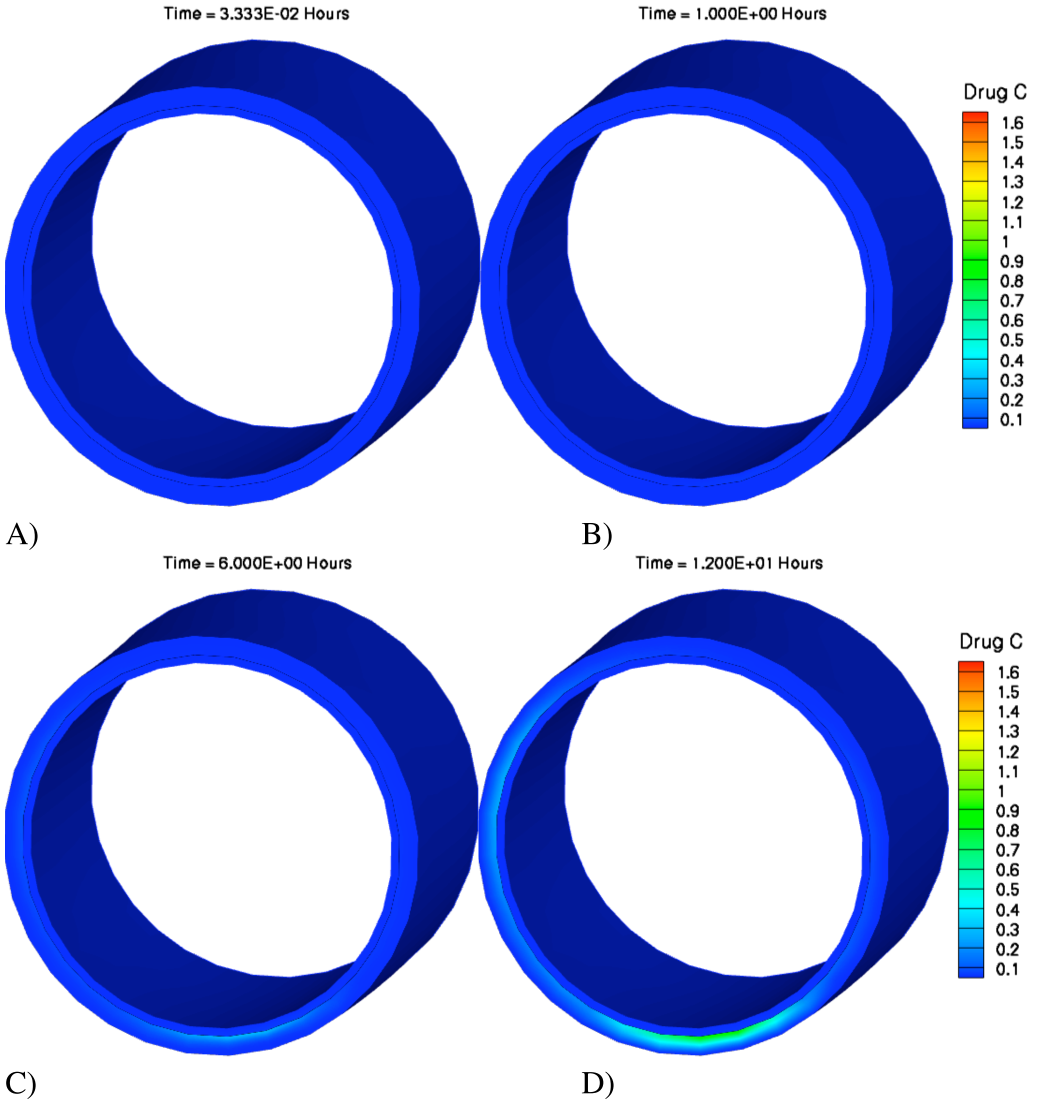

Figure 6.10a: Drug distribution at slice 1 of the patient-specific coronary artery wall segment under normal condition at A) $t = 2$ mins, B) $t = 1$ hr, C) $t = 6$ hrs, and D) $t = 12$ hrs in terms of concentration (normalized).

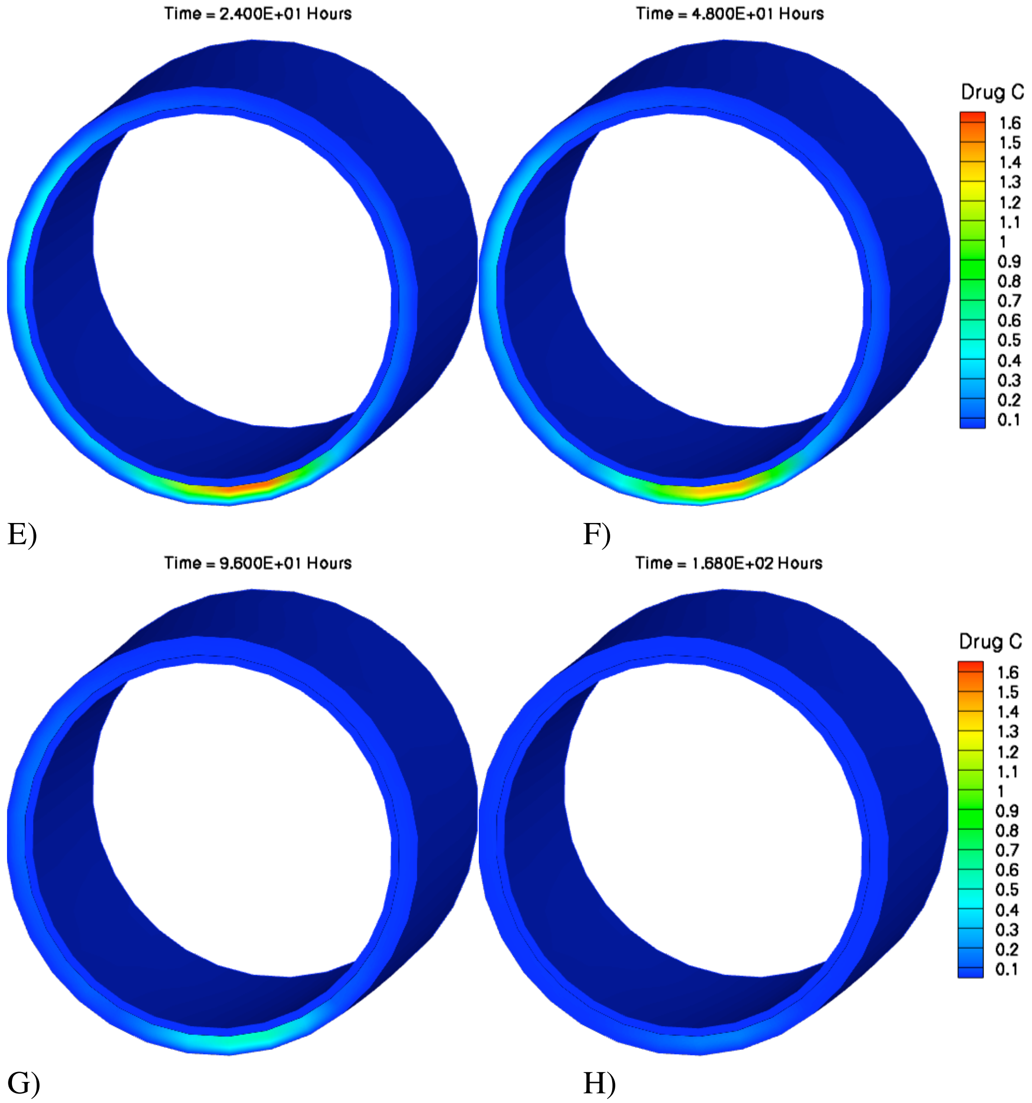

Figure 6.10b: Drug distribution in terms of concentration (normalized) at slice 1 of the patient-specific coronary artery wall segment under normal condition at E) *t* = 1 day, F) *t* = 2 days, G) *t* = 4 days, and H) *t* = 7 days.

6.2 DRUG DISTRIBUTION IN A DISEASED ARTERY WALL WITH A VULNERABLE PLAQUE

The diseased artery model contains a vulnerable plaque characterized by a large lipid core and a thin fibrous cap, placed in its circumflex branch that is roughly 100 mm in length. Vulnerable plaques are more likely to occur close to the bifurcation area, which is a recirculation region for blood flow. According to a study of ruptured plaques by Jerzy et al. using IVUS in 160 patients, 88% of plaques are located within 30 mm of the LAD origin when the average lengths of these LADs are within 48±24.8 mm [78]. Based on these observations, the idealized vulnerable plaque model was positioned near the branching site. Plaque length can be anywhere from 2.0 mm to 50 mm with an average of 26.4 mm [79]. The plaque was chosen to be larger than average, approximately 40 mm in length. The peak wall thickness (excluding the adventitia) within the plaque is approximately 1.1 mm, which agrees with the data in Table 4.1. It can be reiterated here that plaque features and dimensions vary over a wide range of values depending on the extent of disease and the individual patient. This idealized model is just a representative case devised to demonstrate the capabilities of the computational toolset developed. The details of this model can be found in Figures 6.11 and 6.12.

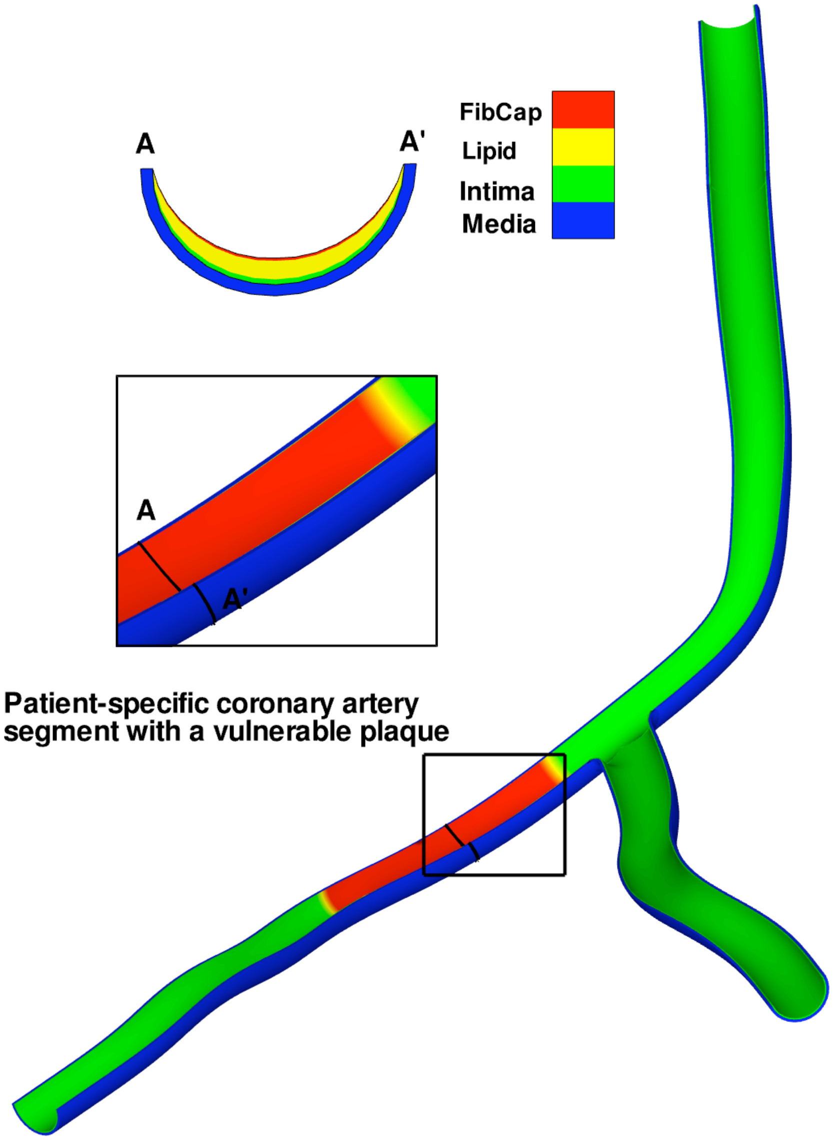

Figure 6.11: A cut-away view of the diseased patient-specific left coronary artery segment with an idealized vulnerable plaque placed in the circumflex branch of the LCA. The media is in blue, the intima in green, the lipid core in yellow and the thin fibrous cap in red. A cross-section is taken along A-A’ midway through the vulnerable plaque highlighting the thickening of the intima and lipid accumulation.

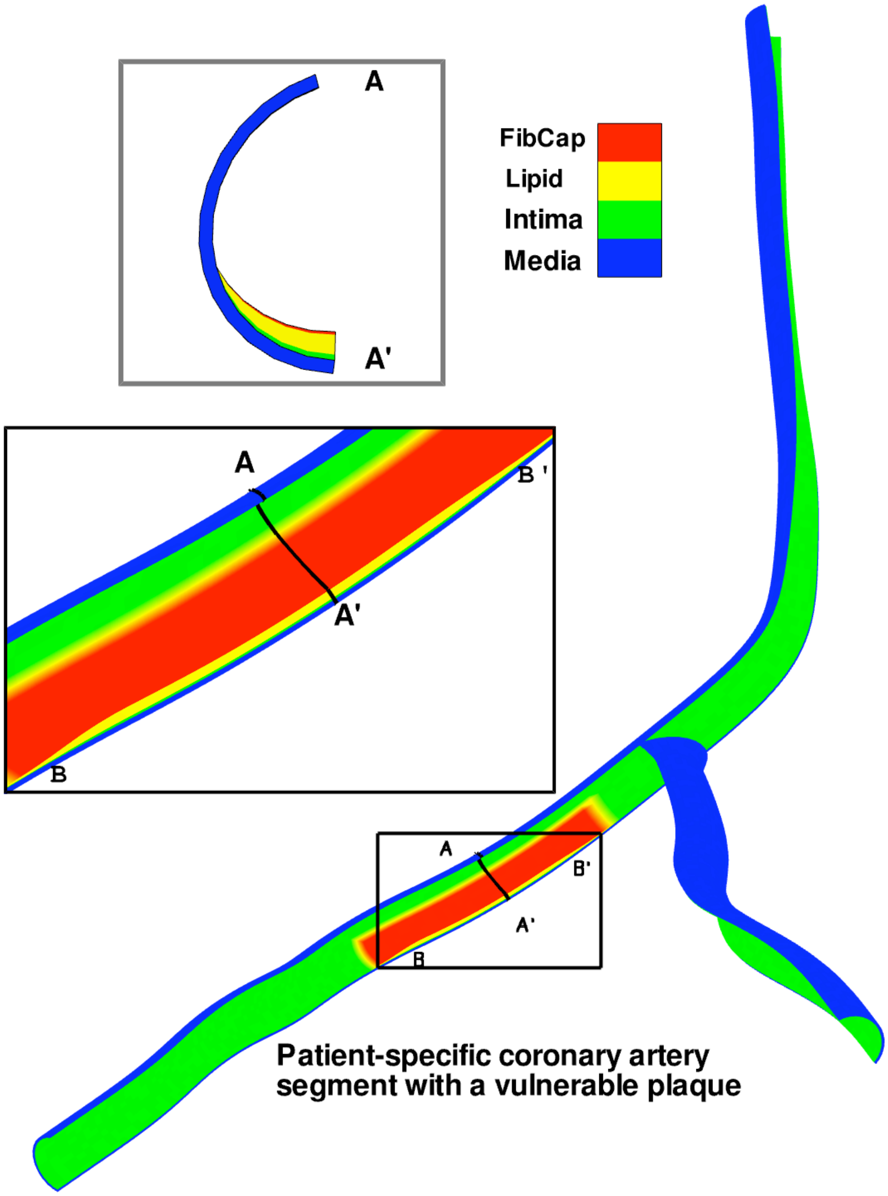

Figure 6.12: A cut-away view of the diseased patient-specific left coronary artery segment with an idealized vulnerable plaque placed in the circumflex branch. The media is in blue, the intima in green, the lipid core in yellow and the thin fibrous cap in red. A transverse cross-section is taken along A-A’ midway through the vulnerable plaque highlighting the thickening of the intima and lipid accumulation.

In Figure 6.13, the location of the three representative transverse slices are presented with slice 1 taken right through the middle of the vulnerable plaque located at the circumflex branch of the LCA. Again, due to the closely coupled nature of transport between the drug and the nanoparticles, the effect of plaque heterogeneity on drug distribution can be better studied by considering the time evolution of their distributions together.

Because of non-uniform wall deposition of nanoparticles (unlike the idealized case), a deeper penetration of nanoparticles with a higher concentration level at or around the nanoparticle rich wall deposition area was detected. Fortunately, the plaque location selected coincides with this dense wall deposition site, hence ensuring drug availability to the target region. This may not be the case in general. But for the purpose of analysis, this provides an excellent opportunity to investigate local transport behavior at the target area when the nanoparticles actually marginate preferentially toward the diseased site.

From Figure 6.14 it appears that the nanoparticle transport behavior mimics the corresponding idealized case, that is, slow accumulation and entrapment of nanoparticles within the lipid core. This observation is further reinforced by the way the nanoparticles gradually seep into the diseased part from the surrounding areas, albeit to a lesser extent due to somewhat reduced nanoparticle availability in the neighboring healthy part of the artery. The latter is a direct consequence of spatial variation of nanoparticle wall deposition.

The nanoparticle concentration in the lipid pool peaks within 24 hours of its administration. This is highly beneficial from an efficiency perspective because this appears to coincide with the initial burst of drug release (see Figure 4.5). During the first 24 hours drug release rate is steepest by design and close to 30% percent of the drug becomes available for retention within the lipid core to exert therapeutic effect. Beyond this time, the release rate profile flattens out and the role of nanoparticles as a source of drug diminishes.

The drug distribution pattern (see Figure 6.15) essentially follows that of the nanoparticles. This is particularly true at early times. However, later on, as the nanoparticles overcome the IEL barrier seemingly effortlessly, and then eventually clear out through the adventitia and the lumen, the drug remains largely confined within the intima. That is, even though the drug is able to overcome the lipid core barrier, when it reaches the outer intima, a region of fast planar diffusion, the drug gets depleted through the healthy part of the artery into the lumen. Consequently, it appears that the concentration gradient across the IEL on the lipid core side does not become steep enough for the drug to diffuse through the IEL barrier, which leads to its entrapment within the lipid core.

Figure 6.16 and Figure 6.17 illustrate the spatial distribution of the nanoparticles and the drug at slice 2, respectively, at various times. Comparing with Figure 6.9 and Figure 6.10 for the corresponding distributions at slice 1 of the healthy patient-specific artery case, it appears that both species exhibit similar transport characteristics and pattern of distribution. The difference lies in the range of concentration, which can be attributed to the variation in nanoparticle wall deposition at these two different slice locations.

A side-by-side comparison of the drug distribution for the healthy and diseased cases (see Figure 6.18) at slice 2 of the neighboring branch (that is, the LAD) reveals that although the time evolution of distribution pattern is essentially the same, the healthy branch of the diseased patient-specific artery retains a lower concentration of drug compared to its non-diseased counterpart. This implies that the lipid core in the vulnerable plaque attracts and accumulates the hydrophobic drug from its neighboring healthy branches facilitated by rapid planar diffusion.

The nanoparticle and drug distribution at various times for slice 3, located upstream of the branch with the vulnerable plaque, can be found in Figure 6.19 and Figure 6.20, respectively. Quite expectedly, the distributions demonstrate similar trends to those at slice 2. However, drug concentration is lower at this location due to the spatial variation of nanoparticle wall deposition.

Finally, Figure 6.21 depicts the time evolution of nanoparticle and drug distributions side-by-side at a slice taken at 1/3 depth (radially) from the lumen side of the patient-specific coronary artery wall segment. These pictures highlight the points made above more clearly. For example, they illustrate how the hydrophobic drug travels from the healthy parts facilitated by the faster planar diffusion and gets trapped within the lipid core of the vulnerable plaque. The 3D nature of drug distribution is quite obvious here.

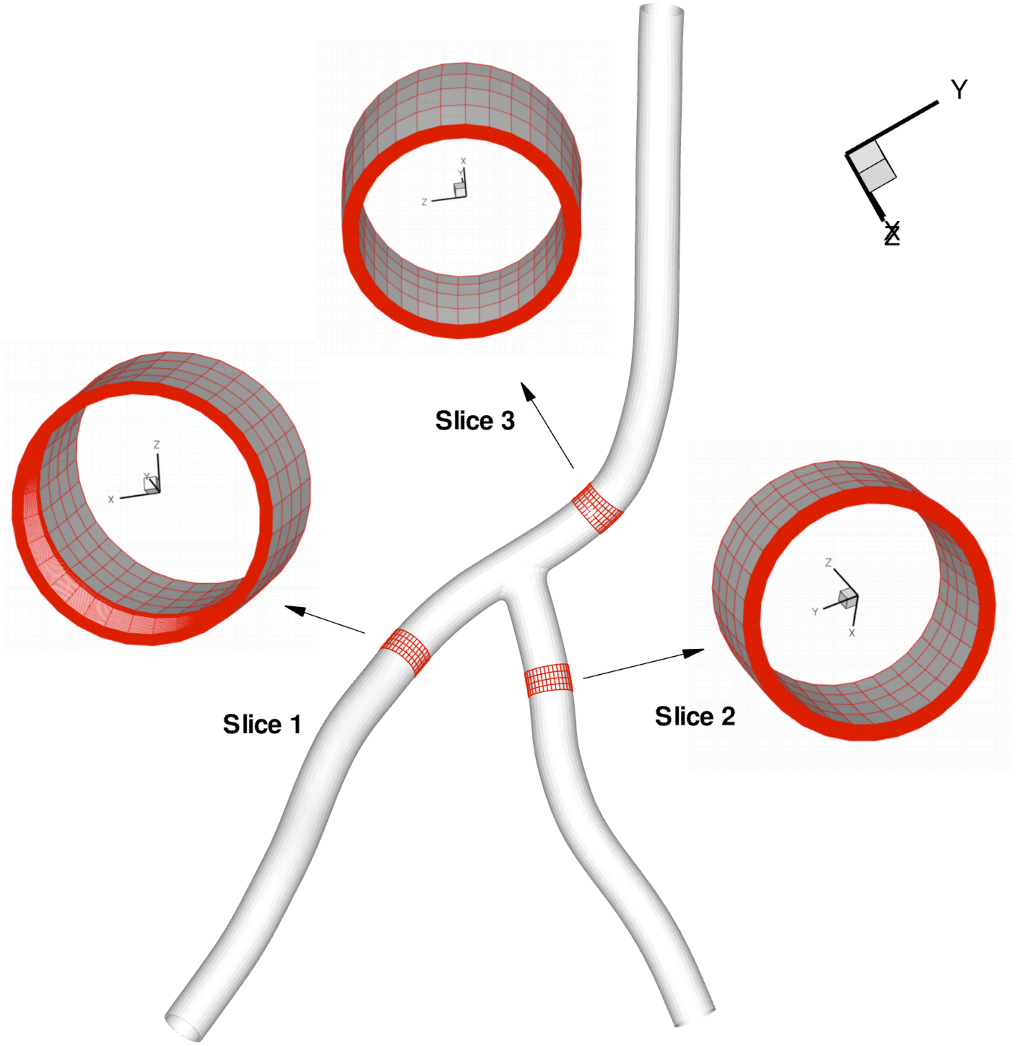

Figure 6.13: Schematic of the patient-specific coronary artery model under diseased condition characterized by a vulnerable plaque depicting the location and orientation of the slices 1, 2 and 3 under consideration. Here slice 1 is taken approximately halfway through the length of the plaque.

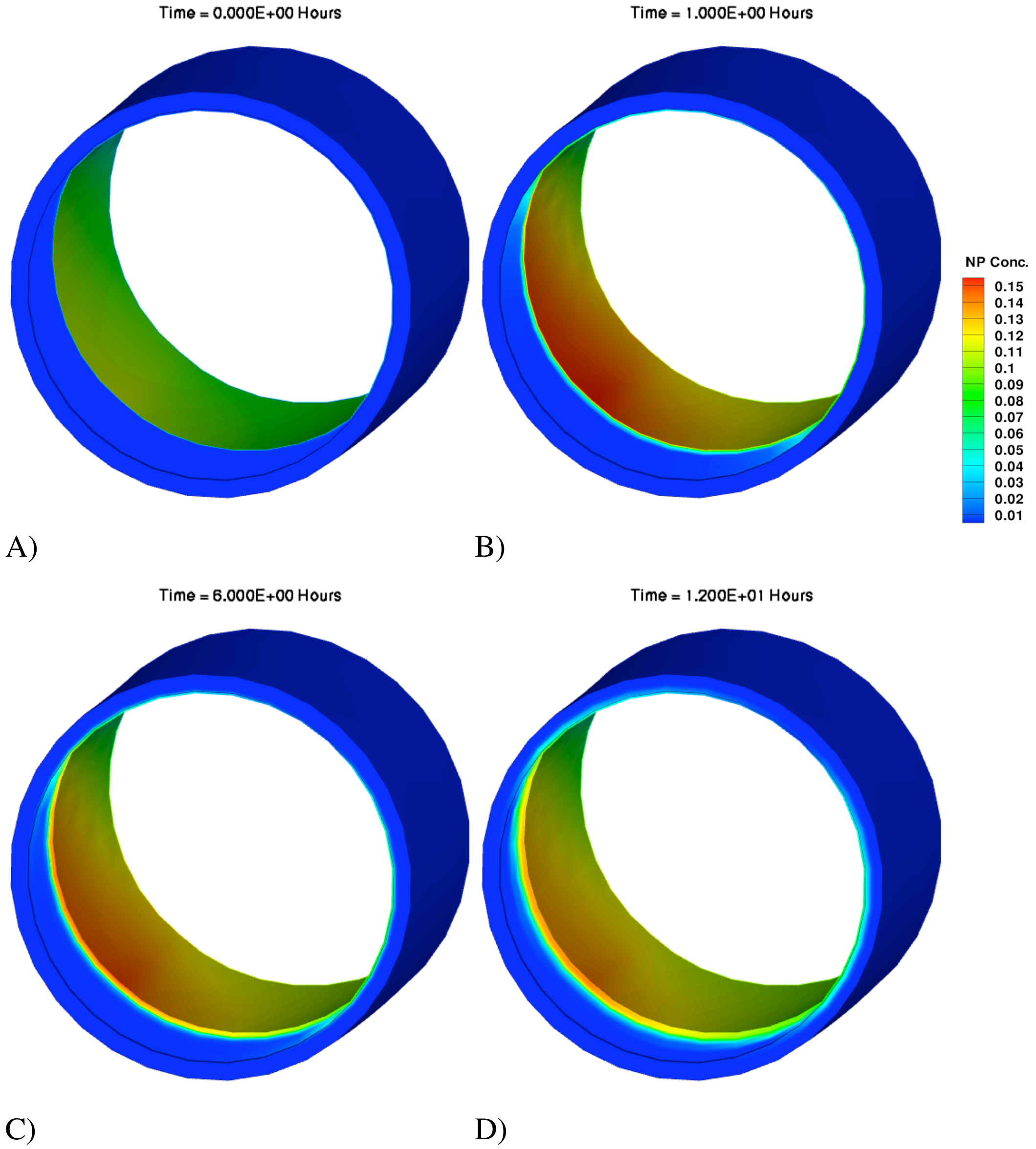

Figure 6.14a: Distribution of nanoparticles at slice 1 of the patient-specific coronary artery wall segment under diseased condition characterized by a vulnerable plaque at A) $t = 2$ mins, B) $t = 1$ hr, C) $t = 6$ hrs, and D) $t = 12$ hrs in terms of concentration (normalized).

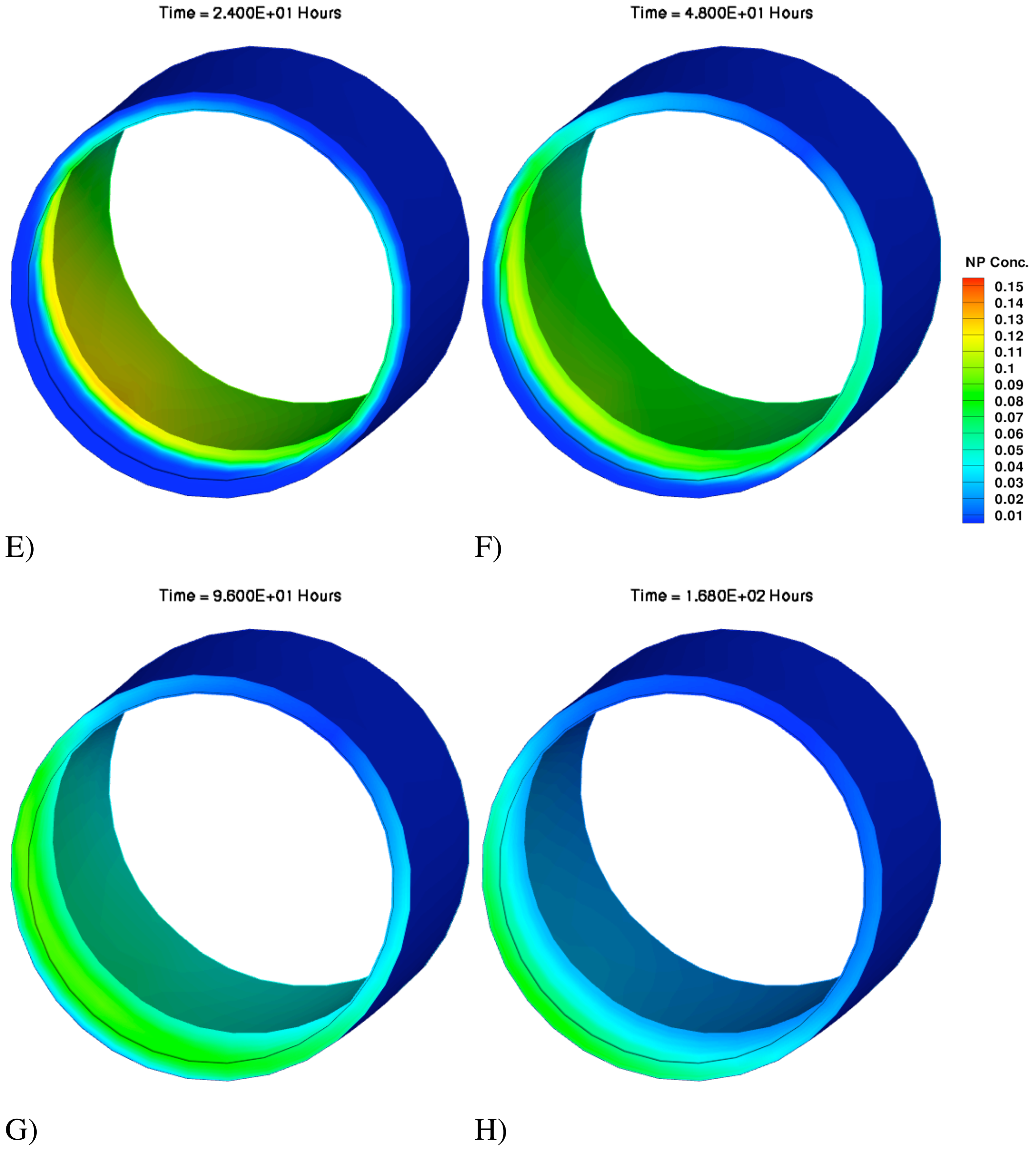

Figure 6.14b: Distribution of nanoparticles at slice 1 of the patient-specific coronary artery wall segment under diseased condition characterized by a vulnerable plaque at E) t = 1 day, F) t = 2 days, G) t = 4 days, and H) t = 7 days in terms of concentration (normalized).

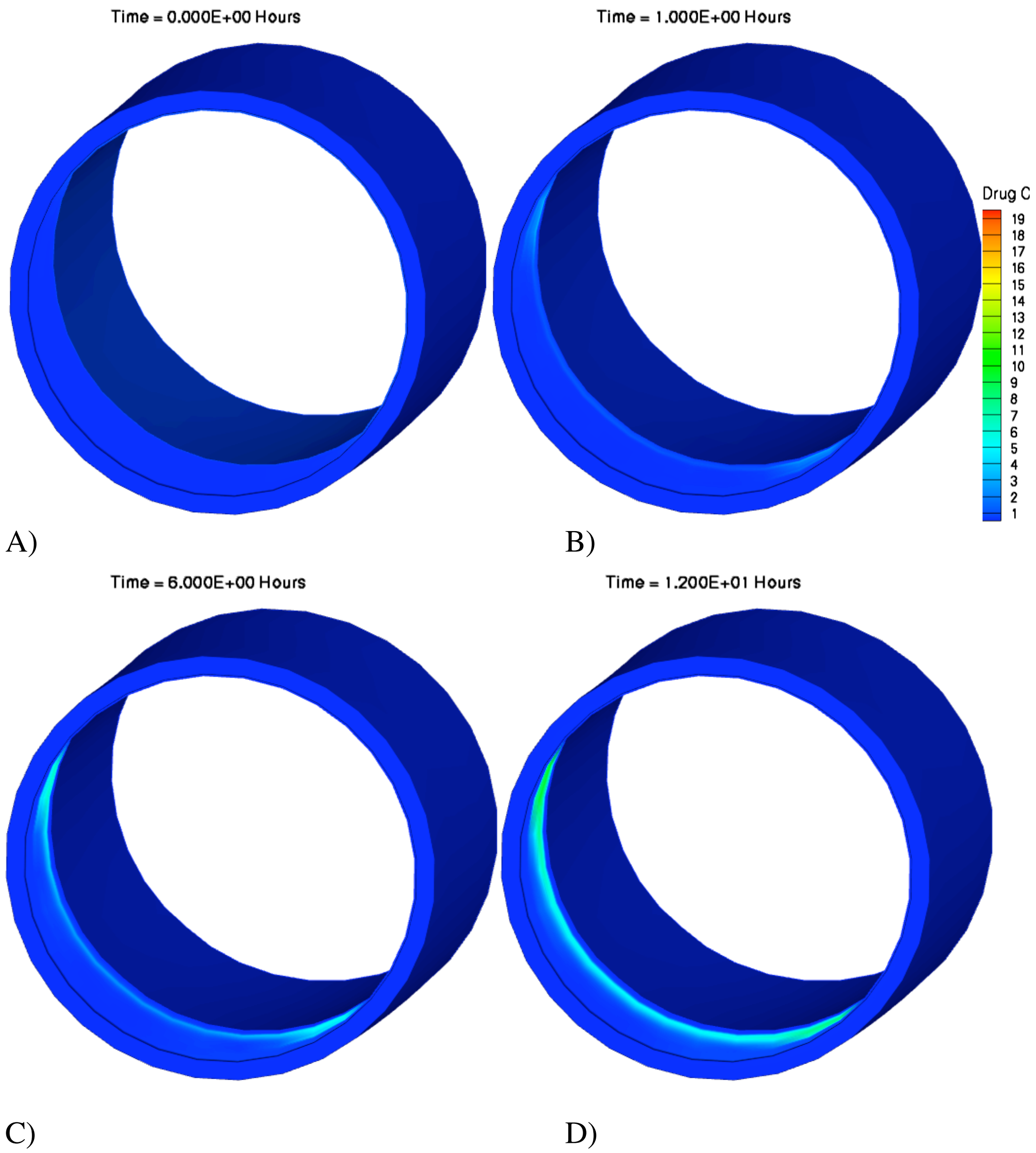

Figure 6.15a: Drug distribution in terms of concentration (normalized) at slice 1 of the patient-specific coronary artery wall segment under diseased condition at A) *t* = 2 mins, B) *t* = 1 hr, C) *t* = 6 hrs, and D) *t* = 12 hrs.

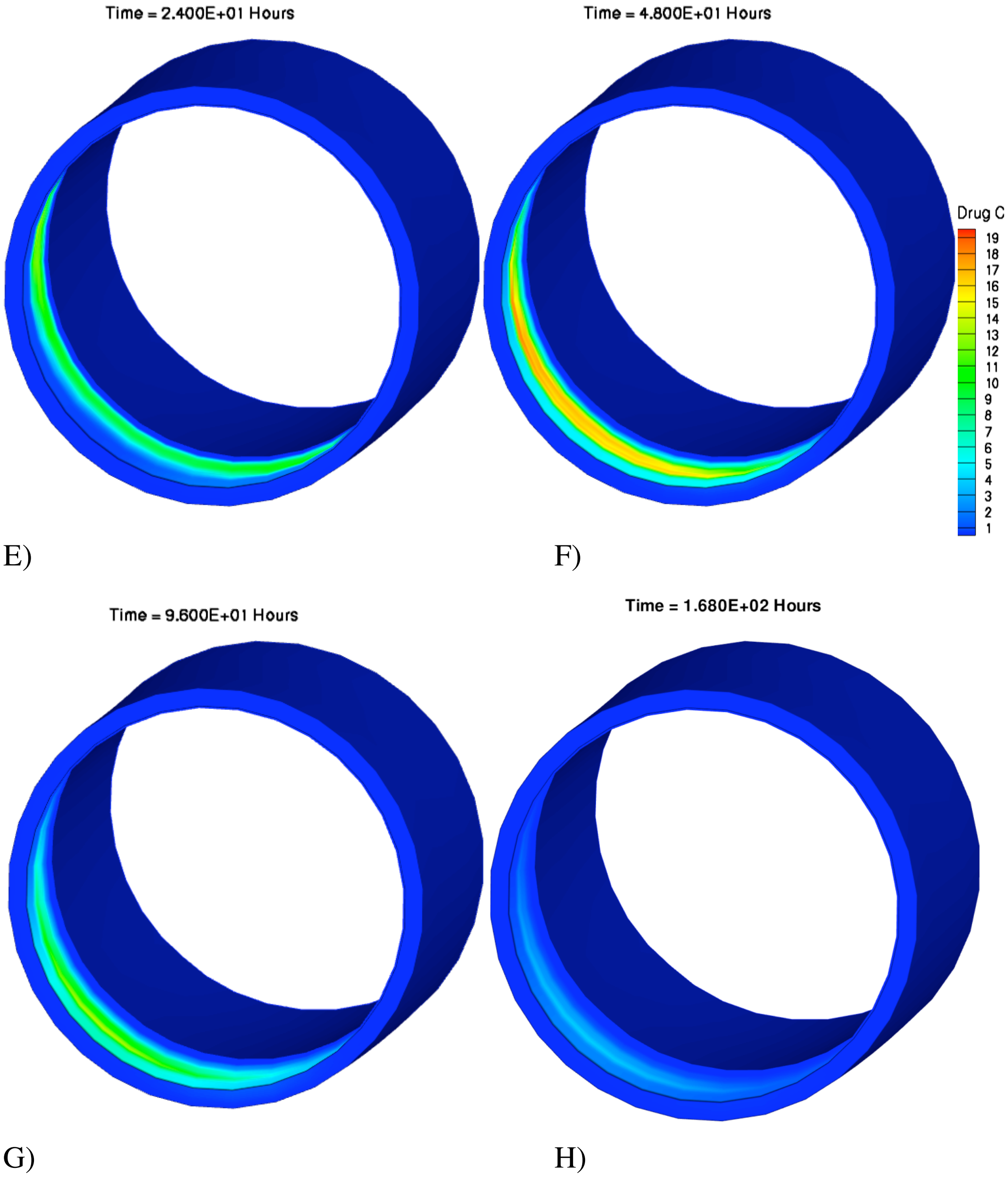

Figure 6.15b: Drug distribution in terms of concentration (normalized) at slice 1 of the patient-specific coronary artery wall segment under diseased condition at E) t = 1 day, F) t = 2 days, G) t = 4 days, and H) t = 7 days.

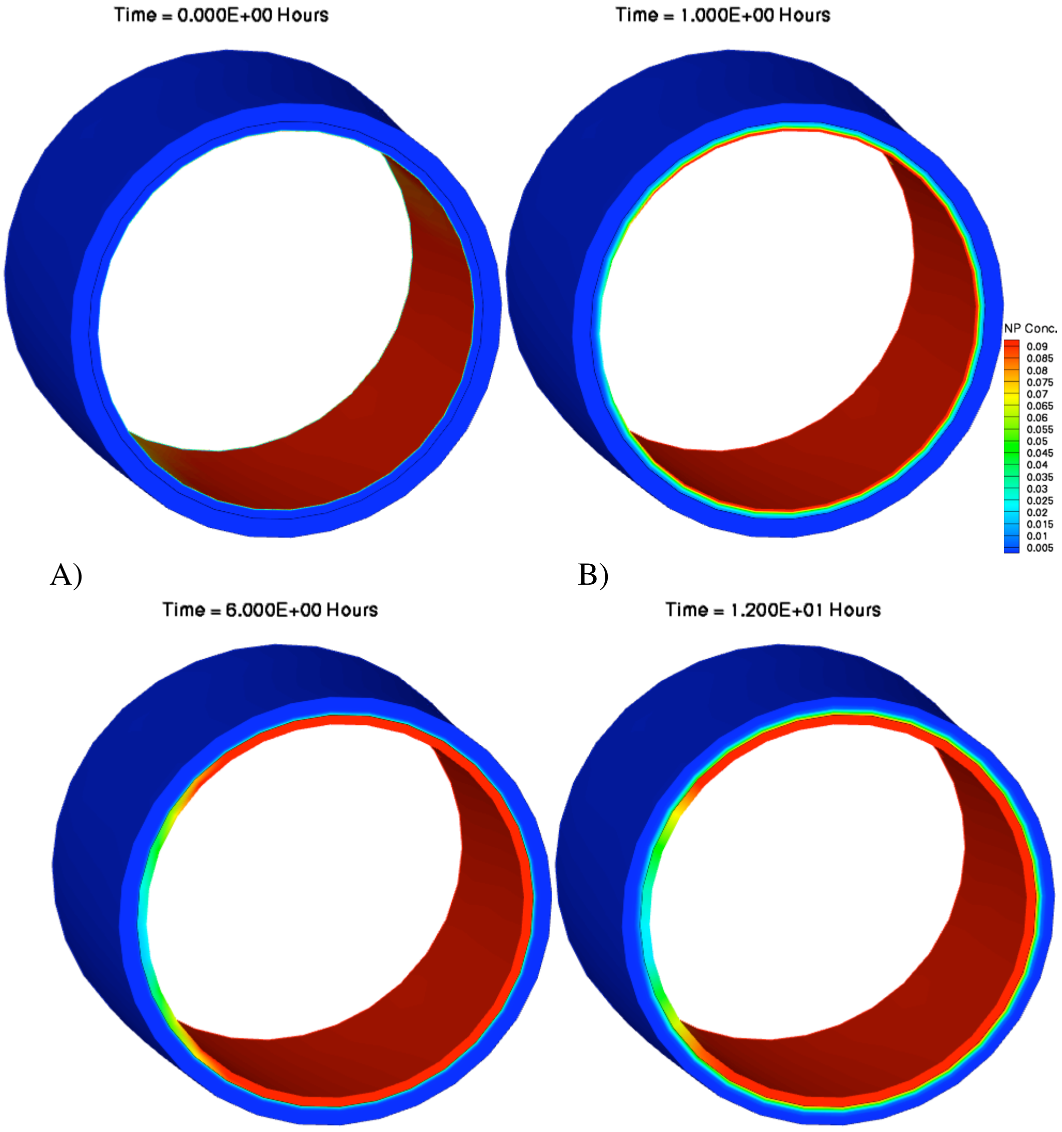

A) B)

C) D)

Figure 6.16a: Distribution of nanoparticles at slice 2 of the patient-specific coronary artery wall segment under diseased condition at times A) *t* = 2 mins, B) *t* = 1 hr C) *t* = 6 hrs, D) *t* = 12 hrs.

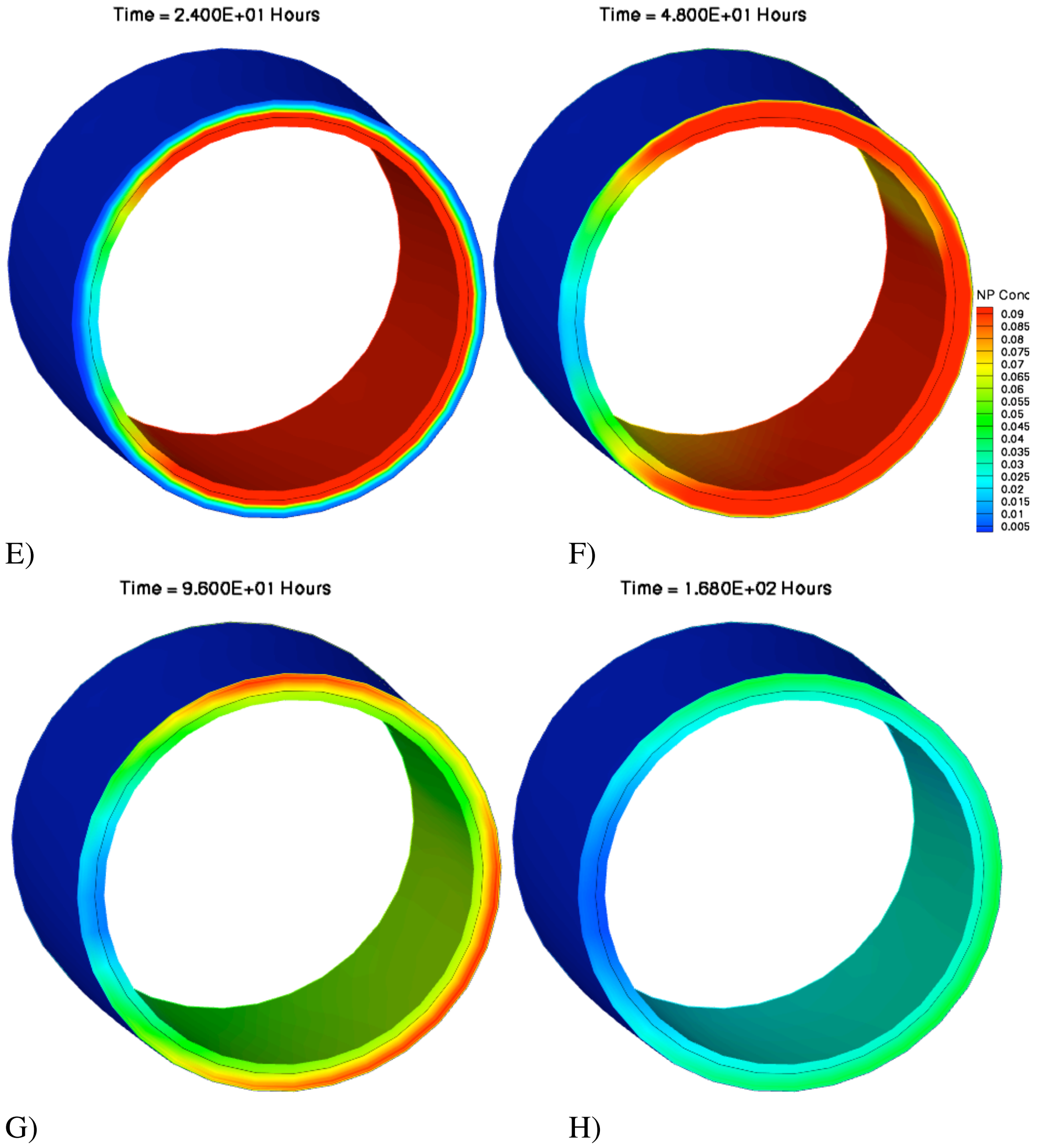

Figure 6.16b: Distribution of nanoparticles in terms of concentration (normalized) at slice 2 of the patient-specific coronary artery wall segment under diseased condition at times at times E) $t = 1$ day, F) $t = 2$ days, G) $t = 4$ days, and H) $t = 7$ days.

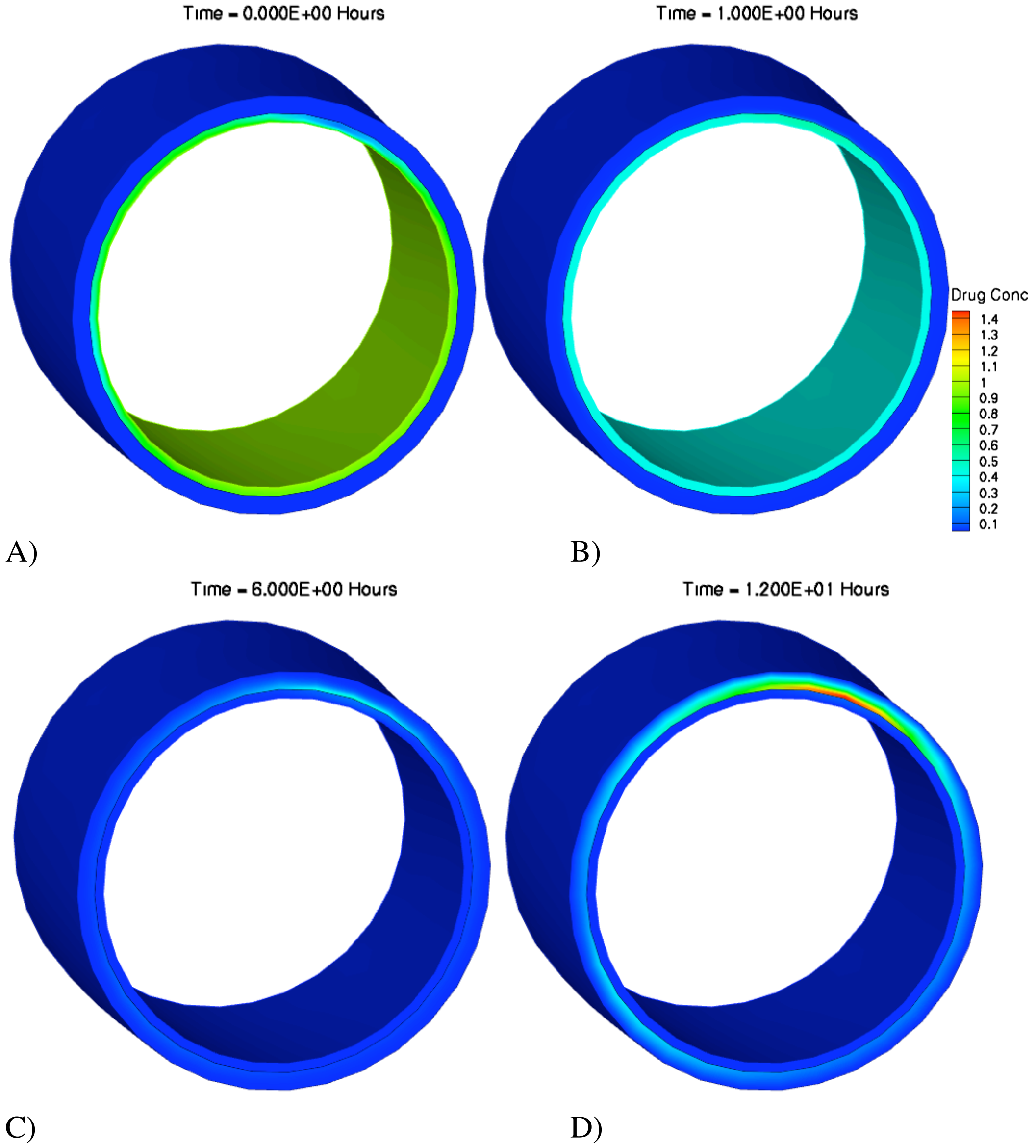

Figure 6.17a: Drug distribution at slice 2 of the patient-specific coronary artery wall segment under diseased condition at times A) t = 2 mins, B) t = 1 hr C) t = 6 hrs, D) t = 12 hrs.

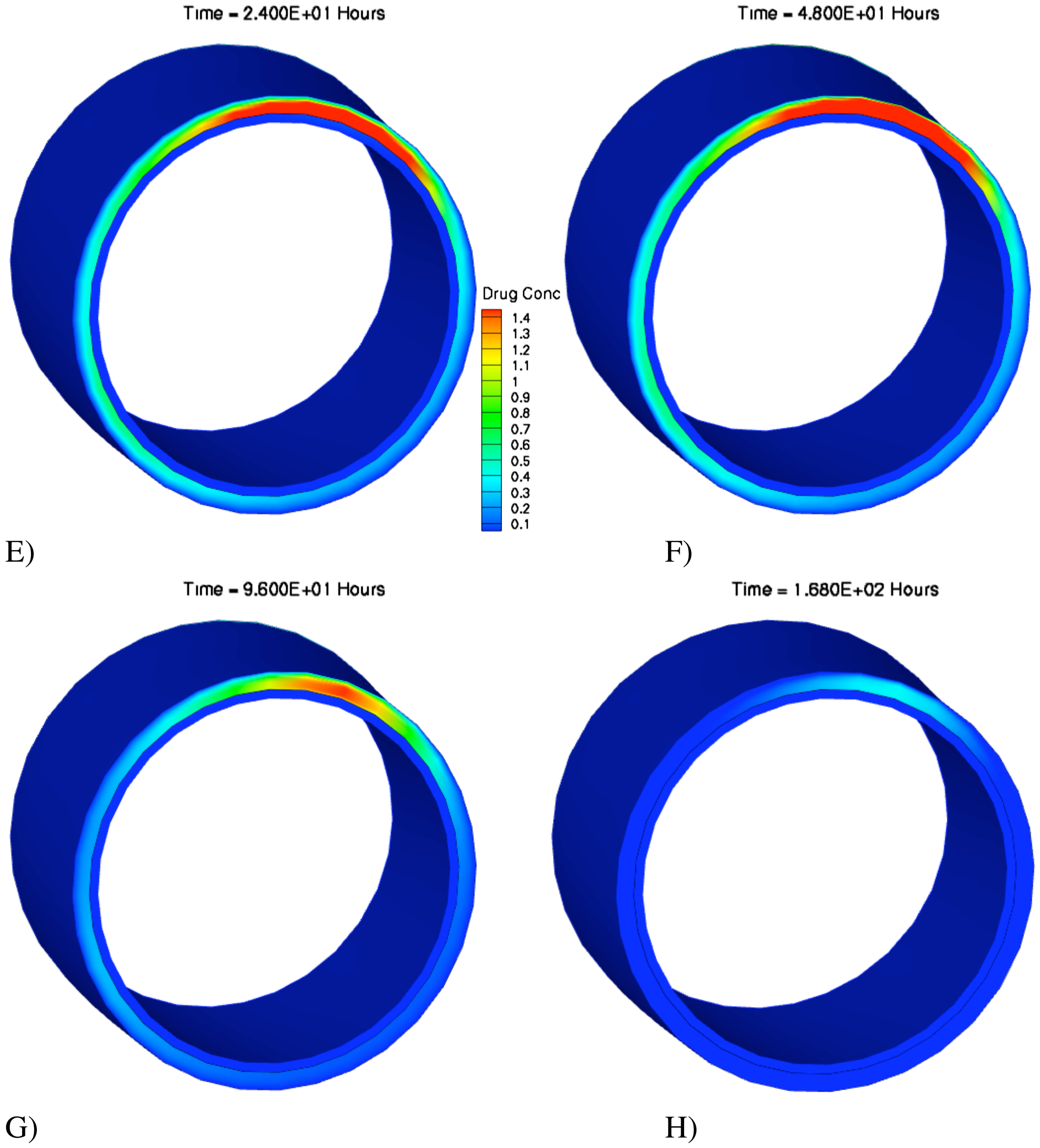

Figure 6.17b: Drug distribution at slice 2 of the patient-specific coronary artery wall segment under diseased condition at times E) $t = 1$ day, F) $t = 2$ days, G) $t = 4$ days, and H) $t = 7$ days.

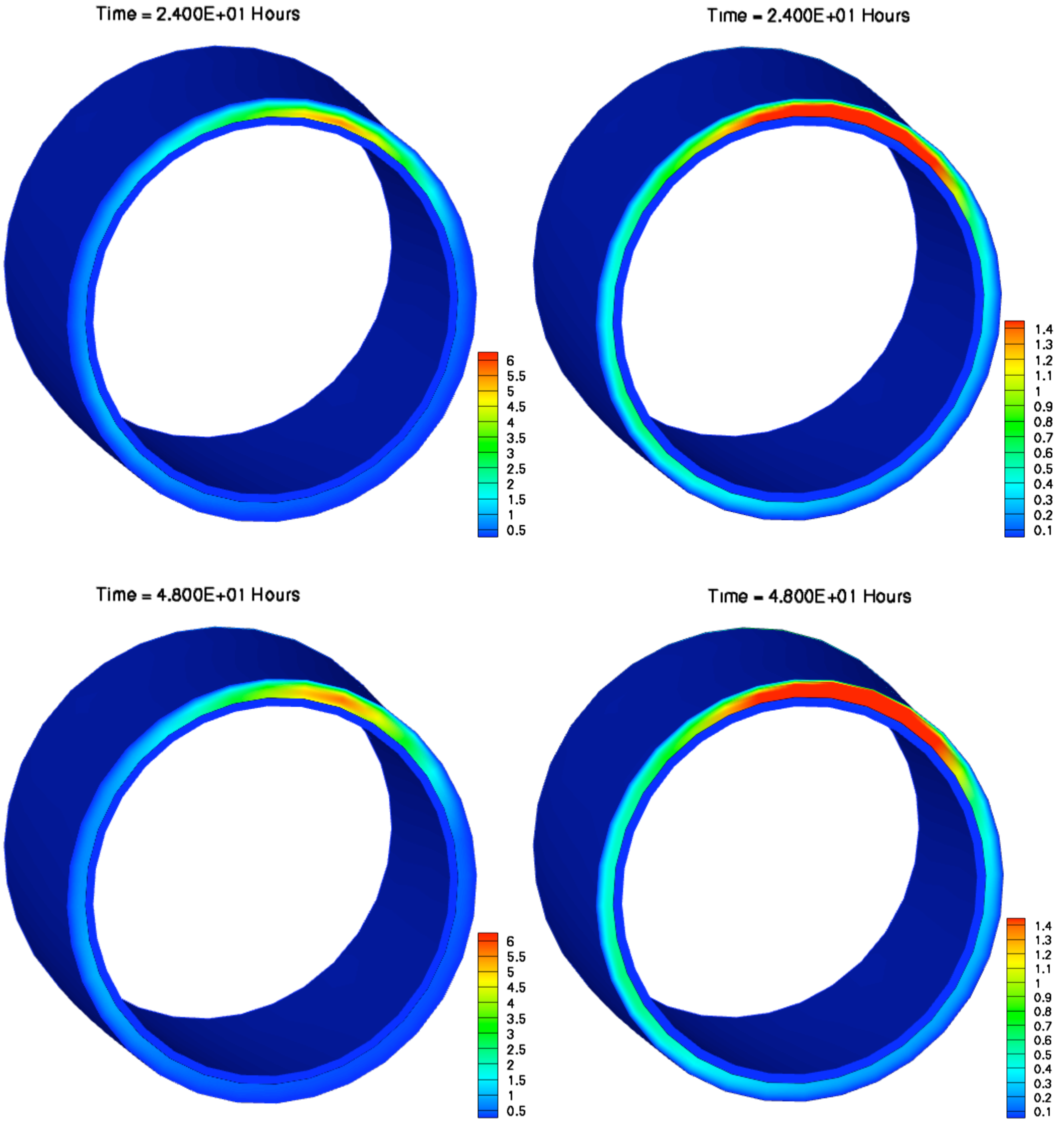

Figure 6.18a: Distribution of drug at slice 2 of the healthy (left) and diseased (right) patient-specific coronary artery wall segment at t = 1 day (top) and t = 2 days (bottom), in terms of concentration (normalized).

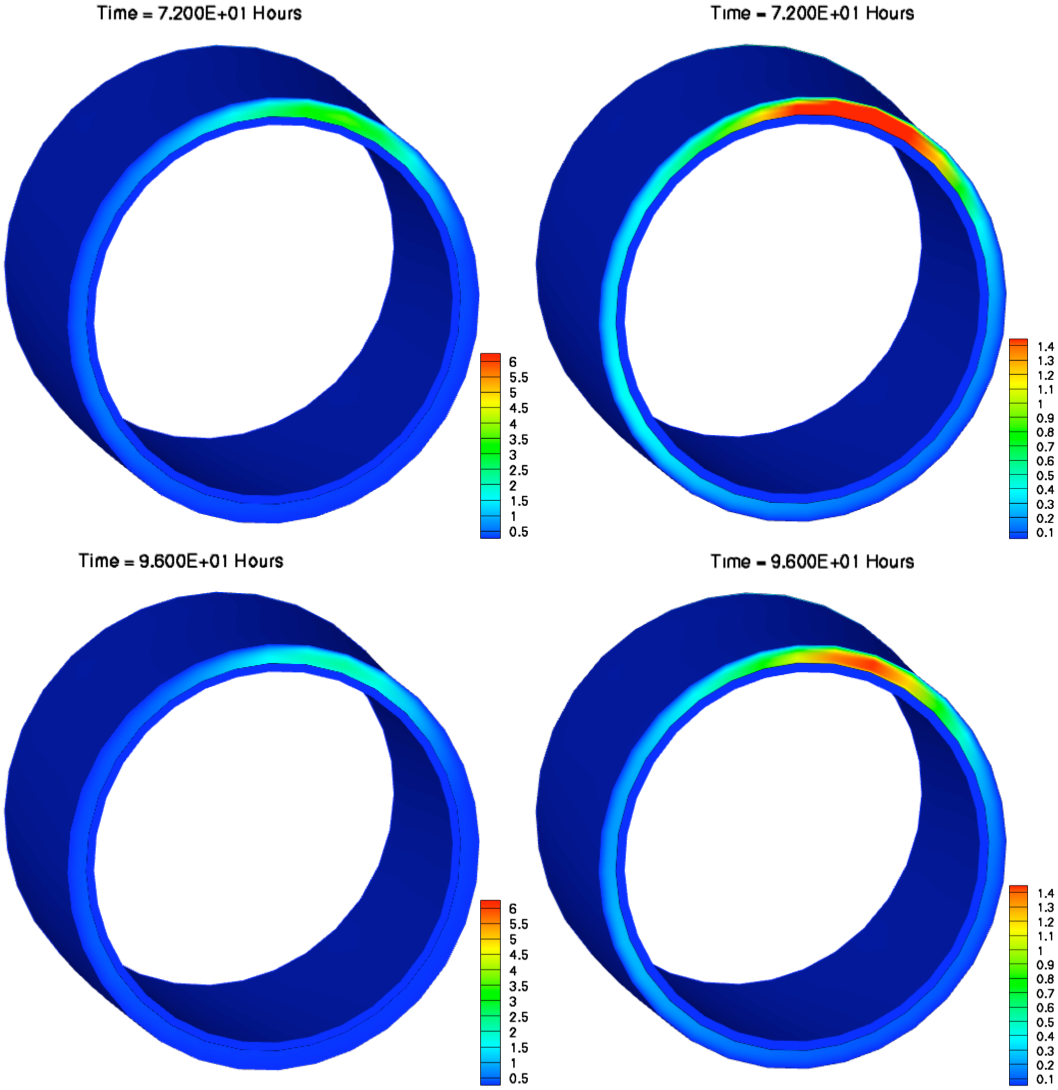

Figure 6.18b: Distribution of drug at slice 2 of the healthy (left) and diseased (right) patient-specific coronary artery wall segment at $t = 3$ days (top) and $t = 4$ days (bottom), in terms of concentration (normalized).

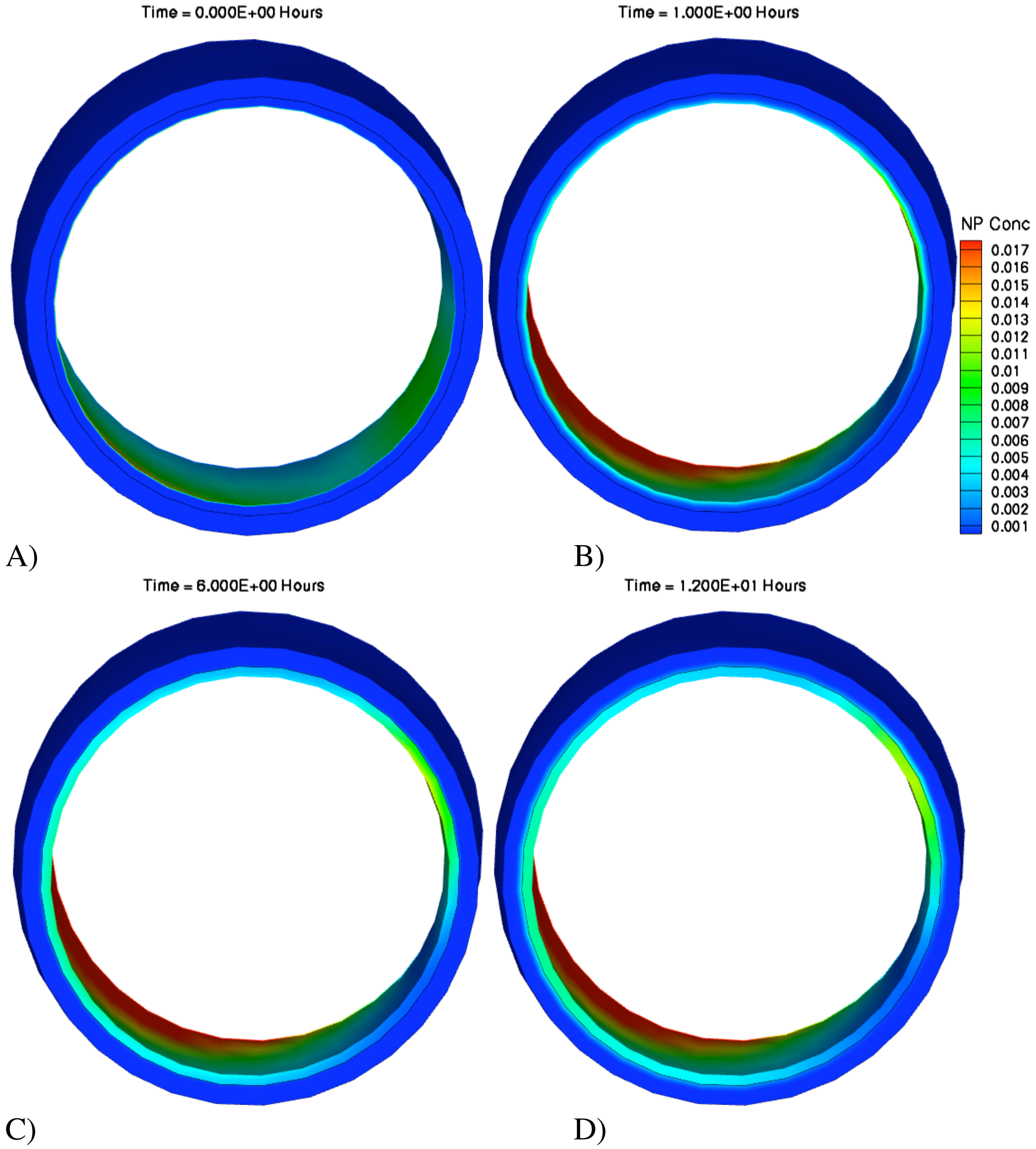

Figure 6.19a: Distribution of nanoparticles in terms of concentration (normalized) at slice 3 of the patient-specific coronary artery wall segment under diseased condition at times A) $t = 2$ mins, B) $t = 1$ hr C) $t = 6$ hrs, D) $t = 12$ hrs.

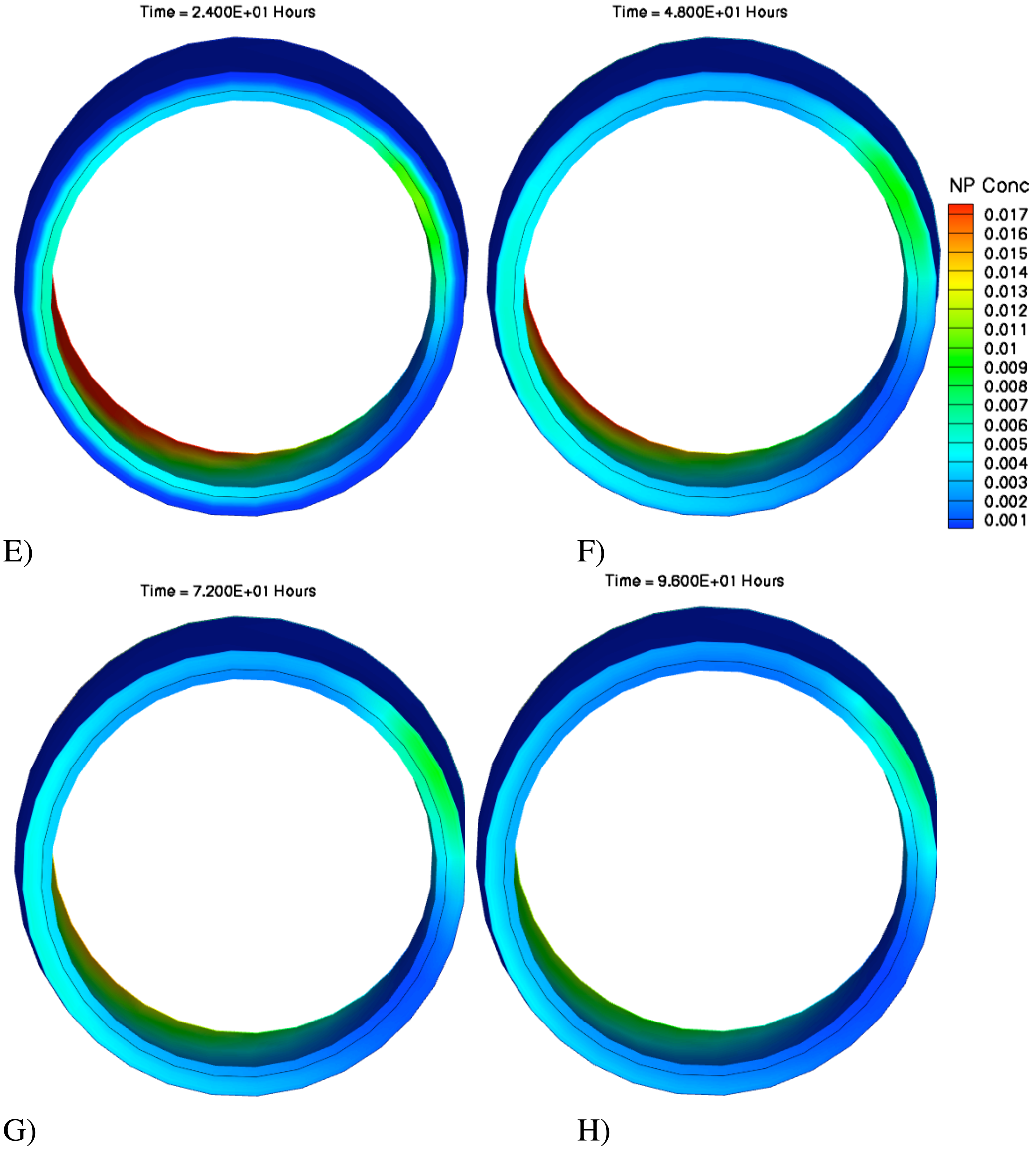

Figure 6.19b: Distribution of nanoparticles in terms of concentration (normalized) at slice 3 of the patient-specific coronary artery wall segment under diseased condition at times E) $t = 1$ day, F) $t = 2$ days, G) $t = 3$ days, and H) $t = 4$ days.

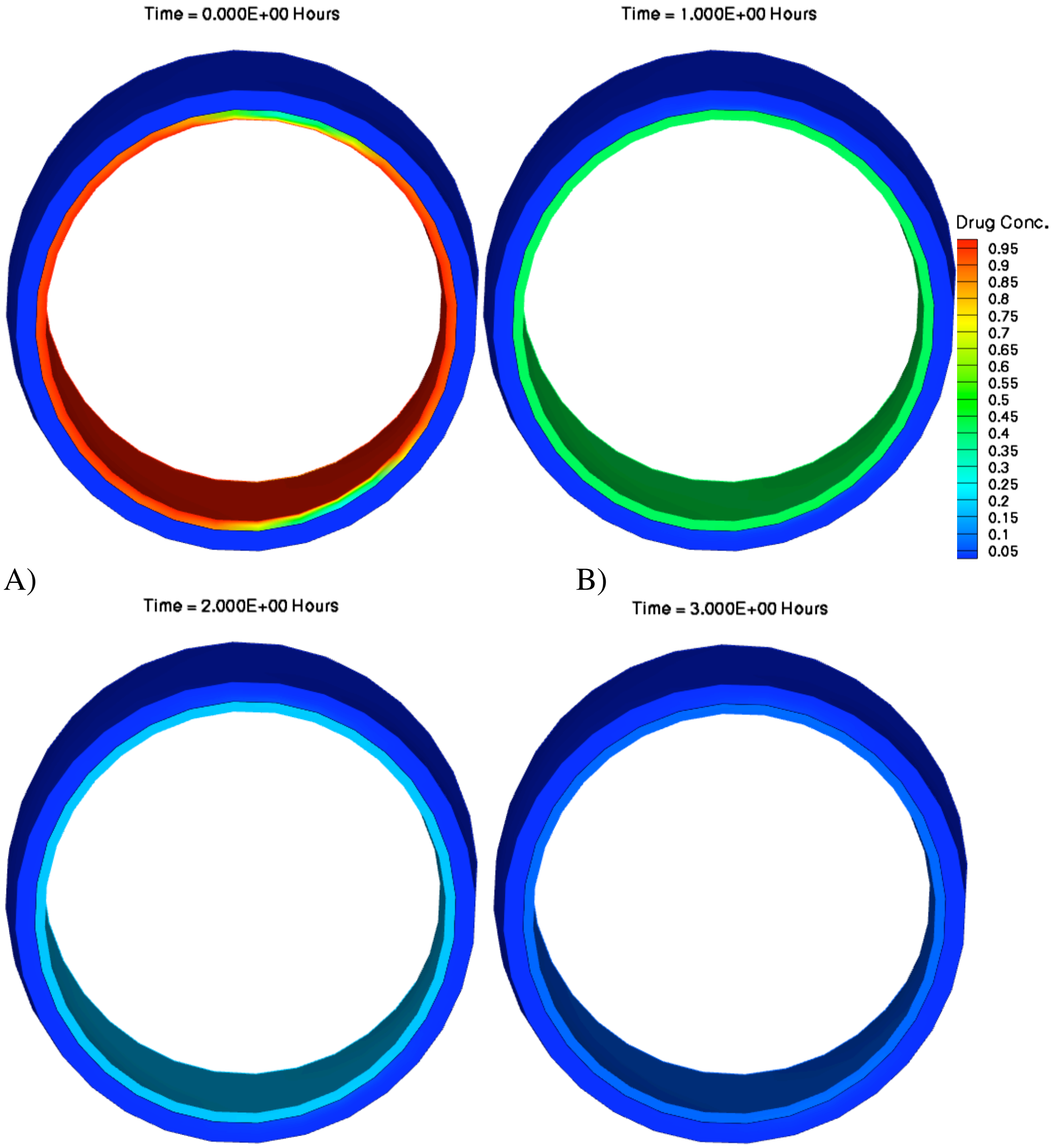

A) B) C) D)

Figure 6.20: Drug distribution in terms of concentration (normalized) at slice 3 of the patient-specific coronary artery wall segment under diseased condition at times A) t = 2 mins, B) t = 1 hr C) t = 2 hrs, D) t = 3 hrs. After 3 hrs only a trace amount of drug can be observed until the artery wall is completely depleted.

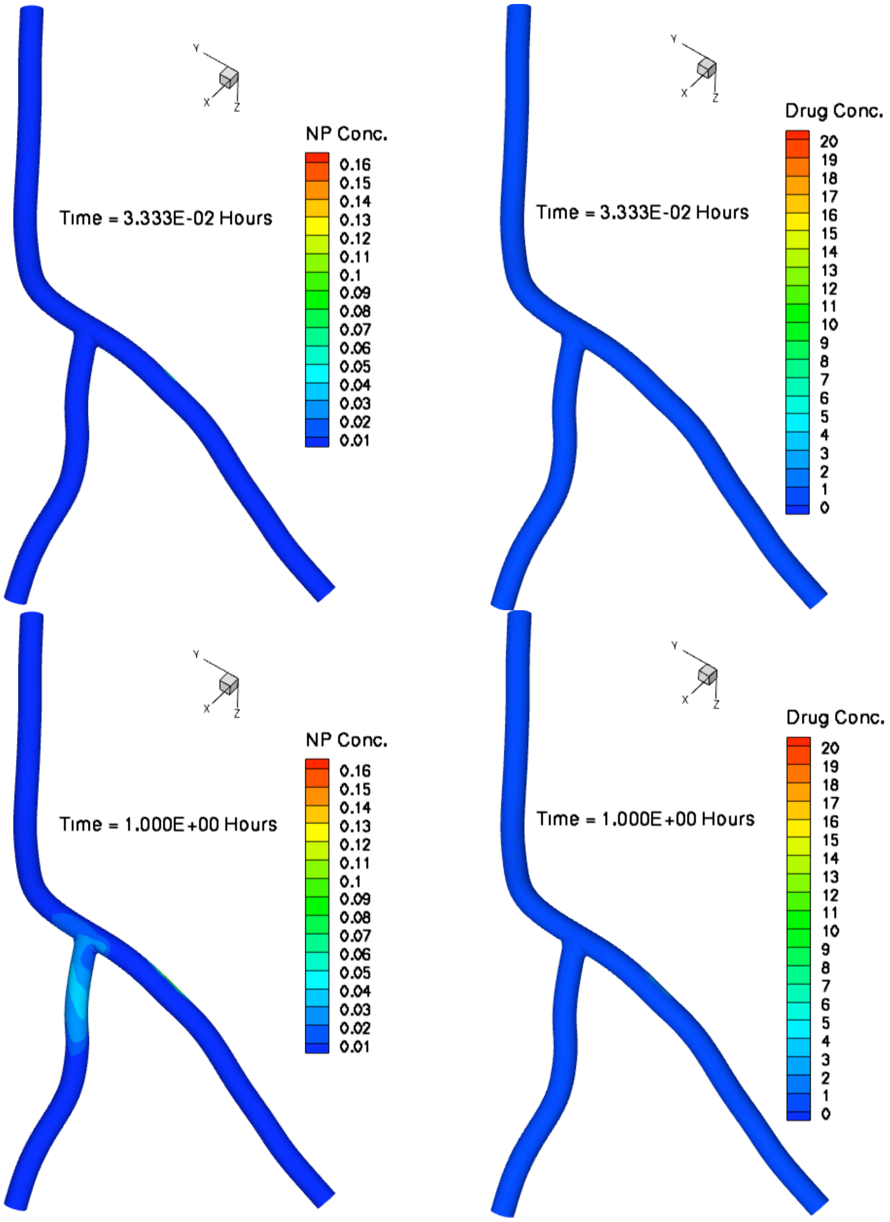

Figure 6.21a: Nanoparticle (left) and Drug (right) distribution in terms of concentration (normalized) at 1/3 depth from the lumen side of the patient-specific coronary artery wall segment under diseased condition at times $t = 2$ mins (top) and $t = 1$ hr (bottom).

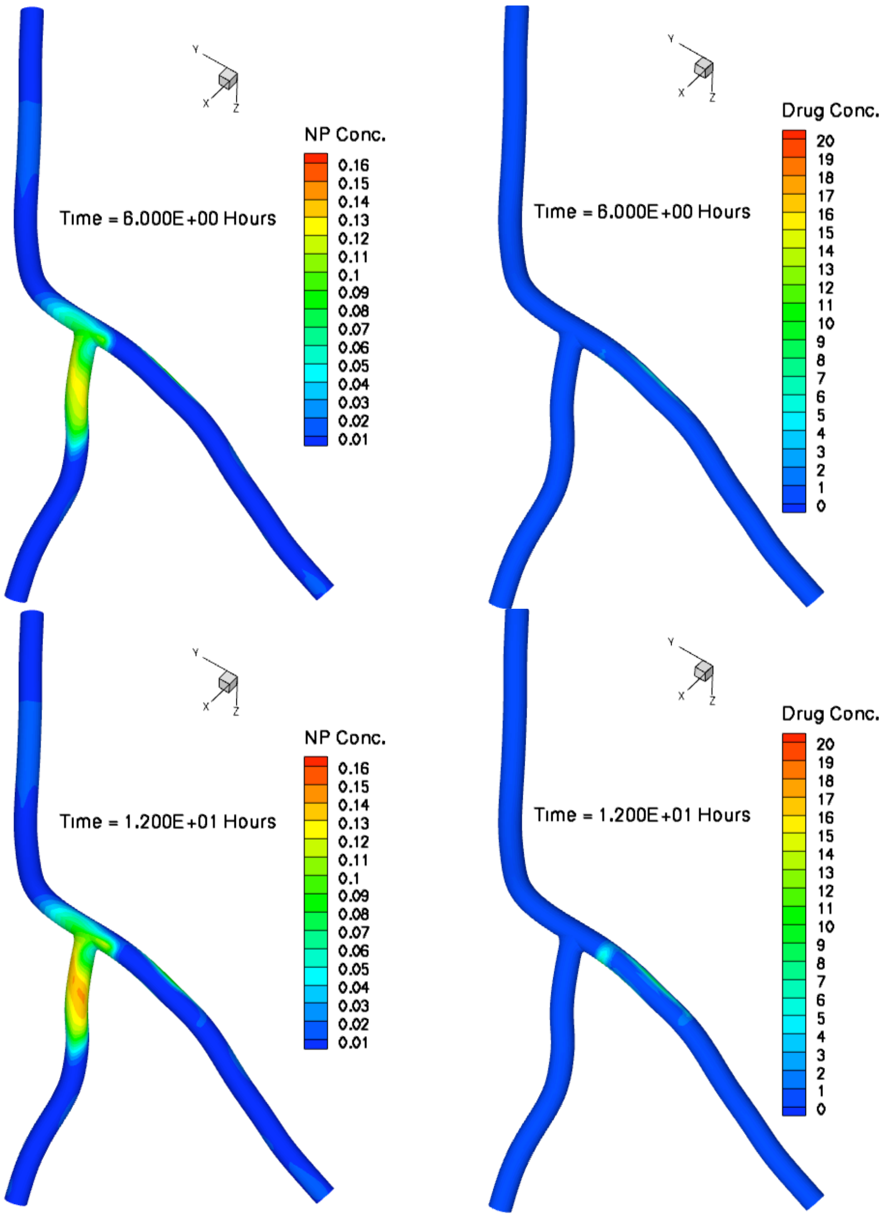

Figure 6.21b: Nanoparticle (left) and Drug (right) distribution in terms of concentration (normalized) at 1/3 depth from the lumen side of the patient-specific coronary artery wall segment under diseased condition at times t = 6 hrs (top) and t = 12 hrs (bottom).

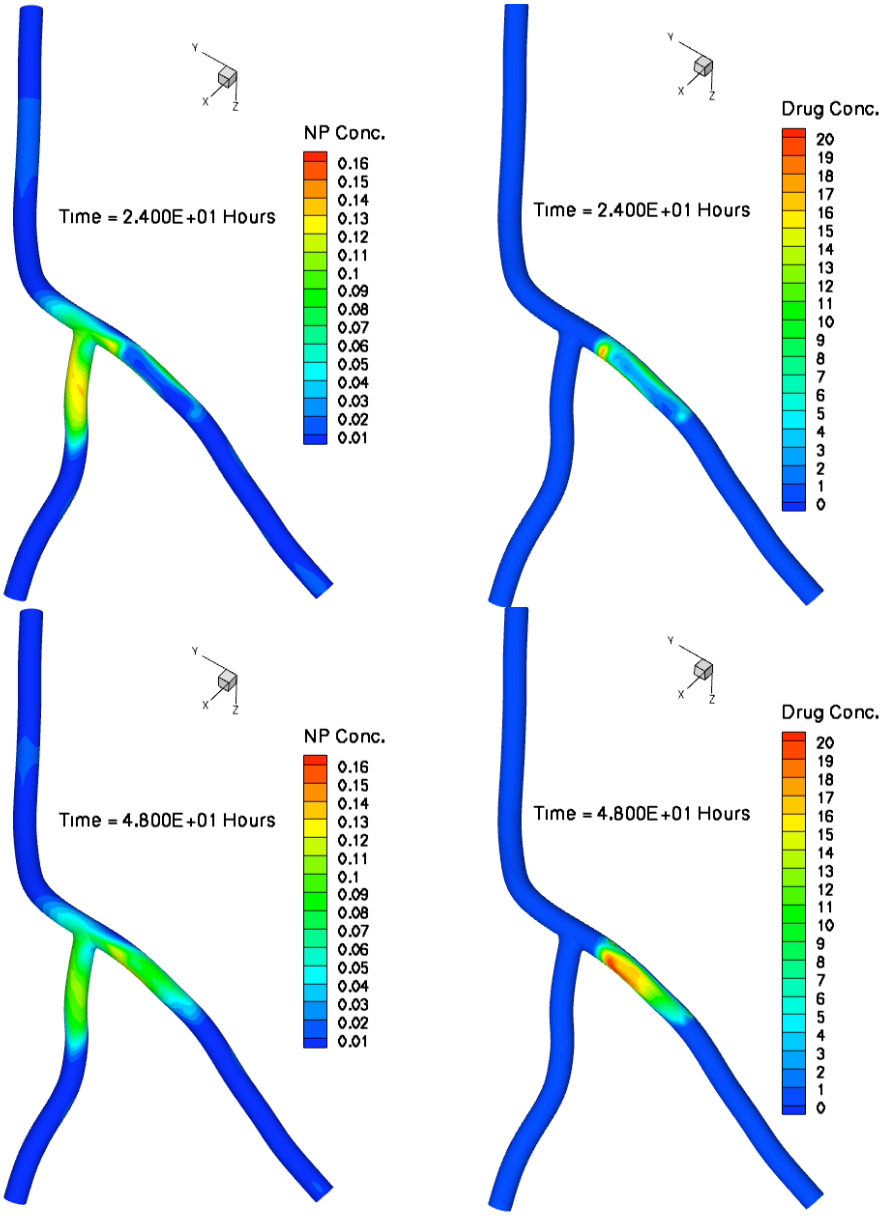

Figure 6.21c: Nanoparticle (left) and Drug (right) distribution in terms of concentration (normalized) at 1/3 depth from the lumen side of the patient-specific coronary artery wall segment under diseased condition at times $t = 24$ hrs (top) and $t = 48$ hrs (bottom).

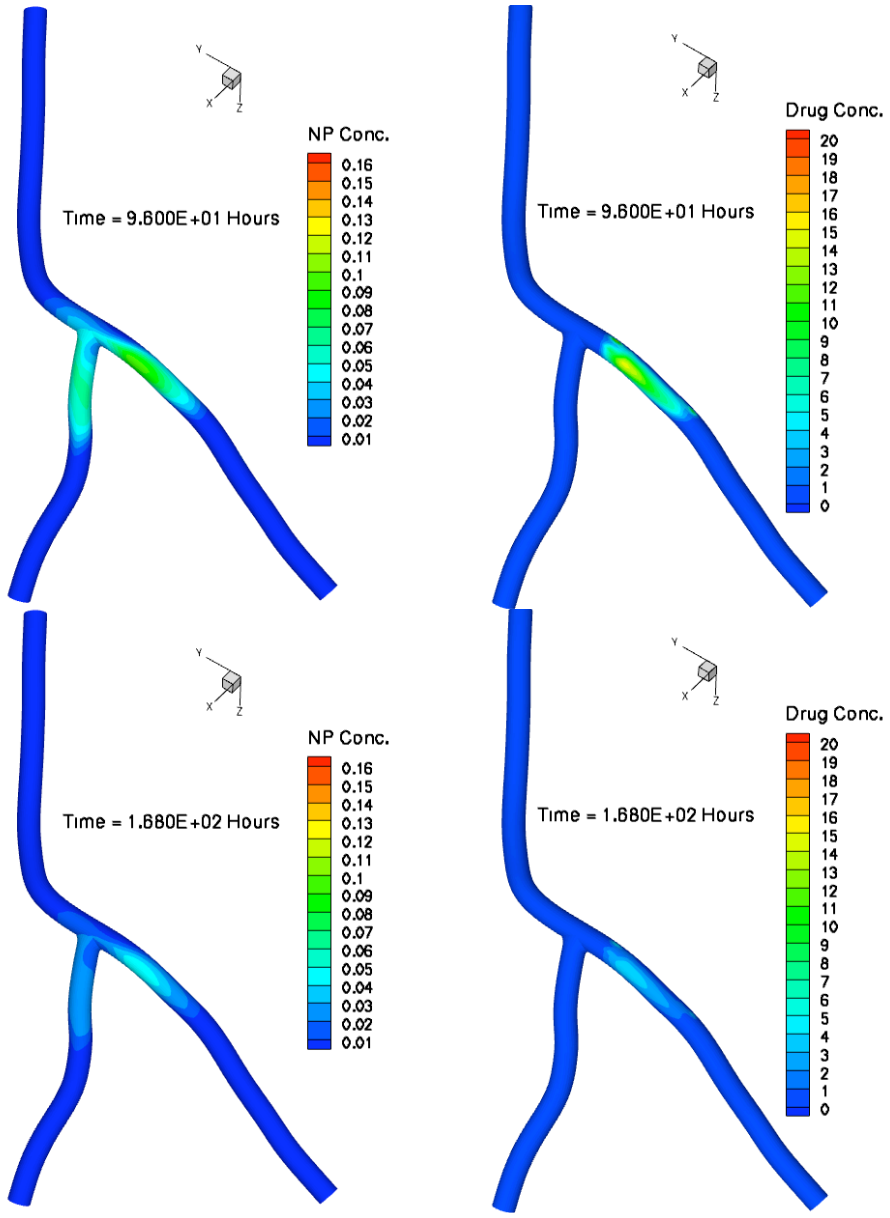

Figure 6.21d: Nanoparticle (left) and Drug (right) distribution in terms of concentration (normalized) at 1/3 depth from the lumen side of the patient-specific coronary artery wall segment under diseased condition at times t = 4 days (top) and t = 7 days (bottom).

CHAPTER 7

Conclusions and Future Work

Design and evaluation of local drug delivery systems involve understanding the complex interplay between a series of physiological processes, along with the physiochemical properties of the compounds delivered and their interactions. Concepts and technologies applicable to these configurations have been investigated herein in order to realistically simulate physiological phenomena and transport forces necessary for device design optimization that is otherwise difficult to achieve in an experimental setting.

In developing such a tool, the biggest challenge lies in the selection of parameters that are able to mimic the physiological forces reliably. A number of assumptions have been made which are deemed reasonable, however, they should be further investigated. The goal was to establish that the computational tool developed shows the right trends even though all the parameters may not be measurable in a precise way, and therefore is suitable for use in the drug delivery business to help optimize drug design parameters. A study of the parametric sensitivity of drug transport revealed that both the Peclet number and Damkohler number are dominant in the transport process, though it is more sensitive to variation in the latter case. The effect of free drug that may be present in the formulation in addition to the drug-encapsulated nanoparticles was also explored. Although free drug may provide an initial boost to the drug tissue uptake, its influence is negligible and limited in scope because free drug penetration is minimal and largely confined to a small area within the intima when the target area is usually the media or the plaque (depending on application). Additionally, free drug penetration lasts for a few hours at most until it is depleted completely through the lumen side boundary. Therefore its residence time may not be sufficiently long for it to act as a viable drug source to produce therapeutic effect to the surrounding area. Thus inclusion of free drug in the design may not augment drug transport effectively. This is an example of how this tool can address important design questions.

The methodology developed was applied to a few cases of physical interest in order to demonstrate its capabilities. A few trends were observed that make sense intuitively. In the healthy artery case, the nanoparticles have a largely uniform distribution within the intima, while there is an appreciable concentration gradient within the media during the first 48 hours after their administration. This observation agrees well with [39]. The IEL acts as a significant transport barrier to both species, though the resistance appears to be more pronounced for the drug, as drug transport in the intima is essentially diffusive in nature. This is consistent with the findings in [66]. Also, the diseased artery provides more resistance to drug transport, as reported in [64]. A comparison of the idealized case with the patient-specific one established that due to the highly coupled nature of transport between the two species, the nanoparticle wall deposition pattern and its intensity have a significant bearing on the overall drug distribution. Another important observation is that both arterial inhomogeneity and plaque heterogeneity modulate drug transport as expected from [64]. Additionally, drug transport is influenced by drug avidity. A direct consequence is lipid core recruits the hydrophobic drug and retains it such that there is a high local drug concentration within this target region for a reasonably long period of time. This is encouraging from a therapeutic point of view. Furthermore, the time evolution of this local drug distribution within the target region is very closely related to the drug release rate profile. Therefore, optimal therapeutic effect may be largely dependent on how well the release rate profile can be tuned to achieve peak concentration in synchronization with the time course of desired biological responses.

A comparison of the normal versus diseased patient-specific artery wall distribution demonstrates that the existence of vulnerable plaque reduces drug concentration level in the neighboring healthy branches. This indicates that the nanoparticles that are away from the target region may actually contribute to the overall therapeutic effect facilitated by the highly anisotropic nature of drug diffusion. Observations such as this make patient-specific geometry an essential ingredient in simulating realistic transport forces and flow features that are crucial for such modeling endeavors.

The findings of this dissertation provide a research framework for future work. An area to be addressed is an extension to non-rigid deformable artery wall models by developing a large deformation theory of flow in porous media. Incorporation of a bound drug model that will account for the specific and non-specific interactions of drug with binding sites within the arterial tissue is also planned. Furthermore, the modular aspect of this computational tool allows incorporation of functionalities fairly easily that can greatly facilitate design and optimization procedures. For example, one can tailor the existing model to introduce particle shape factor as a parameter in the coupled mass-transport equations. The effects of particle size and shape can be analyzed and validated against existing experimental work [80]. Future efforts will also include defining metrics (for example, dose homogeneity index, remaining mass percentage, and so on) to measure drug delivery efficiency, and thus effectiveness of various catheter systems.

Appendix A: Verification of numerical methods

Since transport of drug in the arterial wall is a highly diffusion dominant phenomenon, it makes pure diffusion a natural candidate for a model test problem to evaluate the performance of the numerical methods. The numerical code was therefore verified against a simple 1D pure diffusion problem

$$\begin{aligned} &\frac{\partial C}{\partial t} = D\frac{\partial^2 C}{\partial x^2} \qquad \text{in } \ 0 < x < 1, \\ &C(0,t) = 1, \\ &C(1,t) = 0, \\ &C(x,0) = 0 \qquad \text{on } \ 0 < x < 1 \text{ at } t = 0, \end{aligned} \tag{92}$$

with known analytical solution

$$C(x,t) = (1-x) - \frac{2}{\pi}\sum_{n=1}^{\infty}\frac{\sin n\pi x}{n}e^{-n^2\pi^2 Dt}. \tag{93}$$

Eq. (92) was solved for both the nanoparticles and pure drug with a coefficient of diffusion of D_I = 1e-12 cm^2/s and D_{II} = 1e-9 cm^2/s, respectively. The simulations were run for a period of 7 days using a time step of 2 minutes. A comparison of the numerical results with the analytical solutions in Eq. (93) show that the numerical approximations were fairly accurate for the mesh and time step chosen. This provided confidence in the accuracy and reliability of the numerical methods employed (see Figure A.1).

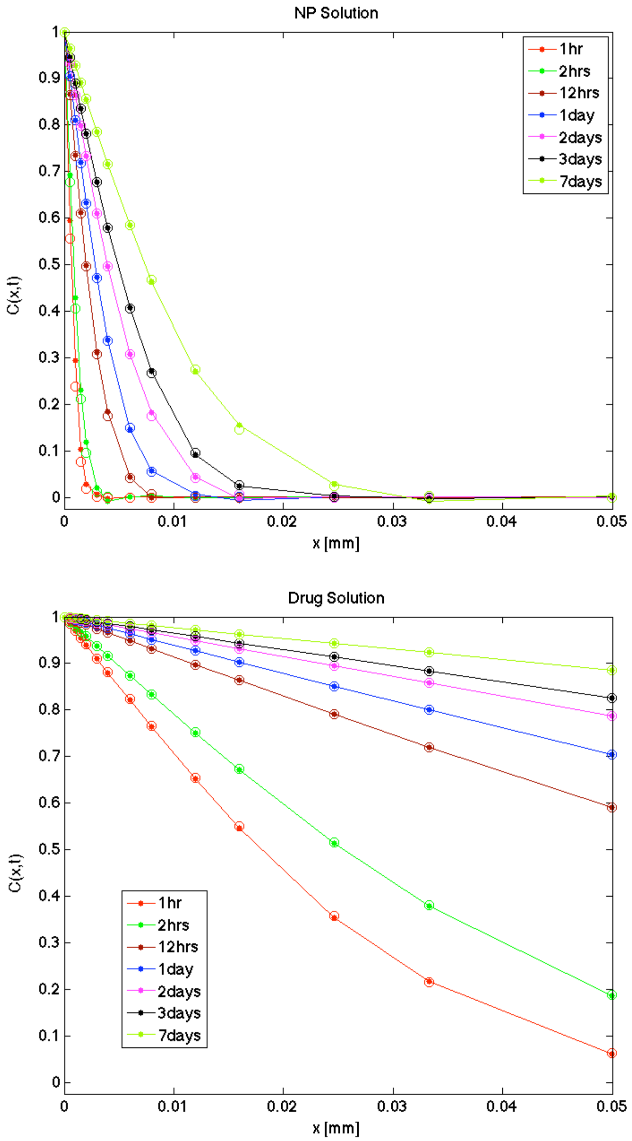

Figure A.1: A comparison of the numerical solution (dot) with the known analytical solution (circle) for the nanoparticles (top) and the drug (bottom) in 1D under purely diffusive transport as described in Eq. (92). Only the interesting part (1/20 of the thickness) of the artery wall has been shown here.

Glossary

MI = Myocardial Infarction
LDL = Low Density Lipoprotein
CRP = C-Reactive Protein
IVUS = Intravascular Ultrasound
SCD = Sudden Cardiac Death
NP = Nanoparticle
MRT = Mean Residence Time
3D = Three dimensional
1D = One dimensional
IEL = Internal Elastic Lamina
EEL = External Elastic Lamina
NURBS = Non-Uniform Rational B-Splines
GMRES = Generalized Minimal Residual Method
PDE = Partial Differential Equation
RR = Release Rate
LCA = Left Coronary Artery
LAD = Left Anterior Descending
MW = Molecular Weight
kDa = Kilo Daltons

HRP = Horseradish Peroxide

Cp = Centipoise

ATP = Adenosine Tri-Phosphate

D_{intima} = Diffusivity in the intima

D_{media} = Diffusivity in the media

D_{lipid} Diffusivity in the lipid core

D_{fc} Diffusivity in the fibrous cap

Da = Damkohler Number

Pe = Peclet Number

μm = micrometer

mm = millimeter

nm = nanometer

mins = minutes

hrs = hours

References

[1] J. Lau, D. Kent, A. Tatsioni, Y. Sun, C. Wang, P. Chew, B. Kupelnick, and H. Jordan, "Vulnerable Plaques: A Brief Review of the Concept and Proposed Approaches to Diagnosis and Treatment," U.S. Department of Health and Human Services, Rockville, MD 2004.

[2] J. C. Spratt and E. Camenzind, "Plaque stabilisation by systemic and local drug administration," *Heart,* vol. 90, pp. 1392-1394, 2004.

[3] P. K. Shah, "Mechanisms of plaque vulnerability and rupture," *Journal of the American College of Cardiology,* vol. 41, pp. S15-S22, 2003.

[4] M. Naghavi, P. Libby, E. Falk, S. W. Casscells, S. Litovsky, J. Rumberger, J. J. Badimon, C. Stefanadis, P. Moreno, G. Pasterkamp, Z. Fayad, P. H. Stone, S. Waxman, P. Raggi, M. Madjid, A. Zarrabi, A. Burke, C. Yuan, P. J. Fitzgerald, D. S. Siscovick, C. L. de Korte, M. Aikawa, K. E. J. Airaksinen, G. Assmann, C. R. Becker, J. H. Chesebro, A. Farb, Z. S. Galis, C. Jackson, I.-K. Jang, W. Koenig, R. A. Lodder, K. March, J. Demirovic, M. Navab, S. G. Priori, M. D. Rekhter, R. Bahr, S. M. Grundy, R. Mehran, A. Colombo, E. Boerwinkle, C. Ballantyne, W. Insull, Jr, R. S. Schwartz, R. Vogel, P. W. Serruys, G. K. Hansson, D. P. Faxon, S. Kaul, H. Drexler, P. Greenland, J. E. Muller, R. Virmani, P. M. Ridker, D. P. Zipes, P. K. Shah, and J. T. Willerson, "From vulnerable plaque to vulnerable patient: a call for new definitions and risk assessment strategies: Part II," *Circulation,* vol. 108, pp. 1772-1778, 2003.

[5] M. Naghavi, P. Libby, E. Falk, S. W. Casscells, S. Litovsky, J. Rumberger, J. J. Badimon, C. Stefanadis, P. Moreno, G. Pasterkamp, Z. Fayad, P. H. Stone, S. Waxman, P. Raggi, M. Madjid, A. Zarrabi, A. Burke, C. Yuan, P. J. Fitzgerald, D. S. Siscovick, C. L. de Korte, M. Aikawa, K. E. J. Airaksinen, G. Assmann, C. R. Becker, J. H. Chesebro, A. Farb, Z. S. Galis, C. Jackson, I.-K. Jang, W. Koenig, R. A. Lodder, K. March, J. Demirovic, M. Navab, S. G. Priori, M. D. Rekhter, R. Bahr, S. M. Grundy, R. Mehran, A. Colombo, E. Boerwinkle, C. Ballantyne, W. Insull, Jr, R. S. Schwartz, R. Vogel, P. W. Serruys, G. K. Hansson, D. P. Faxon, S. Kaul, H. Drexler, P. Greenland, J. E. Muller, R. Virmani, P. M. Ridker, D. P. Zipes, P. K. Shah, and J. T. Willerson, "From vulnerable

plaque to vulnerable patient: a call for new definitions and risk assessment strategies: Part I," *Circulation,* vol. 108, pp. 1664-1672, 2003.

[6] "Heart Disease and Stroke Statistics - 2006 Update," American Heart Association, Dallas, TX 2006.

[7] "Heart Disease and Stroke Statistics-2005 Update," American Heart Association, Dallas, TX 2005.

[8] "Heart Disease and Stroke Statistics-2008 Update," American Heart Association, Dallas, TX 2008.

[9] "Heart attack and acute coronary syndrome," in *In-Depth Reports*. vol. 2007, M. D. Harvey Simon, Ed.: A.D.A.M. Inc.

[10] E. Falk, P. K. Shah, and V. Fuster, "Coronary Plaque Disruption," *Circulation,* vol. 92, pp. 657-671, 1995.

[11] P. M. Ridker, C. P. Cannon, D. Morrow, N. Rifai, L. M. Rose, C. H. McCabe, M. A. Pfeffer, E. Braunwald, E. the Pravastatin or Atorvastatin, and I. Infection Therapy-Thrombolysis in Myocardial Infarction, "C-Reactive Protein Levels and Outcomes after Statin Therapy," *The New England Journal of Medicine,* vol. 352, pp. 20-28, 2005.

[12] M. Aikawa, E. Rabkin, S. Sugiyama, S. J. Voglic, Y. Fukumoto, Y. Furukawa, M. Shiomi, F. J. Schoen, and P. Libby, "An HMG-CoA reductase inhibitor, cerivastatin, suppresses growth of macrophages expressing matrix metalloproteinases and tissue factor in vivo and in vitro," *Circulation,* vol. 103, pp. 276-283, 2001.

[13] M. Aikawa and P. Libby, "Lipid lowering reduces proteolytic and prothrombotic potential in rabbit atheroma," *Annals Of The New York Academy Of Sciences,* vol. 902, pp. 140-152, 2000.

[14] M. Aikawa, E. Rabkin, Y. Okada, S. J. Voglic, S. K. Clinton, C. E. Brinckerhoff, G. K. Sukhova, and P. Libby, "Lipid lowering by diet reduces matrix metalloproteinase activity and increases collagen content of rabbit atheroma: a potential mechanism of lesion stabilization," *Circulation,* vol. 97, pp. 2433-2444, 1998.

[15] A. Tonkin, P. Aylward, D. Colquhoun, P. Glasziou, P. Harris, D. Hunt, A. Keech, S. MacMahon, P. Magnus, D. Newel, P. Nestel, N. Sharpe, J.

Shaw, R.J. Simes, P. Thompson, and A. Thomson, "Prevention of Cardiovascular Events and Death with Pravastatin in Patients with Coronary Heart Disease and a Broad Range of Initial Cholesterol Levels," *The New England Journal of Medicine,* vol. 339, pp. 1349-1357, 1998.

[16] F. M. Sacks, M. A. Pfeffer, L. A. Moye, J. L. Rouleau, J. D. Rutherford, T. G. Cole, L. Brown, J. W. Warnica, J. M. O. Arnold, C.-C. Wun, B. R. Davis, E. Braunwald, a. The Cholesterol, and I. Recurrent Events Trial, "The Effect of Pravastatin on Coronary Events after Myocardial Infarction in Patients with Average Cholesterol Levels," *The New England Journal of Medicine,* vol. 335, pp. 1001-1009, 1996.

[17] J. Shepherd, S. M. Cobbe, I. Ford, C. G. Isles, A. R. Lorimer, P. W. Macfarlane, J. H. McKillop, C. J. Packard, and G. The West of Scotland Coronary Prevention Study, "Prevention of Coronary Heart Disease with Pravastatin in Men with Hypercholesterolemia," *The New England Journal of Medicine,* vol. 333, pp. 1301-1308, 1995.

[18] T. R. Pedersen, J. Kjekshus, K. Berg, T. Haghfelt, O. Faergeman, G. Faergeman, K. Pyörälä, T. Miettinen, L. Wilhelmsen, A. G. Olsson , and H. Wedel, "Randomised trial of cholesterol lowering in 4444 patients with coronary heart disease: the Scandinavian Simvastatin Survival Study (4S)," *The Lancet,* vol. 344, pp. 1383–1389, 1994.

[19] D. Davalian, "Luminal Drug Delivery Product Concept," Santa Clara, CA: Abbott Vascular, Inc., 2007.

[20] J. Kreuter, "Nanoparticles," in *Colloidal Drug Delivery Systems* J. Kreuter, Ed. New York: Marcel Dekker, 1994.

[21] D. Davalian, J. Wan, and K. Klein, "ApoA1 Formulation," Santa Clara, CA: Abbott Vascular, Inc., 2008.

[22] G. Meyer, R. Merval, and A. Tedgui, "Effects of Pressure-Induced Stretch and Convection on Low-Density Lipoprotein and Albumin Uptake in the Rabbit Aortic Wall," *Circulation Research,* vol. 79, pp. 532-540, 1996.

[23] C.-W. Hwang, D. Wu, and E. R. Edelman, "Physiological Transport Forces Govern Drug Distribution for Stent-Based Delivery," *Circulation,* vol. 104, pp. 600-605, 2001.

[24] G. Karner, K. Perktold, and H. P. Zehentner, "Computational Modeling of Macromolecule Transport in the Arterial Wall," *Computer Methods in Biomechanics and Biomedical Engineering,* vol. 4, pp. 491 - 504, 2001.

[25] L. Ai and K. Vafai, "A coupling model for macromolecule transport in a stenosed arterial wall," *International Journal of Heat and Mass Transfer,* vol. 49, pp. 1568-1591, 2006.

[26] Z. J. Huang and J. M. Tarbell, "Numerical simulation of mass transfer in porous media of blood vessel walls," *The American Journal of Physiology - Heart and Circulatory Physiology,* vol. 273, pp. H464-477, 1997.

[27] M. Prosi, P. Zunino, K. Perktold, and A. Quarteroni, "Mathematical and numerical models for transfer of low-density lipoproteins through the arterial walls: a new methodology for the model set up with applications to the study of disturbed lumenal flow," *Journal of Biomechanics,* vol. 38, pp. 903-917, 2005.

[28] N. Sun, N. Wood, A. Hughes, S. Thom, and X. Xu, "Fluid-Wall Modelling of Mass Transfer in an Axisymmetric Stenosis: Effects of Shear-Dependent Transport Properties," *Annals of Biomedical Engineering,* vol. 34, pp. 1119-1128, 2006.

[29] S. Hossain, Y. Bazilevs, N. Brasher, V. M. Calo, and T. J. R. Hughes, "Numerical Investigation of Blood Flow and Drug Transport in Patient - Specific Coronary Arteries," in *9th US National Congress on Computational Mechanics*, San Francisco, CA, 2007.

[30] D. K. Stangeby and C. R. Ethier, "Computational Analysis of Coupled Blood-Wall Arterial LDL Transport," *Journal of Biomechanical Engineering,* vol. 124, pp. 1-8, 2002.

[31] D. K. Stangeby and C. R. Ethier, "Coupled Computational Analysis of Arterial LDL Transport -- Effects of Hypertension," *Computer Methods in Biomechanics and Biomedical Engineering,* vol. 5, pp. 233 - 241, 2002.

[32] N. Sun, N. B. Wood, A. D. Hughes, S. A. M. Thom, and X. Yun Xu, "Effects of transmural pressure and wall shear stress on LDL accumulation in the arterial wall: a numerical study using a multilayered model," *The American Journal of Physiology - Heart and Circulatory Physiology,* vol. 292, pp. H3148-3157, 2007.

[33] C. P. Markou, E. M. Lutostansky, D. N. Ku, and S. R. Hanson, "A Novel Method for Efficient Drug Delivery," *Annals of Biomedical Engineering,* vol. 26, pp. 502-511, 1998.

[34] P. Zunino, "Multidimensional Pharmacokinetic Models Applied to the Design of Drug-Eluting Stents," *Cardiovascular Engineering,* vol. 4, pp. 181-191, 2004.

[35] G. Pontrelli and F. d. Monte, "Modelling of mass convection-diffusion in stent-based drug delivery," in *XXV Congresso Nazionale UIT sulla Trasmissione del Calore* Trieste, Giugno 2007, pp. 18-20

[36] V. M. Calo, N. Brasher, Y. Bazilevs, and T. J. R. Hughes, "Multiphysics model for blood flow and drug transport with application to patient-specific coronary artery flow," *Computational Mechanics,* vol. 43, pp. 161-177, 2008.

[37] J. A. Moore and C. R. Ethier, "Oxygen Mass Transfer Calculations in Large Arteries," *Journal of Biomechanical Engineering,* vol. 119, pp. 469-475, 1997.

[38] S. Tada and J. M. Tarbell, "Internal elastic lamina affects the distribution of macromolecules in the arterial wall: a computational study," *The American Journal of Physiology - Heart and Circulatory Physiology,* vol. 287, pp. H905-913, 2004.

[39] N. Yang and K. Vafai, "Modeling of low-density lipoprotein (LDL) transport in the artery--effects of hypertension," *International Journal of Heat and Mass Transfer,* vol. 49, pp. 850-867, 2006.

[40] P. Feenstra and C. Taylor, "Drug transport in artery walls: A sequential porohyperelastic-transport approach," *Computer Methods in Biomechanics and Biomedical Engineering,* vol. 12, pp. 263-76, 2009.

[41] G. Pontrelli and F. de Monte, "Mass diffusion through two-layer porous media: an application to the drug-eluting stent," *International Journal of Heat and Mass Transfer,* vol. 50, pp. 3658-3669, 2007.

[42] N. Koshiba, J. Ando, X. Chen, and T. Hisada, "Multiphysics Simulation of Blood Flow and LDL Transport in a Porohyperelastic Arterial Wall

Model," *Journal of Biomechanical Engineering,* vol. 129, pp. 374-385, 2007.

[43] J. Crank, *The Mathematics of Diffusion*, Second ed. Oxford: Oxford University Press, 1975.

[44] S. Hossainy, S. Prabhu, S. Hossain, D. Davalian, and J. Wan, "Mathematical Modeling of Bi-phasic Mixed Particle Drug Release from Nanoparticles," in *8th World Biomaterials Congress*, Amsterdam, 2008.

[45] S. Hossainy and S. Prabhu, "A mathematical model for predicting drug release from a biodurable drug-eluting stent coating," *Journal of Biomedical Materials Research Part A,* vol. 9999, p. NA, 2008.

[46] W. M. Saltzman, *Drug Delivery*. New York: Oxford, 2001.

[47] T. J. R. Hughes, J. A. Cottrell, and Y. Bazilevs, "Isogeometric analysis: CAD, finite elements, NURBS, exact geometry and mesh refinement," *Computer Methods in Applied Mechanics and Engineering,* vol. 194, pp. 4135-4195, 2005.

[48] Y. Bazilevs, L. B. da Veiga, J. A. Cottrell, T. J. R. Hughes, and G. Sangalli, "Isogeometric analysis: Approximation, stability and error estimates for h-refined meshes," *Mathematical Models & Methods in Applied Sciences,* vol. 16, pp. 1031-1090, 2006.

[49] J. Chung and G. M. Hulbert, "A time integration algorithm for structural dynamics with improved numerical dissipation: The generalized-method," *Journal of Applied Mechanics,* vol. 60, pp. 371–75, 1993.

[50] K. E. Jansen, C. H. Whiting, and G. M. Hulbert, "A generalized-[alpha] method for integrating the filtered Navier-Stokes equations with a stabilized finite element method," *Computer Methods in Applied Mechanics and Engineering,* vol. 190, pp. 305-319, 2000.

[51] Y. Saad and M. Schultz, "GMRES: A Generalized Minimal Residual Algorithm for Solving Nonsymmetric Linear Systems," *SIAM Journal on Scientific and Statistical Computing,* vol. 7, pp. 856-869, 1986.

[52] C. Caro, "Steady transport of material in the artery wall," in *Advances in Fluid Mechanics*, 1981, pp. 314-329.

[53] I. Gradus-Pizlo, B. Bigelow, Y. Mahomed, S. G. Sawada, K. Rieger, and H. Feigenbaum, "Left anterior descending coronary artery wall thickness measured by high-frequency transthoracic and epicardial echocardiography includes adventitia," *The American Journal of Cardiology,* vol. 91, pp. 27-32, 2003.

[54] D. Velican and C. Velican, "Comparative study on age related changes and atherosclerosis involvement of the coronary arteries of male and female subjects up to 40 years of age," *Atherosclerosis,* vol. 316 pp. 39–50, 1981.

[55] F. Migliavacca, F. Gervaso, M. Prosi, P. Zunino, S. Minisini, L. Formaggia, and G. Dubini, "Expansion and drug elution model of a coronary stent," *Computer Methods in Biomechanics and Biomedical Engineering,* vol. 10, pp. 63 - 73, 2007.

[56] S. Hossainy, Personal Communication ed Santa Clara: Abbott Vascular Inc., 2007.

[57] J. M. Tarbell, M. J. Lever, and C. G. Caro, "The effect of varying albumin concentration of the hydraulic conductivity of the rabbit common carotid artery," *Microvascular Research,* vol. 35, pp. 204-220, 1988.

[58] Y. Huang, D. Rumschitzki, S. Chien, and S. Weinbaum, "A Fiber Matrix Model for the Growth of Macromolecular Leakage Spots in the Arterial Intima," *Journal of Biomechanical Engineering,* vol. 116, pp. 430-445, 1994.

[59] L. Hagar, "Diffusion of drug delivery vehicles (DDVs) through the arterial wall " Santa Clara, CA: Abbott Vascular Inc., 2007.

[60] C. J. Creel, M. A. Lovich, and E. R. Edelman, "Arterial Paclitaxel Distribution and Deposition," *Circulation Research,* vol. 86, pp. 879-884, 2000.

[61] C.-W. Hwang, A. D. Levin, M. Jonas, P. H. Li, and E. R. Edelman, "Thrombosis Modulates Arterial Drug Distribution for Drug-Eluting Stents," *Circulation,* vol. 111, pp. 1619-1626, 2005.

[62] F. Yuan, S. Chien, and S. Weinbaum, "A New View of Convective-Diffusive Transport Processes in the Arterial Intima," *Journal of Biomechanical Engineering,* vol. 113, pp. 314-329, 1991.

[63] M. L. Reed and W. K. Lye, "Microsystems for drug and gene delivery," *Proceedings of the IEEE,* vol. 92, pp. 56-75, 2004.

[64] C.-W. Hwang and E. R. Edelman, "Arterial Ultrastructure Influences Transport of Locally Delivered Drugs," *Circulation Research,* vol. 90, pp. 826-832, 2002.

[65] A. D. Levin, N. Vukmirovic, C.-W. Hwang, and E. R. Edelman, "Specific binding to intracellular proteins determines arterial transport properties for rapamycin and paclitaxel," *Proceedings of the National Academy of Sciences of the United States of America,* vol. 101, pp. 9463-9467, 2004.

[66] M. S. Penn, G. M. Saidel, and G. M. Chisolm, "Relative significance of endothelium and internal elastic lamina in regulating the entry of macromolecules into arteries in vivo," *Circulation Research,* vol. 74, pp. 74-82, 1994.

[67] D. L. Fry, "Mass transport, atherogenesis, and risk," *Arteriosclerosis, Thrombosis, and Vascular Biology,* vol. 7, pp. 88-100, 1987.

[68] D. L. Fry, "Mathematical models of arterial transmural transport," *The American Journal of Physiology - Heart and Circulatory Physiology,* vol. 248, pp. H240-263, 1985.

[69] K. Lee, G. M. Saidel, and M. S. Penn, "Permeability change of arterial endothelium is an age-dependent function of lesion size in apolipoprotein E-null mice," *The American Journal of Physiology - Heart and Circulatory Physiology,* vol. 295, pp. H2273-2279, 2008.

[70] E. Arne, A. Hilde Nortvedt, N. Stine Nalum, S. Pawel, and D. Catharina de Lange, "Physical and chemical modifications of collagen gels: Impact on diffusion," *Biopolymers,* vol. 89, pp. 135-143, 2008.

[71] V. Shenoy and J. Rosenblatt, "Diffusion of Macromolecules in Collagen and Hyaluronic Acid, Rigid-Rod-Flexible Polymer, Composite Matrixes," *Macromolecules,* vol. 28, pp. 8751-8758, 2002.

[72] D. Levitt, "Heterogeneity of human adipose blood flow " *BMC Clinical Pharmacology,* vol. 7, p. 1, 2007.

[73] A. L. Mark, C. Chris, H. Kristy, H. Chao-Wei, and R. E. Elazer, "Carrier proteins determine local pharmacokinetics and arterial distribution of paclitaxel," *Journal of Pharmaceutical Sciences,* vol. 90, pp. 1324-1335, 2001.

[74] Y. Bazilevs, V. M. Calo, T. E. Tezduyar, and T. J. R. Hughes, "YZbeta discontinuity capturing for advection-dominated processes with application to arterial drug delivery," *International Journal for Numerical Methods in Fluids,* vol. 54, pp. 593-608, 2007.

[75] J. Ohayon, G. Finet, A. M. Gharib, D. A. Herzka, P. Tracqui, J. Heroux, G. Rioufol, M. S. Kotys, A. Elagha, and R. I. Pettigrew, "Necrotic core thickness and positive arterial remodeling index: emergent biomechanical factors for evaluating the risk of plaque rupture," *The American Journal of Physiology - Heart and Circulatory Physiology,* vol. 295, pp. H717-727, 2008.

[76] Y. Zhang, Y. Bazilevs, S. Goswami, C. L. Bajaj, and T. J. R. Hughes, "Patient-specific vascular NURBS modeling for isogeometric analysis of blood flow," *Computer Methods in Applied Mechanics and Engineering,* vol. 196, pp. 2943-2959, 2007.

[77] C. K. Zarins, D. P. Giddens, B. K. Bharadvaj, V. S. Sottiurai, R. F. Mabon, and S. Glagov, "Carotid bifurcation atherosclerosis. Quantitative correlation of plaque localization with flow velocity profiles and wall shear stress," *Circulation Research,* vol. 53, pp. 502-514, 1983.

[78] P. Jerzy, T. Pawel, S. M. Gary, K. Sang-Wook, W. Adam, S. Lowell, K. Mariusz, W. Ron, M. Akiko, and J. W. Neil, "Intravascular ultrasound assessment of the spatial distribution of ruptured coronary plaques in the left anterior descending coronary artery," *American Heart Journal,* vol. 151, pp. 898-901, 2006.

[79] A. Oshima, S. Takeshita, K. Kozuma, N. Yokoyama, K. Motoyoshi, S. Ishikawa, M. Honda, K. Oga, M. Ochiai, and T. Isshiki, "Intravascular Ultrasound Analysis of the Radial Artery for Coronary Artery Bypass Grafting," *The Annals of Thoracic Surgery,* vol. 79, pp. 99-103, 2005.

[80] S. E. A. Gratton, P. A. Ropp, P. D. Pohlhaus, J. C. Luft, V. J. Madden, M. E. Napier, and J. M. DeSimone, "The effect of particle design on cellular internalization pathways," *Proceedings of the National Academy of Sciences,* vol. 105, pp. 11613-11618, 2008.

Vita

Shaolie Samira Hossain was born and raised in Bangladesh. She received Bachelor of Science in Mechanical Engineering with Honors from Bangladesh University of Engineering and Technology in 2000. She was awarded Dr. V. G. Desa Gold Medal for graduating with the highest GPA in her class. After working for over a year as a lecturer at the same university, she went to Stanford University, Stanford, CA, on a four year ASCI scholarship to work under Dr. Norbert Peters in the area of Combustion Sciences. Toward the end of her masters program, while working on a project with Dr. Charles Taylor, she discovered a passion for Cardiovascular Biomechanics. After obtaining Master of Science degree in Mechanical Engineering from Stanford in 2003, she relocated to Austin, Texas to pursue a PhD degree under Dr. Thomas J. R. Hughes at The University of Texas at Austin. She worked as a research intern at Abbott Vascular, Santa Clara, CA, for 6 months in 2007.

Permanent address: 6704 Havenbrook Cove, Austin, TX 78759
This dissertation was typed by the author.